Dissertation
submitted to the
Combined Faculties of the Natural Sciences and Mathematics
of the Ruperto-Carola-University of Heidelberg, Germany
for the degree of
Doctor of Natural Sciences

Put forward by
M. Sc. Clemens Velte
born in: Münster

Oral examination: 30. October 2019

Measurement of a high energy resolution and high statistics ^{163}Ho electron capture spectrum for the ECHo experiment

Referees: JProf. Dr. Loredana Gastaldo
Prof. Dr. Hans-Christian Schulz-Coulon

The goal of the ECHo collaboration is to reach a sub-eV sensitivity on the effective electron neutrino mass by the analysis of the high energy resolution and high statistics ^{163}Ho electron capture spectrum measured with metallic magnetic micro calorimeters. Within this thesis several measurements have been performed for detector optimization and for a study of the spectral shape of the ^{163}Ho . In a first measurement the heat capacity of Ho-ions implanted in gold absorbers was measured. It was found that an implanted activity per pixel of $a = 10\,\mathrm{Bq}$ does not compromise in a noticeable way the performance of the detector at $T = 20\,\mathrm{mK}$. To test the performance of MMC detectors shielded by rock and to check this option of operation for future ECHo phases, an experiment was performed in an underground lab. This measurement allowed for the first time a detailed investigation of the ^{163}Ho spectral shape. Furthermore, was a first high statistic ^{163}Ho spectrum acquired. The analysis allows for a determination of the Q-value of the ^{163}Ho EC with $Q = 2.837 \pm 0.005^{stat} \pm 0.005^{syst}\,\mathrm{keV}$ and to perform a first analysis of the end point region of the spectrum to extract an effective electron neutrino mass.

Messung eines Hochstatistik ^{163}Ho -Elektroneneinfangspektrums mit hoher Energieauflösung für das ECHo Experiment

Ziel des ECHo-Projektes ist ein neues oberes Limit für die effektive Elektron-Neutrinomasse $m_\nu < 1\mathrm{eV}$ zu geben mittels der Analyse eines ^{163}Ho -Elektroneneinfangspektrums, welches mit metallischen magnetischen Kalorimetern (MMC) gemessen wird. In dieser Arbeit wurden mehrere Messungen für das ECHo Projekt durchgeführt. In der ersten Messung wurde die Wärmekapazität der in den Goldabsorber der MMCs implantierten Ho-Ionen gemessen. Es wurde gezeigt, dass die angestrebte Aktivität von 10 Bq pro MMC bei einer Temperatur von 20 mK die Detektorleistung nicht wahrnehmbar beeinflusst. Um die Notwendigkeit einer Abschirmung durch Gestein, auch für spätere Phasen von ECHo, zu testen wurde eine Messung des ^{163}Ho -Spektrums in einem Untergrundlabor durchgeführt. Dies erlaubte zum erstem Mal eine detaillierte Analyse der spektralen Form von ^{163}Ho . Zudem wurde ein erstes ^{163}Ho -Spektrum mit einer sehr hohen Statistik und einer guten Detektor-Energieauflösung gemessen. $Q = 2.837 \pm 0.005^{stat} \pm 0.005^{syst}\,\mathrm{keV}$ konnte durch eine Analyse der Messergebnisse bestimmt werden. Außerdem konnten durch die Analyse der Endpunktsregion erste Informationen über m_ν extrahiert werden.

Contents

1. Introduction

It was a long way from the first suggestion of the neutrino by W. Pauli in 1933, to the experimental evidence of neutrino oscillations in 1998 by the Super-Kamiokande experiment [Fuk98], with all their consequences. The difficulty from experimental side was and still is the fact that neutrinos only interact weakly. Parallel to the theoretical development of the description of neutrinos and the embedding in existing theories or even coming up with new theories taking account neutrinos, the experiments have developed a lot. The first experiments, which needed a third particle as decay partner to explain energy and momentum conservation in the decay of ^{214}Pb and ^{214}Bi have been done in a standard laboratory by J. Chadwick in 1914. Already the next experimental step in 1956 by Cowan [Cow56], which provided the first measurement of a neutrino, needed a big water tank in front of a nuclear reactor and more than 40 years. As the neutrino became more and more interesting new experiments developed, bigger and with better equipment then before, bringing the detectors underground and scaling up the detection medium a lot as done by the Homestake experiment in 1968 to measure the solar neutrino flux. Resulting in two even larger experiments SNO and Super-Kamiokande providing the evidence for neutrino oscillations, with the consequence of a finite neutrino mass. In our days even more experiment like the DUNE experiment [Gra17] or the follow up experiment of Super-Kamiokande HYPER-K [Abe18] with better detectors and a higher budget are performed to investigate the parameters of neutrino oscillations with a high precision. And although the used detectors were based on quite simple methods, which have not dramatically changed over the years, the implementation of these has developed a lot. Better energy resolutions, higher sensitivities and in general better performances have been established. This path of detector development and large effort for neutrinos is followed as well for the still unanswered question of the absolute scale of the neutrino masses.

To test a finite neutrino mass, or the fact that it has none, was already proposed quite early. One particular case in this field is the calorimetric measurement of the ^{163}Ho energy spectrum to deduce an effective electron neutrino mass. Already proposed in 1982 by DeRujula the experimental requirements for such a measurement to provide meaningful results were such high, that detector technologies had to develop for quite a long time, until the first approaches towards a realistic neutrino mass could be made. Here the fantastic results of low temperature detectors in terms of energy resolutions below 2 eV for 6 keV photons triggered a new era of projects on the hunt for a sub-eV sensitivity on the electron neutrino mass.

In the middle of this interesting period, where the technical developments are far enough to tackle a finite neutrino mass, falls this thesis as contribution to the ECHo project which aims to provide a sub-eV sensitivity on the effective electron neutrino mass via the calorimetric measurement of the ^{163}Ho energy spectrum. This thesis contributes basically by three measurements to the ECHo project.

In chapter 2 the motivation of this thesis and integration in the current research landscape is given. We start from the suggestion of the neutrino, pass by the neutrino oscillations which demonstrated that neutrinos are massive particles and discuss the approaches to determine the absolute neutrino mass scale. In the end an overview over the ECHo project will be given, where this thesis is embedded. A special focus is here on the experimental side of this journey.

In chapter 3 the general concept of the in this thesis used low temperature detectors (metallic magnetic calorimeters) is given. Here all relevant theories to describe and operate the MMCs are shortly discussed. Furthermore, we discuss the thermodynamic properties of ^{163}Ho implanted in Au, which is of special interest for the optimization of the detectors, since the used detectors have ^{163}Ho implanted in their gold absorbers, which might influence their performance.

The technical aspects of the used low temperature detectors are discussed in chapter 4, together with the non-standard parts of the read out chain. In particular will be presented the used detector designs, the applied SQUID read out schematic and a small introduction to the pre and post processing of such an MMC detector chip, needed to implant ^{163}Ho into the Au absorbers.

In chapter 5 the measurement of the contribution to the total detector heat capacity due to implanted ^{163}Ho -ions is discussed. The determination of the specific heat per ^{163}Ho -ion has important consequences for the optimization of MMCs used for the ECHo experiment. In particular this allows to define the maximum allowed activity per detector for future phases of ECHo.

A ^{163}Ho energy spectrum was measured in chapter 6 with metallic magnetic calorimeters in an underground lab in Modane. The motivation for this measurement was originally the investigation of background due to cosmic muons. The observed statistics in the spectrum and the achieved energy resolution made it possible to use this data as new input to theories describing ^{163}Ho .

In chapter 7 the measurement of a high statistic ^{163}Ho spectrum with a good energy resolution is presented. Due to this a new Q-value for the decay of ^{163}Ho could be deduced, new spectral features relevant for all coming ^{163}Ho theories could be observed and a preliminary limit on the electron neutrino mass could be provided.

A summary of this thesis with all achieved results is given in chapter 8.

2. Motivation

2.1 Neutrinos

In 1930 Wolfgang Pauli [Pau77] postulated an electrically neutral and very weakly interacting particle to fulfill energy conservation for the experimentally seen continuous β-decay spectrum of ^{214}Pb and ^{214}Bi measured earlier by James Chadwick in 1914 [Cha14]. Pauli named this new particle "neutron". Four years later Enrico Fermi came up with his theory of the β-decay [Fer34], including the new particle postulated by Pauli which he called "neutrino" (little neutron). Due to its only very weakly interacting nature the neutrino is very hard to detect. It took about 26 years until it was directly observed in an experiment of Clyde L. Cowan and Federick Reines [Cow56] in 1956. They used a big water tank in front of a nuclear reactor to find the electron anti neutrinos ($\overline{\nu}_e$) emitted from the reactor. The $\overline{\nu}_e$ reacted with the proton in the hydrogen and formed a neutron and a positron. The positron and an electron decayed via annihilation to two photons, which were measured using liquid scintillators. The generated light was then detected by photomultipliers. This way an energy resolution of about $\Delta E_{\mathrm{FWHM}} = 750$ keV at 0.5 MeV was achieved. The created neutron was moderated via scattering at the water nuclei to thermal neutrons. These thermal neutrons could be caught with a high probability by ^{113}Cd, which transformed under the process to ^{114}Cd and emitted photons again. This process took a few μs from the creation of the neutron to the emitted photon. Therefore a characteristic neutrino signature could be measured. The ^{113}Cd was solved in the water tank.

At that time neutrinos were assumed to interact only weak and to have a vanishing mass. They were included in theories which evolved later in the very successful standard model of particle physics as only weak interacting particles with no mass. In 1968 the Homestake experiment [Cle98] started which measured the solar neutrino flux. In the sun ν_{e} are created among many other creation process during the main energy process

$$4p \longrightarrow {}^{4}\mathrm{He} + 2e^{+} + 2\nu_e. \tag{2.1}$$

This is the net reaction of the proton-proton chain and the CNO chain. They used tetrachloroethylene tanks to measure the ν_{e} emitted from the sun. The ν_{e} was captured by ^{37}Cl and ^{37}Ar and an electron were created. This process had a rather low threshold energy of 0.814 MeV, which allowed for the first time to measure ν_{e} from the sun. Every week the tanks were filtered to extract the produced ^{37}Ar. The collected ^{37}Ar is radioactive and decays again to Cl with half-life of about 35 days. With a proportional counter it was possible to measure the number of created Ar atoms via the presented process, which allowed to calculate a emission rate of ν_{e} from the sun. The experiment took data until 1994 and defined a final electron neutrino flux of $2.56 \pm 0.16\,(\mathrm{stat.}) \pm 0.16\,(\mathrm{sys.})\,\mathrm{SNU}$. This value was compared with the theoretical expectation of $7.5 \pm 0.1\,\mathrm{SNU}$ [Bah04, TC11] and gave rise to the solar neutrino problem since this deviation between experiment and theory was confirmed by many experiments like GALLEX [Ham99], GNO [Alt05], SAGE [Abd09] and Super-Kamiokande [Abe11]. This discrepancy could be explained by neutrino oscillations, which is a concept that was already introduced by Bruno Pontecorvo in 1957 [Pon57, Pon58]. These oscillations have been experimentally proven 1998 by the Super-Kamiokande experiment [Fuk98] for atmospheric neutrinos and in 2001 the SNO experiment [Ahm01, Ahm02] proofed these neutrino oscillations also for the neutrino flux from the sun which finally solved the solar neutrino problem. They were able to measure all three neutrino flavors with a sufficient significance. For this an acrylic bowl filled with 1000 tons D_2O, surrounded by 1700 t of light water. Around the heavy water about 9600 photo multipliers were mounted. The incoming neutrinos could undergo mainly 3 different reactions. An incoming neutrino could scatter elastically on an electron, which is accelerated above the velocity of light in the water. The created Cerenkov light was detected by the photo multipliers. This process is by a factor of 7 more probable for ν_{e} then for ν_τ and ν_μ. Furthermore, an ν_{e} can do together with a neutron from the heavy water a charge current reaction, where the neutron is converted into a proton and an electron is emitted, which again produces Cerenkov light, due to its high velocity. All three neutrino flavors can disintegrate a deuterium atom. The neutron can be captured by $^{35}\mathrm{Cl}$, which excites to $^{36}\mathrm{Cl}$, which de-excites via photon emission. These photons can accelerate electrons via the Compton effect, which again leads to Cerenkov radiation. This way the rate of ν_{e} compared to the total rate of detected neutrinos from the sun could be determined. These experimental proofs were honored with the Nobel price in 2015 for the SNO and Super-Kamiokande experiment.

The existence of these neutrino flavor oscillations is explained in the quantum mechanical formalism introduced by Pontecorvo by n orthogonal mass eigenstates ν_i which are not identical to the orthogonal flavor eigenstates ν_α, but are connected by a unitary $n \times n$ mixing matrix U:

$$|\nu_\alpha\rangle = \sum_i U_{\alpha i} |\nu_i\rangle \ . \tag{2.2}$$

In the standard interpretation $\alpha = e, \mu, \tau$ and $i = 1, 2, 3$. For such a system the time evolution is given by the Schrödinger equation.

$$|\nu_\alpha(x,t)\rangle = \sum_i U_{\alpha i} e^{\mathrm{i} p_i x} e^{-\mathrm{i} E_i t} |\nu_i\rangle \ , \tag{2.3}$$

The neutrino has the energy E_i, momentum p_i and is emitted at $x = 0$. For relativistic neutrinos

$$E_i = \sqrt{m_i^2 + p_i^2} \simeq p_i + \frac{m_i^2}{2p_i} \simeq E + \frac{m_i^2}{2E} \ , \tag{2.4}$$

with $p_i \gg m_i$ hence $E \approx p_i$ as neutrino energy is a valid assumption. Combining now eq. 2.3 with the inverse of eq. 2.2

$$|\nu_i\rangle = \sum_\beta U^*_{\beta i} |\nu_\beta\rangle \tag{2.5}$$

and $L = x = t$ ($c = 1$) as the distance between source and detector we get for the time evolution of the flavor eigenstate of the neutrino:

$$\begin{aligned} |\nu_\alpha(x,t)\rangle &= \sum_{i,\beta} U_{\alpha i} U^*_{\beta i} e^{\mathrm{i}(p_i x - E_i t)} |\nu_\beta\rangle \\ &= \sum_{i,\beta} U_{\alpha i} U^*_{\beta i} \exp\left(-\mathrm{i}\frac{m_i^2}{2}\frac{L}{E}\right) |\nu_\beta\rangle \ . \end{aligned} \tag{2.6}$$

The probability for a flavor transition is then given by:

$$\begin{aligned} P(\alpha \to \beta) &= |\langle\nu_\beta|\nu_\alpha(x,t)\rangle|^2 \\ &= \sum_i \sum_j U_{\alpha i} U^*_{\alpha j} U^*_{\beta i} U_{\beta j} \exp\left(-\mathrm{i}\frac{\Delta m_{ij}^2}{2}\frac{L}{E}\right) \ , \end{aligned} \tag{2.7}$$

with the squared mass difference $\Delta m_{ij}^2 = m_i^2 - m_j^2$. This formula gives the probability for a flavor oscillation, like it was observed by SNO and Super-Kamiokande, depending on the distance L between the detector and the source, the neutrino energy E and the mass squared difference Δm_{ij}^2.

The present standard assumption is $i = 1, 2, 3$, but there exists a minimal extension of the standard model which includes right handed neutrinos, not interacting weakly but only gravitational, the so called sterile neutrinos. These particles might not only be the missing symmetry partner for the left handed neutrinos in theory but might also explain the reactor anomaly reported first in 2011 by Müller *et al.* [Mue11], if these neutrinos have a mass on a eV-scale. These reactor experiments use nuclear reactors as neutrino sources, since the fission process in the reactor creates a lot of isotopes that undergo a β-decay and emit electron anti-neutrinos. The detectors to observe neutrino flavor oscillations are then placed at different baselines L. In first approximation this data was in very good agreement with the proposed neutrino flavor oscillation theory. However, the re-evaluation of the expected neutrino flux in such a reactor by Müller *et al.* showed a discrepancy between experiment in theory for ν_e by $\approx 3\%$. This was later confirmed by Huber *et al.* [Hub11]. However the models to describe the processes in the reactor and the expected neutrino fluxes a very complicated and the precision of the measured neutrino ratio needs to be improved to proof this discrepancy.

For the $n = 3$ case parameters like Δm^2_{ij}, the mixing angles Θ_{ij} contained in the mixing matrix $U_{\alpha i}$ and the CP-violating phases δ_{CP} are determined via various experiments. Used as neutrino source is the sun, atmospheric neutrinos, accelerators and reactor neutrinos. In table 2.1 the present parameters are listed. Since all these oscillation experiments are in the end interference experiments only the value of the

NuFIT 4.0 (2018)

		Normal Ordering (best fit)		Inverted Ordering ($\Delta\chi^2 = 4.7$)	
		bfp $\pm 1\sigma$	3σ range	bfp $\pm 1\sigma$	3σ range
without SK atmospheric data	$\sin^2\theta_{12}$	$0.310^{+0.013}_{-0.012}$	$0.275 \to 0.350$	$0.310^{+0.013}_{-0.012}$	$0.275 \to 0.350$
	$\theta_{12}/^\circ$	$33.82^{+0.78}_{-0.76}$	$31.61 \to 36.27$	$33.82^{+0.78}_{-0.76}$	$31.61 \to 36.27$
	$\sin^2\theta_{23}$	$0.580^{+0.017}_{-0.021}$	$0.418 \to 0.627$	$0.584^{+0.016}_{-0.020}$	$0.423 \to 0.629$
	$\theta_{23}/^\circ$	$49.6^{+1.0}_{-1.2}$	$40.3 \to 52.4$	$49.8^{+1.0}_{-1.1}$	$40.6 \to 52.5$
	$\sin^2\theta_{13}$	$0.02241^{+0.00065}_{-0.00065}$	$0.02045 \to 0.02439$	$0.02264^{+0.00066}_{-0.00066}$	$0.02068 \to 0.02463$
	$\theta_{13}/^\circ$	$8.61^{+0.13}_{-0.13}$	$8.22 \to 8.99$	$8.65^{+0.13}_{-0.13}$	$8.27 \to 9.03$
	$\delta_{\text{CP}}/^\circ$	215^{+40}_{-29}	$125 \to 392$	284^{+27}_{-29}	$196 \to 360$
	$\frac{\Delta m^2_{21}}{10^{-5}\ \text{eV}^2}$	$7.39^{+0.21}_{-0.20}$	$6.79 \to 8.01$	$7.39^{+0.21}_{-0.20}$	$6.79 \to 8.01$
	$\frac{\Delta m^2_{3\ell}}{10^{-3}\ \text{eV}^2}$	$+2.525^{+0.033}_{-0.032}$	$+2.427 \to +2.625$	$-2.512^{+0.034}_{-0.032}$	$-2.611 \to -2.412$
		Normal Ordering (best fit)		Inverted Ordering ($\Delta\chi^2 = 9.3$)	
		bfp $\pm 1\sigma$	3σ range	bfp $\pm 1\sigma$	3σ range
with SK atmospheric data	$\sin^2\theta_{12}$	$0.310^{+0.013}_{-0.012}$	$0.275 \to 0.350$	$0.310^{+0.013}_{-0.012}$	$0.275 \to 0.350$
	$\theta_{12}/^\circ$	$33.82^{+0.78}_{-0.76}$	$31.61 \to 36.27$	$33.82^{+0.78}_{-0.75}$	$31.62 \to 36.27$
	$\sin^2\theta_{23}$	$0.582^{+0.015}_{-0.019}$	$0.428 \to 0.624$	$0.582^{+0.015}_{-0.018}$	$0.433 \to 0.623$
	$\theta_{23}/^\circ$	$49.7^{+0.9}_{-1.1}$	$40.9 \to 52.2$	$49.7^{+0.9}_{-1.0}$	$41.2 \to 52.1$
	$\sin^2\theta_{13}$	$0.02240^{+0.00065}_{-0.00066}$	$0.02044 \to 0.02437$	$0.02263^{+0.00065}_{-0.00066}$	$0.02067 \to 0.02461$
	$\theta_{13}/^\circ$	$8.61^{+0.12}_{-0.13}$	$8.22 \to 8.98$	$8.65^{+0.12}_{-0.13}$	$8.27 \to 9.03$
	$\delta_{\text{CP}}/^\circ$	217^{+40}_{-28}	$135 \to 366$	280^{+25}_{-28}	$196 \to 351$
	$\frac{\Delta m^2_{21}}{10^{-5}\ \text{eV}^2}$	$7.39^{+0.21}_{-0.20}$	$6.79 \to 8.01$	$7.39^{+0.21}_{-0.20}$	$6.79 \to 8.01$
	$\frac{\Delta m^2_{3\ell}}{10^{-3}\ \text{eV}^2}$	$+2.525^{+0.033}_{-0.031}$	$+2.431 \to +2.622$	$-2.512^{+0.034}_{-0.031}$	$-2.606 \to -2.413$

Table 2.1: Three-flavor oscillation parameters from a fit to global data as of November 2018. The results shown in the upper (lower) section are obtained without (with) the inclusion of the tabulated χ^2 data on atmospheric neutrinos provided by the Super-Kamiokande collaboration (SK-atm). The numbers in the 1st (2nd) column are obtained assuming NO (IO), i.e., relative to the respective local minimum. Minimization with respect to the ordering provides the same results as Normal Ordering, except for the 3σ range of Δm^2_{3l} in the analysis without SK-atm. Note that $\Delta m^2_{3l} = \Delta m^2_{32} > 0$ for NO and $\Delta m^2_{3l} = \Delta m^2_{32} < 0$ for IO. This table was taken from [Est19].

mass squared difference of the neutrino masses can be known.

For Δm_{3l}^2 only the absolute value is known and therefore a normal ordering for the neutrino masses and an inverted ordering is allowed ($m_1 < m_2 < m_3$ vs. $m_3 < m_1 < m_2$). Since only Δm_{ij}^2 can be determined with these kinds of experiments and not the absolute mass scale which is very interesting to better understand physics beyond the Standard Model of particle physics a lot of experiments have started to investigate the absolute neutrino mass scale. There are basically three major ways to determine the absolute neutrino mass. The study of the distribution of matter in the universe which is sensitive to the sum of the neutrino mass eigenstates. The search for the neutrinoless double beta decay, which is possible if neutrinos are massive. The measurement of the half-life of the neutrinoless double beta decay can be transduced to an effective Majaorana mass and the investigation of the end point region of electron capture or β-decays, where an neutrino is emitted and the spectral shape of the energy spectrum of the decay is dependent on an effective neutrino mass. In the following these three methods are described in a bit more detail.

2.1.1 Neutrinoless double beta decay - $0\nu\beta\beta$

The observation of the neutrinoless double beta decay allows to determine the mass scale of the effective Majorana mass $m_{\beta\beta}$. During a double beta decay two electrons and two electron anti-neutrinos are emitted

$$^{A}_{Z}X_N \longrightarrow ^{A}_{Z+2} X_{N-2} + 2e^- + 2\bar{\nu}_e \quad . \tag{2.8}$$

The resulting energy spectrum of the summed electrons is continuous and very similar to the one of a single beta decay. The half-life of this process is in the range of $t_{1/2} = 10^{18} \ldots 10^{22}\,\mathrm{y}$. A neutrinoless double beta decay is described by:

$$^{A}_{Z}X_N \longrightarrow ^{A}_{Z+2} X_{N-2} + 2e^- \quad . \tag{2.9}$$

It is the result of the theory developed by Ettore Majorana [Maj37], where neutrinos are their own anti-particles. This idea was modified for the neutrinoless double beta decay by Wendell H. Furry [Fur39] in a way that during a decay not two anti-neutrinos are emitted but a virtual light Majorana neutrino is exchanged which leads to the neutrinoless double beta decay. The signature of such a process in the measured energy spectrum of the two electrons would be an additional peak at the end-point of the beta spectrum since the two electrons have to share the total energy available for the decay. If a $0\nu\beta\beta$-decay is detected, the half-life $T_{1/2}^{0\nu\beta\beta}$ of this process, respectively the decay rate $\Gamma^{0\nu\beta\beta}$ would give the absolute scale of the effective Majorana mass $\langle m_{\beta\beta}\rangle = |\sum_i U_{ei}^2 m_i| = \sum_i |U_{ei}^2|\, m_i e^{i\beta_i}$.

$$\Gamma^{0\nu\beta\beta} = \left(T_{1/2}^{0\nu\beta\beta}\right)^{-1} = G^{0\nu\beta\beta}(Q_{\beta\beta}, Z)|M^{0\nu\beta\beta}|^2 \frac{\langle m_{\beta\beta}\rangle}{m_e^2} \ . \tag{2.10}$$

$G^{0\nu\beta\beta}(Q_{\beta\beta}, Z)$ is the integral over the phase space of the two electrons. $Q_{\beta\beta}$ is the end-point energy of the decay. The three neutrino mass eigenstates are m_i and $U_{\alpha i}$ are the mixing matrix elements. m_e is the electron mass and β_i the Majorana phases, introduced in the Majorana formalism. $M^{0\nu\beta\beta}$ are the nuclear matrix elements (NMEs) that need theoretical input and currently present the largest uncertainty in the calculation of $\langle m_{\beta\beta}\rangle$.

There exist many experiments that search for the $0\nu\beta\beta$-decay with different isotopes that undergo a $\beta\beta$-decay. The choice of a specific isotope needs the consideration of certain parameters, like the natural abundance, how easy it can be enriched and many more. Here ^{136}Xe is a very good candidate since its gaseous and can therefore be enriched very easy. Experiments like KamLAND-Zen and EXO-200 use ^{136}Xe. While KamLAND-Zen measures the decay of ^{136}Xe with photomultiplier's mounted around a transparent balloon filled with a ^{136}Xe loaded liquid scintillator in EXO-200 a time projection chamber is used to detect the decay. The best limit on $m_{\beta\beta}$ is derived from KamLAND-Zen data combined with some theoretical considerations on the NMEs with $m_{\beta\beta} < 0.15\,\text{eV}$ 90 % C.L. [Cap17].

Of course there exist many more experiments using other isotope that undergo $2\nu\beta\beta$-decay like GERDA using ^{76}Ge and measuring consequently with germanium detectors or AMORE which embeds ^{100}Mo in scintillating crystals which are then read out by low temperature calorimeters.

.

2.1.2 Cosmology

Neutrinos are the most abundant particles in the observable universe and are fundamental particles in the standard model of particle physics. Therefore they play an important role for several cosmological effects. In most cosmological theories they were created during the big bang and decoupled from the plasma with a temperature of $T = 1.95\,\text{K}$, which translates in an energy of $E \approx 0.17\,\text{meV}$. A total number density of $336\,\text{cm}^{-3}$ combined for the three flavors and including both neutrinos and anti-neutrinos is expected as cosmic neutrino background.

The observable effects are for example the clustering of matter in the universe over large scales and anisotropies in the spectrum of the cosmic microwave background (CMB).

In general are the results for the sum of the three mass eigenstates dependent on the exact cosmological model that is used as well as the data that is included. The standard ΛCDM model can be extended by several parameters and constraints, which can be motivated by recent measurements. Furthermore, can data sets in addition to the temperature angular power spectrum of the CMB be added. Typically data from the Planck satellite is used. The results for the sum of the neutrino mass eigenstates [RC19] are given with:

$$\sum m_i \leq 0.121...0.172\,\mathrm{eV}\ (95\,\%\ \mathrm{C.L.})\ . \tag{2.11}$$

2.1.3 Kinematic measurements

The above obtained results are based on a quite elaborate model and assumptions made in the analysis. Nevertheless, they are for sure model dependent. Therefore, it is desirable to find a way to compare these results with a different kind of measurement that is not as heavily model based, which can be found in the measurements based on neutrino kinematics.

A third method to determine the neutrino mass is the kinematic approach, which is considered to be model independent. Here only energy and momentum conservation are considered. In principle there are two experiments one can think of, which are time-of-flight measurements and the weak nuclear decay to determine a neutrino mass.

The basic idea of time-of-flight measurements is that the traveling time over a distance d for massive particles will differ from d/c for photons. Therefore, a long baseline d, a strong neutrino and photon source and a suitable detector are needed. A core-collapse supernova is a good candidate for such an high intensity source with a long baseline. To perform this measurement a new born supernova needs to be detected and observed with telescopes. This is done by the "Supernova Early Warning System" (SNEWS) [Ant04], which was formed exactly for such purposes. After the light signal is detected it takes typical several days until the neutrino signal is expected. This gives the possibility to prepare the neutrino detectors for the event.

The birth of a supernova is of course a very rare event, which needs to be recognized in time. That's why the only successful time-of-flight analyses has been done after the supernova SN1987A in the Large Megellanic Cloud which gave a limit of $m_\nu < 5.7\,\mathrm{eV}$ (95% C.L.) [Lor02]. There exist as well long baseline experiments located on earth with neutrinos produced with an accelerator like MINOS and OPERA [Acq09], but the sensitivity on the neutrino mass is not as good due to the way shorter baseline. With the technology given today the only competitive approach seems to be the search for new supernovae. Although the sensitivity will not reach the sensitivity of cosmological experiments or direct neutrino mass measurements on weak nuclear decays due to the up to now large systematic uncertainties in the theoretical models of a core-collapse supernova.

The weak nuclear decay is another option for direct neutrino mass determination. Both the β-decay and the electron capture (EC) are used. During this processes an neutrino/anti-neutrino is emitted together with other particles. If now the energy distribution of the other particles is measured very precisely, having a good energy resolution, low background and high statistics a neutrino/anti-neutrino mass can be deduced if the theoretical description of the process is well understood. The spectral shape will differ, for different neutrino/anti-neutrino masses.

There are many candidates that undergo a β-decay, preferable is here a low Q-value which determines the available energy for the decay. It is given by the mass difference between the mother atom and the daughter atom of the decay. In the past mostly ^{3}H (β-decay) and ^{163}Ho (EC) have been used due to their rather low Q-value.

The tritium β-decay is a prominent candidate since it provides the currently best limit on the electron anti-neutrino mass.

$$^3\mathrm{H} \longrightarrow {}^3\mathrm{He} + e^- + \bar{\nu}_e \tag{2.12}$$

It is a super allowed transition, which means the spectral shape can be described mainly by Fermi's Golden rule. Tritium has a half-life of $T_{1/2} = 12.3\,\mathrm{y}$ and a $Q_\beta = 18.6\,\mathrm{keV}$. It can be acquired in reasonable amounts from heavy water moderated fission reactors. Furthermore, decades of experience with handling this radioactive material exist. All these factors make the Isotope very attractive for a neutrino mass experiment. The best limit on the electron anti-neutrino neutrino mass at this point is

$$m(\bar{\nu}_e) \leq 2.0\,\mathrm{eV}\ (95\,\%\ \mathrm{C.L.})\ . \tag{2.13}$$

This is a combined result [Ber12] from two experiments, one located in Mainz [Kra05], the other one located in Troisk [Ase11]. Both experiments used a Magnetic Adiabatic Collimation with an Electrostatic Filter (MAC-E-Filter) to measure the β-decay spectrum. This technique was developed by Kruit and Read [Kru83] and later adapted for higher energies [Pic92] including the 18.6 keV end-point region of the ^{3}H spectrum. With this technique the electrons emitted during the β-decay are guided adiabatically through a magnetic field on to a counting detector. Their momentum is also adiabatically changed to point aligned with the magnetic field onto the detector. Furthermore, a retarding potential is applied for the electrons which allows only electrons to pass the filter with an energy higher the retarding potential. This way a integrated ^{3}H spectrum can be measured. The difference between the experiments was in the tritium source. The experiment located in Troisk used molecular tritium

$^3H_2$ in its gaseous form in a windowless gaseous tritium source. An upper limit of $m(\bar{\nu}_e) \leq 2.05\,\mathrm{eV}$ (95 % C.L.) [Ase11] was found. The Mainz experiment used a thin film of molecular tritium on a cold graphite substrate as source. They were able to reach an upper limit of $m(\bar{\nu}_e) \leq 2.3\,\mathrm{eV}$ (95 % C.L.) [Kra05].

The KATRIN experiment is a follow up of the Mainz and Troisk experiments actually using the old setup from Troisk in a refined version a pre-spectrometer for their new MAC-E-Filter with a diameter of 9.8 m and a length of 23.3 m. They use as well a windowless gaseous tritium source. With this new set up they will be able to set a new limit on the electron anti-neutrino mass [Ang05] of:

$$m(\bar{\nu}_e) \leq 0.2\,\mathrm{eV}\ (90\,\%\ \mathrm{C.L.})\ . \tag{2.14}$$

KATRIN has started the first data taking with ^{3}H beginning of this year. The new limit is expected after 3 years of data taking. Another promising candidate is Project 8 [Esf17], which also uses ^{3}H as source material. Here the emitted electrons are captured in a magnetic bottle. Due to the external magnetic field they will move with a cyclotron frequency which depended on their energy. The emitted radiation from this motion is then picked up by antenna and read out. They aim to have a vacuum vessel filled with $10^{-7} - 10^{-6}\,\mathrm{mBar}$ of $^3\mathrm{H}_2$ gas in a 1 T magnetic field. This way they aim to reach a sensitivity of

$$m(\bar{\nu}_e) \leq 0.04\,\mathrm{eV}\ (90\,\%\ \mathrm{C.L.})\ . \tag{2.15}$$

With this precision they explore a parameter space for the anti neutrino mass, that is not ruled out with a high probability by cosmology and they might be able to solve the question for a inverted or normal hierarchy. Up to this point they have seen first measured signals from their setup, showing the cyclotron frequency of a single electron.

Other β-decay candidates are ^{115}In and ^{187}Rn, which have a very low Q-value. The Q-value for ^{115}In is $Q_\beta = (155 \pm 24)\,\mathrm{eV}$ [Mou09] for the interesting decay path to excited ^{115}Sn which is very preferable. Anyhow, this decay path has only a branching ratio of about 10^{-6} [Wie09]. Most of the β-decays will end already in the ground state of ^{115}Sn. Furthermore, the decay to the excited state has a lifetime of about $10^{20}\,\mathrm{y}$ [Wie09]. These two facts make it experimentally very challenging to get a calorimetric measurement of the β-decay to the excited state. In principle can the decay to the excited state be recognized by the coincident de-excitation γ-ray of the ^{115}Sn nucleus, but it has to be identified between about 10^6 other decay electrons from the β-decay to the ground state. The other candidate with low Q-value is ^{187}Rn with $Q_\beta = 2.47\,\mathrm{keV}$ and a half-life of $T_{1/2} = 4.3 \times 10^{10}\,\mathrm{y}$. Here the β-decay to ^{187}Os is in first order forbidden which leads to a quite complex spectral shape for the energy spectrum [Dvo11]. The challenge here is to extract the electrons from the β-decay since already a very thin foil of ^{187}Rn will cause self-absorption of the electrons within the source. Thats why a calorimetric measurement is done where the source is spread between several detectors. In the 1980s [McC84] it was suggested to use thermal micro-calorimeters to measure the ^{187}Rn decay spectrum. This idea was followed by two experiments MANU and MIBETA.

The MANU experiment used metallic Re absorbers with the intersting ^{187}Rn already inside. For the read out out they used Neutron Transmutation Doped (NTD) Ge thermistors and found with these an upper limit [Gat01] of

$$m(\bar{\nu}_e) \leq 26\,\mathrm{eV}\ (95\,\%\ \mathrm{C.L.})\ . \tag{2.16}$$

The MIBETA experiment [Sis04] used AgReO$_4$ crystals read out with Si thermistors, which allowed to provide a limit of

$$m(\bar{\nu}_e) \leq 15\,\mathrm{eV}\ (90\,\%\ \mathrm{C.L.})\ . \tag{2.17}$$

Within this measurement, they were able to achieve an energy resolution of $\Delta E_{\mathrm{FWHM}} = 28.5\,\mathrm{eV}$ at $2.47\,\mathrm{keV}$.

This good results combined with the very good detector performance lead to the "Micro-calorimeter Arrays for a Rhenium Ex- periment" (MARE) collaboration [Nuc08]. MARE plans to use large arrays of low temperature micro calorimeters to measure the β-decay spectrum The AgReO$_4$ crystals and the ^{187}Rn absorbers are both under investigation, as well as a proper read out technique which is able to achieve an energy resolution of about $\Delta E_{\mathrm{FWHM}} \approx 1\,\mathrm{eV}$ and a signal rise time of $\tau_{\mathrm{rise}} \approx 1\,\mu\mathrm{s}$. ^{187}Rn absorbers have problems with a complicated and long thermalization of energy in the superconducting absorber, which decreases the performance of any considered detector technique [Por11, Fer12, Ran12]. The detector of choice are Si:P thermistors coupled to AgReO$_4$ crystals [Fer14], which would allow to achieve a limit on th electron anti-neutrino mass of

$$m(\bar{\nu}_e) \leq 4.5\,\mathrm{eV}\ (90\,\%\ \mathrm{C.L.}) \tag{2.18}$$

The investigation on ^{187}Rn as β-decay candidate are ongoing, but at the present status the detector numbers and performances are not suitable to reach a sub-eV sensitivity on the electron neutrino mass.

A very promising candidate for an electron capture is ^{163}Ho , which is used for the here presented measurements. In the following a short overview of ^{163}Ho as candidate for a sub-eV sensitivity electron neutrino mass measurement will be given.

2.2 Brief history of ^{163}Ho

Among the many nuclide's that undergo an electron capture ^{163}Ho is one of the best candidates for determination of the neutrino mass since it has the lowest Q_{EC}-value with 2.833 keV [Eli15]. This is advantageous since all used detectors have a relative spectral resolving power and a low Q_{EC}-value allows for a good absolute energy resolution close to the end point region of the measured energy spectrum, where the biggest influence due to a non-zero neutrino mass is expected. Furthermore, is a small energetic distance between the last main resonance of the decay and the Q_{EC}-value preferable, since then a larger fraction of total counts is in the end point region (ROI), which allows gathering faster/easier the needed statistics. ^{163}Ho decays via an electron capture, where the electron is captured from an inner shell into the nucleus. There a proton and the electron form a neutron and an electron neutrino ν_e is created. The new daughter atom is excited Dysprosium Dy*.

$$
\begin{aligned}
{}^{163}_{67}\mathrm{Ho}_{96} &\longrightarrow {}^{163}_{66}\mathrm{Dy}^*_{97} + \nu_{\mathrm{e}} \\
&\hookrightarrow {}^{163}_{66}\mathrm{Dy}_{97} + \mathrm{E}
\end{aligned}
\tag{2.19}
$$

The excited Dysprosium de-excites over various channels like x-ray emission, Auger electrons and Koster-Kronig transitions. The de-excitation energy is E. The total available energy for this decay is called Q_{EC}-value and is given by the mass difference between ^{163}Ho and ^{163}Dy. This value is $Q_{\mathrm{EC}} = 2.833 \pm 0.030^{\mathrm{stat}} \pm 0.015^{\mathrm{syst}}\,\mathrm{keV}$ [Eli15] measured by Penning trap mass spectrometry. The half life of the decay is $T_{1/2} = 4570 \pm 50\,\mathrm{years}$ [Bai83]. In principle is the dominant part of the energy spectrum given by the non radiative electron capture process described by resonances with energies corresponding to the energy levels of the captured electrons. As can be seen in figure 2.1. The resonances are described by a Lorentzian line shape with a position E_H and the line width Γ_H. The names of the peaks MI, MII, ... correspond to the position of the electron in the shell where it was captured from. The amplitude is given by the squared electron wave function at the position of the nucleus $\psi_H^2(0)$ which represents the capture probability for this electron. B_H is an overlap and exchange correction which theory dependent since several approximations have to be made to calculate this value. The sum of the resonances needs then to be multiplied by the phase space factor for this decay. It contains the maximum energy of the decay Q_{EC} and the effective electron neutrino mass $\mathrm{m}_{\nu_{\mathrm{e}}}$. Together with a scaling factor A which scales with the number of measured events the probability W to find an event with energy E_{EC} is given by:

$$
\frac{\mathrm{d}W}{\mathrm{d}E} = A(Q_{\mathrm{EC}} - E)^2 \sqrt{1 - \frac{m_\nu^2}{(Q_{\mathrm{EC}} - E)^2}} \sum_H B_H \psi_H^2(0) \frac{\frac{\Gamma_H}{2\pi}}{(E - E_{\mathrm{H}})^2 + \frac{\Gamma_H^2}{4}}. \tag{2.20}
$$

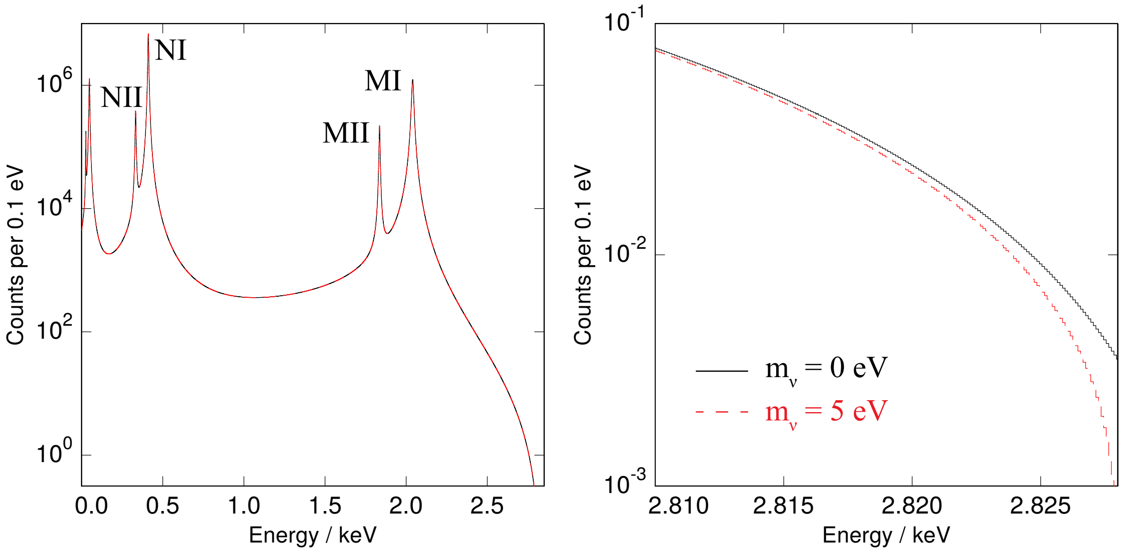

Figure 2.1: Simple 7 resonances ^{163}Ho theory with $Q_{\mathrm{EC}} = 2.833\,\mathrm{keV}$ and $\mathrm{m}_\nu = 0\,\mathrm{eV}$ (solid black) and $\mathrm{m}_\nu = 5\,\mathrm{eV}$ (dashed red).

So in principle is the spectral shape of the decay dependent on the effective electron neutrino mass. This was abused already a long time ago by a group from the Department of Physics and Chemistry of Princeton University [Ben81]. At these days basically two ideas were followed to extract from a ^{163}Ho decay spectrum a limit on the electron neutrino mass. The first one is the measurement of the de-excitation x-ray spectrum, which is of course depended on the effective electron neutrino mass as well. Only a tiny fraction of the total spectral weight goes into these x-rays. The corresponding spectrum shows as peak position energies the differences of the energy levels in the excited dysprosium. A ^{163}Ho source was and put in front of a silicon detector to measure the escaping x-rays. These measurements [Ben81, And82, Yas83] were able to provide a limit on the effective electron neutrino mass with $m_\nu < 490\,\mathrm{eV}$ 68 % C.L. [Yas94] by measuring the ratio of the x-ray multiplets corresponding to a electron hole in the M and N shell of ^{163}Ho . These measurements were not prolonged, since the energy of the electron levels in Dy needs to be known very precisely. Besides the fact that the ^{163}Ho x-ray spectrum needs to be measured very accurate, it was doubted at that time that these energy levels in excited Dy will be known with high enough precision to give a relevant upper limit on the electron neutrino mass. The other idea that was followed was the measurement of an IBEC spectrum. The capture electron will see on his way to the core during the EC process the electrical field of the core and might produce Bremsstrahlung. Again this IBEC spectrum will be dependent on the effective electron neutrino mass. This method still gives the best limit on the effective electron neutrino mass with $m_\nu < 225\,\mathrm{eV}$ 95 % C.L. [Spr87] in a kinematic approach. The energy resolution for the used Si(Li) detectors was about $\Delta E_{\mathrm{FWHM}} \approx 137\,\mathrm{eV}$ at $2\,\mathrm{keV}$.

In the year 1981 DeRujula [DR81] made the suggestion to measure a precise ^{163}Ho energy spectrum calorimetrically, to deduce an electron neutrino mass. This requires an implantation into suitable detectors in a way that the whole de-excitation energy E is measured. The idea was, that the effective electron neutrino mass can be measured as difference between Q_{EC}-value of the decay and the maximum of E. Any uncertainties in branching ratios, peak position and effects like the self-absorption in the ^{163}Ho source are avoided. The theoretical description given above was sufficient for a long time, for example for the first calorimetric measurement of ^{163}Ho by a group from Aarhus University and the ISOLDE group [Lae84]. They implanted the ^{163}Ho into a Si(Li) detector. These detectors were operated at liquid nitrogen temperature $T = 77\,\mathrm{K}$. A detector problem lead to $\Delta E_{\mathrm{FWHM}} \approx 380\,\mathrm{eV}$ at the MI line, which was much worse than the measured energy resolution for a ^{1}37Cs calibration source with $\Delta E_{\mathrm{FWHM}} \approx 75\,\mathrm{eV}$. Furthermore, seemed to occur an incomplete charge collection in the Si(Li) detector, which was recognized by small shifts towards lower energies of the main resonance lines. It seemed that the implantation process did introduce several defects in the detector.

A second measurement was done by a group from Princeton University [Har92]. They used a gas proportional counter where the ^{163}Ho -ions are bound in volatile fluorooctanedione. This experiment had an energy resolution of about $\Delta E_{\mathrm{FWHM}} \approx 940\,\mathrm{eV}$ at $5.89\,\mathrm{keV}$ measured with an ^{55}Fe calibration source.

The next experiment was done by a group from Genoa University [Gat97] using for the first time a micro calorimeter. They put liquid ^{163}Ho in a α-HIGA solution (2-Hydroxyisobutyric acid) and let a drop dry between two tin foils to achieve a quantum efficiency close to 100%. This absorber was mounted on a NTD Ge thermistor operated at about $T \approx 55\,\mathrm{mK}$. For this setup energy resoltions of $\Delta E_{\mathrm{FWHM}} = 50\,\mathrm{eV}$ at the N-lines and $\Delta E_{\mathrm{FWHM}} = 100\,\mathrm{eV}$ at the M-lines where achieved. Here for the first time the sub-shell peaks MI, MII and NI, NII could be observed and the great potential of micro calorimeters in terms of energy resolution could be seen. This triggerd new approaches to describe theoretically the ^{163}Ho energy spectrum.

In 2015 Robertson [Rob15] proposed to take higher order excitations during the electron capture process into account, since they also can be relevant at the end-point region. The detectors where in principle developed that far, that in terms of energy resolution and statistics these additional structures due to higher order processes can be seen. And of course they will play an important role in any determination of the electron-neutrino mass due to a difference in spectral shape of ^{163}Ho . He focused on two hole excitations, where not only one hole in the shell of the excited Dy* is created but a second hole is created by a shake-up process. There an electron is excited into a higher shell. Of course such an event is less probable and gives rise to additional discrete peaks with a position corresponding to the created holes. This is possible due to the fact that the surrounding electron system cannot follow the capture adiabatically. To give a first estimate on how big this effect he included it in a calculation for xenon (Z=54). Although this was a very rough approximation it already could explain an excess of counts between 400 eV and 600 eV, seen in experimental data. This triggered a lot more theoretical work on ^{163}Ho . Fäßler et al. calculated the two hole excitation ^{163}Ho energy spectrum [Fae14] in a more refined version. He also included at some point three hole excitations [Fae15]. In 2015 De Rujula et al. [DR15] included as well a shake-off process, where the second electron is not excited to a bound state of the atom, but to the continuum. This gives rise to high energy shoulders to every higher order resonance.

In 2014 a measurement of ^{163}Ho with fully micro fabricated metallic magnetic calorimeters (MMC) has been done [Ran17], showing that these detectors are suitable to push the energy resolution and the statistics of the spectrum to a limit, where an actual impact on the sensitivity of the effective electron neutrino mass can be reached. The achieved energy resolution was $\Delta E_{\mathrm{FWHM}} = 12\,\mathrm{eV}$. With this measurement the foundation of the ECHo experiment was laid. In parallel two other big experiments have formed, which follow the same approach as ECHo, measuring the decay of ^{163}Ho calorimetrically with cryogenic detectors to reach a sub-eV sensitivity on the effective electron neutrino mass, which are HOLMES and NuMECS. The "Electron Capture Decay of ^{163}Ho to Measure the Electron Neutrino Mass with sub-eV Sensitivity" (HOLMES) experiment [Alp15] uses TES as low temperature detectors as well as the "Neutrino Mass via Electron Capture Spectroscopy" (NuMECS) experiment [Cro14].

2.3 ECHo

The **E**lectron **C**apture ^{163}**Ho** experiment (**ECHo**) aims to measure the electron neutrino mass with a sub-eV sensitivity. This will be achieved with a high statistic and high energy precision measurement of the ^{163}Ho electron capture spectrum. A detailed description of the whole project can be found in [Gas17], here only the main ideas are given.

Such a low sensitivity needs a good energy resolution in the end point region, thats why low temperature metallic magnetic calorimeters (MMCs) [Fle09] are used. The ^{163}Ho source will be implanted in the absorbers of these detectors to reach a quantum efficiency close to 100 %. But not only fast detectors with a good energy resolution are needed to reach a sub-eV sensitivity on the electron anti neutrino mass. In addition a pure ^{163}Ho -source needs to be produced and implanted into the detectors, a good theoretical understanding of the spectral shape of the ^{163}Ho -decay needs to be reached and the Q_{EC}-value needs to be precisely measured to keep the systematics due to this value low. And of course any background sources need to be kept minimal. This thesis was performed after the first measurements of ^{163}Ho with MMCs have been performed within this project. This was the so called ECHo-1k phase, were mainly proof of principles and scalability of certain approaches were the aim to reach the next phase called ECHo-1M. Sensitivity studies have shown that 10^{14} counts in total are needed to have in the ROI, which is probably 1 eV below the Q_{EC}-value, about 10 counts. This number of counts is sufficient to reach a sub-eV sensitivity. To reach this number of counts in a reasonable time about 1 MBq of ^{163}Ho will be measured over 3 years. In the following the main aspects to reach a sub-eV sensitivity will be shortly presented.

2.3.1 Dedicated ECHo MMCs with implanted ^{163}Ho

The used detectors for the ECHo experiment have to fulfill certain constrains to reach a sub-eV sensitivity on the electron anti neutrino mass [Gal12]. They need to have a good energy resolution of $\Delta E_{\mathrm{FWHM}} < 5\,\mathrm{eV}$ to avoid smearing the ROI. They need to have a very good linearity to define precisely the energy scale of the measured ^{163}Ho spectrum. And they need to have a quite fast signal rise time τ_r to reduce an intrinsic background source, the unresolved pile-up events. Unresolved pile-up events occur if two events happen so close in time (within τ_r) that the signals can't be recognized as two, but they are recognized as one event with an energy equal to the sum of the two signals. The fraction of unresolved pile-up events f_{upu} is given with $f_{upu} = a \cdot \tau_r$. With a typical detector rise time $\tau_r = 1\,\mu\mathrm{s}$ an activity per detector of $a = 10\,\mathrm{Bq}$ is allowed. Therefore, 10^5 detectors are needed in total to reach the 1 MBq of total activity. The activity a per detector is limited as well by the additional heat capacity introduced by the implanted ^{163}Ho as will be discussed in chapter 3.5. The heat capacity of the detector is a crucial parameter for the energy resolution as will be explained in chapter 3.4.3. A study on this effect and the consequences for ECHo is part if this thesis. To reach an absorption efficiency for the ^{163}Ho decay energy close to 100%, in particular for the photons, the ^{163}Ho is encapsulated in the gold absorber of the detector. The thickness of this absorber needs to be optimized, since more material to reach the 100% also brings additional heat capacity to the system.

For this thesis within the ECHo-1k phase a classical read-out scheme was used for the detectors, where all connected detector channels are read out in parallel. For ECHo-1M with the large number of 10^5 detectors another approach needs to be established. The detectors need to be able to be somehow multiplexed.

All these requirements can be fulfilled with MMCs, which are used for the ECHo experiment. A detailed description on how MCCs work will be given in 3. The best MMCs have reached a spectral resolving power of above 3000, with an energy resolution of $\Delta E_{\mathrm{FWHM}} = 2\,\mathrm{eV}$ at 6 keV and a signal rise time of $\tau_r = 90\,\mathrm{ns}$ [Kem18].

These are the constraints for the ECHo-1M phase, which aims for a sub-eV sensitivity. The ECHo-1k phase has less strong constraints, since the aim is to improve the limit of the neutrino by about one order of magnitude.

.

2.3.2 Multiplexing within ECHo

As described in the previous section a multiplexing technique is necessary to read out the 10^5 detectors. Within the ECHo collaboration the microwave SQUID multiplexing scheme [Mat11] for MMCs has been implemented. Here every detector is inductively coupled to a non-hysteretic, un-shunted rf-SQUID. This is coupled to a superconducting microwave resonator, which has a high internal quality factor and a unique resonance frequency for each single detector. A detector signal causes a change of the magnetic flux in the SQUID which leads to a change of the effective inductance of the SQUID. Due to mutual interaction this changes the resonance frequency of the corresponding resonator. This change of resonance frequency is monitored simultaneously for all channels by measuring the transmission of a frequency comb containing the resonances send down a common transmission line capacitively coupled to each resonator. A first proof of principle has already been provided with a detector suitable for the ECHo experiment reaching an energy resolution of $\Delta E_{\mathrm{FWHM}} = 19$ eV at 5.89 keV and a signal rise time of $\tau_r = 130\,\mathrm{ns}$. An overview on the low temperature part of this technique can be found in [Kem13]. A more detailed discussion can be found in [Weg18]. The room temperature electronics itself are very complex as well since they need a high precision and they need to be very fast to keep the detectors performance. Furthermore, they need to be scalable to 10^5 detectors.

2.3.3 ^{163}Ho source production and implantation

To reach the 1 MBq of total activity at least $\approx 2^{17}$ ^{163}Ho atoms are needed, ignoring implantation efficiencies and additional tests. Due to its half-life of 4590 y ^{163}Ho has no relevant natural abundance and needs to be produced. For ECHo this is done by thermal neutron activation of enriched ^{162}Er targets in the research reactor of ILL, Grenoble. During this activation ^{163}Er is produced with an half-life of 75 minutes. This decays to ^{163}Ho . The this way produced sample still contains relevant amounts of radioactive nuclide's which spoil the ^{163}Ho energy spectrum.

Therefore a very careful chemical separation needs to be done, in order to remove all non Holmium nuclide's performed by a nuclear chemistry group in Mainz [Dor18]. Afterwards the sample still contains for example ^{166m}Ho, which is removed during the ion implantation of the ^{163}Ho with a mass separator RISIKO in Mainz [Kie19]. This way the radioactive contamination needs to be pushed well below the expected unresolved pile-up background. For the presented samples in this thesis a ratio of $^{163}\mathrm{Ho}\ /^{166m}\mathrm{Ho} < 10^5$ is proven. This value might be even better and will be corrected once the sufficient precision for the measuring methods is reached.

2.3.4 ^{163}Ho theory within ECHo

As described in chapter 2.2 the theoretical description of the spectral shape of the decay of ^{163}Ho is rather complicated due to the many relevant processes that can happen during the decay and the surrounding host material. So any given theory needs to describe the measured spectra not only at the end-point region very precisely , but over the whole spectral range. This is crucial to be able to deduce a electron neutrino mass from a deviation in the spectral shape at the end point region. For now a promising theory is given by [Bra18] describing the ^{163}Ho spectrum quite good. One of the aims of the measurement later on described (chapter 6) was to provide new experimental data with higher statistics and no visible radioactive contamination to give new input to theory. This was as well one of the goals of the second measurement presented in this thesis (chapter 7) with a dedicated ECHo detector, more pixels, higher activity per pixel and an improved energy resolution. A more detailed status of ^{163}Ho theories and their comparison with measured data will be given in these chapters.

2.3.5 The Q_{EC}-value of ^{163}Ho

The Q_{EC}-value is here of major importance, since it will be one major contribution to the systematics on the electron neutrino mass. Therefore, it is measured within the ECHo collaboration by a penning trap mass spectrometry, which measures precisely the mass difference between the mother atom ^{163}Ho and the daughter atom ^{162}Dy. This measurement provides an $Q_{\mathrm{EC}} = 2.833 \pm 0.030^{\mathrm{stat}} \pm 0.015^{\mathrm{syst}}$ keV [Eli15] obtained with the penning traps SHIPTRAP and TRIGATRAP. To reach a sub-eV sensitivity a novel Penning-trap mass spectrometer PENTATRAP [Gas17] will be used to reach an accuracy of about 1 eV. The actual Q_{EC}-value for ^{163}Ho decaying depends on the specific host material the ^{163}Ho is implanted in. Most probably this has no significant effect but needs to be investigated by theory. For the measurements in this thesis a Q_{EC}-value has been extracted, which is in good agreement with the Penning trap measurements.

2.3.6 Background within ECHo

Except from the already described background sources like the unresolved pile-up events and the radioactive contamination coming along with the ion implantation process some other background sources are investigated as well. Not only along with the implantation radioactive impurities can occur, but they can also be present in the surrounding materials, which are used for the experiment itself. Therefore, careful material screening for all used components is done and the used materials are chosen in advance carefully. Due to the very small relevant volume per pixel, about $10\,\mu$m $\times 200\,\mu$m $\times 200\,\mu$m and all the metal components around the detector a possible radioactive background source needs to be quite close to the detector to create a significant background. To study such effects geometrical Monte-Carlo simulation of the hole detector setup and its surroundings are performed.

Another source are cosmic muons that might directly hit the detector and cause an event or hit the surroundings and the following shower creates events. A direct absorber hit will cause in the majority of the cases a detector signal, which differs in shape from a ^{163}Ho decay signal. If the incoming moun has enough energy to reach the absorber it will most probable not be completely stopped by the $5\,\mu$m thick Au absorber but will also deposit energy in the underlying sensor and the substrate underneath. This changes the signal shape significant since the energy deposition is in all systems almost instant and additional sub system with a heat capacity and a coupling constant to the detector play a role. The production of secondaries which hit in showers with an energy in the relevant region is the more probable scenario. These showers can be recognized by the comparison of timestamps of each pixel on the detector. To investigate the to be expected number of muon events a detector set up was brought to an underground lab in Modane with 4800 m of water equivalent shielding around the setup. The results obtained there, were then compared with results measured above ground and compared. The results are presented in chapter 6. In parallel an active muon veto with plastic scintillators surrounding the setup was build up and tested. If events are triggered there in coincidence with a detector event, the signal is declined.

2.3.7 ECHo-1k phase

To structure the developments towards a sub eV sensitivity on the electron neutrino mass the ECHo project has defined several phases, where certain milestones should be reached in order to scale up the experiment. During this thesis the ECHo-1k phase is running. In this phase 1 kBq of total ^{163}Ho source material was planned. As already mentioned, the planned activity of 10 Bq per detector could not be reached for this phase, but the problem will be overcome for the next phase. Due to this the total wanted activity was reduced to 200 Bq. These are planned to be distributed over about 200 detectors to measure in the end 10^{10} counts with an energy resolution of below $\Delta E_{\mathrm{FWHM}} < 10\,\mathrm{eV}$. This will allow to reduce the upper limit on the effective electron neutrino mass to $m_\nu < 10\,\mathrm{eV}$. The background level should therefore be under $BG < 1 \times 10^{-5}$ events/pixel/eV/day and the unresolved pile-up fraction should be under $f_{\mathrm{pu}} < 1 \times 10^{-5}$ for this goal. The here presented measurements already fulfill these constraints, although not yet the total statistics of 10^{10} counts are reached. As presented in this thesis, for this phase a parallel read out of the 200 detectors is foreseen. For the ECHo-1M phase the 1 MBq of total ^{163}Ho source material will be used, distributed over 100 000 detectors. Here the microwave SQUID multiplexing needs to be applied. First proof of principle and measurements have been already done with this technique [Weg18]. The number total counts will be 10^{14} and the background level and unresolved pile-up fraction need to be kept one order of magnitude lower, then for the ECHo-1k phase. As well have the detectors to achieve an energy resolution of $\Delta E_{\mathrm{FWHM}} < 3\,\mathrm{eV}$.

3. Detector principle

Due to the outstanding performance of metallic magnetic calorimeters (MMCs) experiments like ECHo are possible. They provide a very good energy resolution, a very fast signal rise time and a very good energy linearity [Kem18]. In this chapter the working principle of such an MMC will be explained as well as the relevant thermodynamic properties of the used absorber and sensor material of the detector. Since for the ECHo project the ^{163}Ho is implanted in to the Au absorbers and the thermodynamic properties of the whole detector system play an important role for the detectors' performance, the thermodynamic properties of Au:Ho are discussed, Afterwards a fundamental limit of the energy resolution of MMCs is given.

3.1 Metallic Magnetic Calorimeters (MMC)

Metallic magnetic calorimeters operated at mK temperatures are capable of measuring very precisely the energy of single particles and photons. In the following the basic principles of MMCs are explained.

In picture 3.1 a typical MMC scheme is shown. In the case of ECHo the radioactive ^{163}Ho -source is implanted in the absorber. The absorber is designed to absorb all relevant decay products. The energy E is deposited in the absorber and leads to a change of temperature ΔT. The absorber is in strong thermal contact with the sensor material, typically silver doped with a few hundred ppm of the rare earth erbium. Due to the strong thermal coupling, the whole system of sensor and absorber rises in temperature ΔT:

$$\Delta T \simeq \frac{E}{C_{\mathrm{tot}}} \ , \tag{3.1}$$

with C_{tot} being the combined heat capacity of sensor and absorber. In a first order approximation during the temperature rise ΔT C_{tot} can be considered temperature independent for $\Delta T << T$. Here T is the heat bath temperature of the MMC. Due to a weak thermal link between the sensor and the heat bath the whole system cools down again to the equilibrium temperature. Since the heat bath is kept via active cooling on a fixed temperature, the equilibrium temperature is the temperature of the heat bath.

The choice of the absorber material and its dimensions are design parameters which have to match the outer constraints given by the application. Parameters like absorption efficiency for a given energy of incoming particles or detector spectral resolution

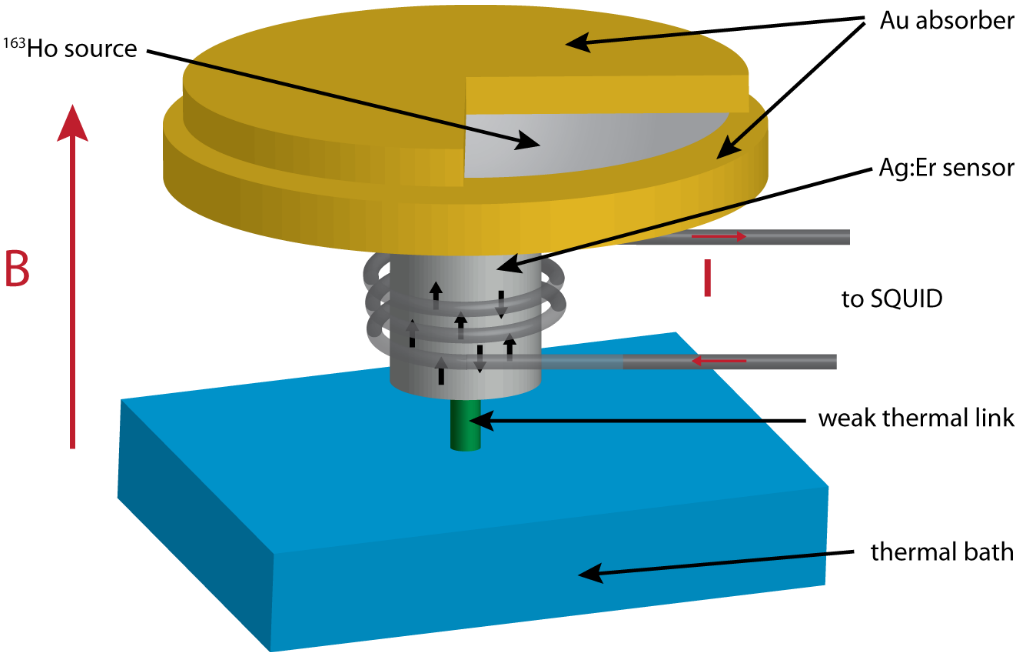

Figure 3.1: Scheme of a metallic magnetic calorimeter.

define the absorber material and geometry.

The sensor is a paramagnetic alloy, typically a few hundred ppm of the rare earth metal erbium hosted in silver (Ag:Er). This alloy is located in a small static magnetic field which induces for such materials in a temperature-dependent magnetization $M(T)$. Therefore, a temperature change ΔT ofthe complete detector leads to a change of magnetization:

$$\Delta M \simeq \frac{\delta M}{\delta T} \Delta T \, . \tag{3.2}$$

The sensor material is thermodynamically well understood [Ens00]. The change of magnetization ΔM in the sensor material can bet detected as a change of magnetic flux $\Delta\phi$ in a superconducting loop in the vicinity of the sensor. This change of magnetic flux $\Delta\phi$ results in screening currents in the superconducting loop to preserve the overall flux in the loop. This screening current leads finally to a change of magnetic flux in a Superconducting Quantum Interference Device (SQUID) which converts it to a change of Voltage ΔV.

From equation 3.1 and 3.2 it is obvious, that the expected signal size can be optimized by a small heat capacity C_{tot} and a steep magnetization of the sensor material $\frac{\delta M}{\delta T}$. Both can be achieved by low operating temperatures of the MMC as it will be explained in the next chapters. Since the absorber material and volume are defined by the experimental requirements, the heat capacity of the absorber at a given operating temperature is fixed. With this information the concentration of the Er-ions in the sensor and the sensor height for a given area of the superconducting pick up coil can be optimized.

3.2 Absorber and sensor material

MMCs can be optimized in order to achieve the required performance defined by the project. The main features that need to be considered are stopping power/quantum efficiency of the absorber together with the absorption area and the spectral resolving power. These constraints define the choice of sensor and absorber dimensions and material.

3.2.1 Au absorber

The absorber is adapted for the kind of particles and its energy to be detected. The thickness of the absorber material defines together with the material itself the stopping power which is of course energy and particle dependent. Furthermore, it defines the corresponding heat capacity C_{tot} of the detector system which is a crucial parameter since a high heat capacity decreases the signal size for a given energy (see 3.1). If the incoming particles are rare and widely distributed in emission angle it might be advantageous to have a larger absorber area to increase the detection sensitivity. A fast thermalization of the absorber material is an advantage as well, since this time can define the final signal shape of the MMC. A fast rise time is here preferable since it reduces the "dead" time of the detector. The absorber material should be such that the energy thermalization in the material occurs in a shorter time than the required time until the energy is seen by the sensor material. For the sensor material Au:Er this needs to be faster than 100 ns [Kem18]. If this would be not the case the different signal rises would create a position dependence of the deposited energy.

Furthermore, the absorber design and choice of material should be suitable for clean room processes and should allow a reliable producible.

As absorber material there exist several candidates. Dielectric materials like silicon or germanium have the advantage of a very low heat capacity compared for example to metals, since they have no contribution to the heat capacity from electrons but only from phonons which goes with $C_{ph} \propto T^3$. But for an incoming particle electron-hole pairs are created in the material. These can be trapped on lattice defects and therefore could lead to very long recombination times. In addition, every absorbed particle might create a different amount of electron-hole pairs which reduces in the end the spectral resolving power [McC93].

Superconducting materials have a relatively low heat capacity compared to normal metals below their critical temperature T_c since here as well the electrons do not contribute to the heat capacity. They are bound as bosonic Cooper pairs. Lead and tin have been used as absorber materials [Kra13, Hoo06]. Unfortunately the thermalization behavior of these superconducting metals is not fully understood [Cos93, Hen12]. One explanation for this might be broken Cooper pairs which have long relaxation and recombination times. Time scales of several hundred milliseconds have been observed.

For the detectors presented in this thesis nobel metal absorbers are used. They have a high thermal conductivity due to their free conduction electrons. This allows a fast and complete thermalization behavior. However, these electrons also provide a significant fraction of heat capacity which dominates at low temperature since it goes with $C_e \propto T$. As absorber material gold is often used due to its large stopping power and the fact that it is inert. Furthermore, it is easy to use during the detector fabrication. It is used as absorber material for the here presented detectors.

3.2.2 Ag:Er sensor

The MMCs used for this thesis have as sensor material a paramagnetic alloy of silver doped with a few ppm of the rare earth metal erbium (Ag:Er). The host material silver was introduced a few years ago which allowed to improve the detectors energy resolution [Kem18]. The standard sensor material for MMC's is Au:Er. For Au:Er a very good theory combined with numerical simulations is available which allows to predict the thermodynamic properties of the sensor, especially its magnetization behavior and its heat capacity. Both features are important for the detector design, since they influence the signal height and shape and the thermodynamic noise. In the following a very short discussion of these properties will be given. A more detailed version can be found in [Fle03]. Afterwards some experimental scaling laws are given which allow to describe Ag:Er as well with the here discussed properties of Au:Er.

For the small amounts of erbium typically used the Er forms a solid solution in which the erbium atoms occupy a regular place in the fcc lattice of the host material as can be seen in picture 3.2. The erbium denotes 3 electrons to the electron gas so that the left Er^{3+}-ions have a $[\mathrm{Kr}]4d^{10}4f^{11}5s^{2}5p^{6}$ electron configuration. This configuration provides a atomic magnetic moment due to the only partially filled $4f$ shell. Since this shell is located quite deep in the atom shielded by the outer surrounding electrons of the Er^{3+}-ion, this electron is only slightly effected by the surrounding crystal field.

For temperatures above 100 K the magnetic behavior can be described by the mag-

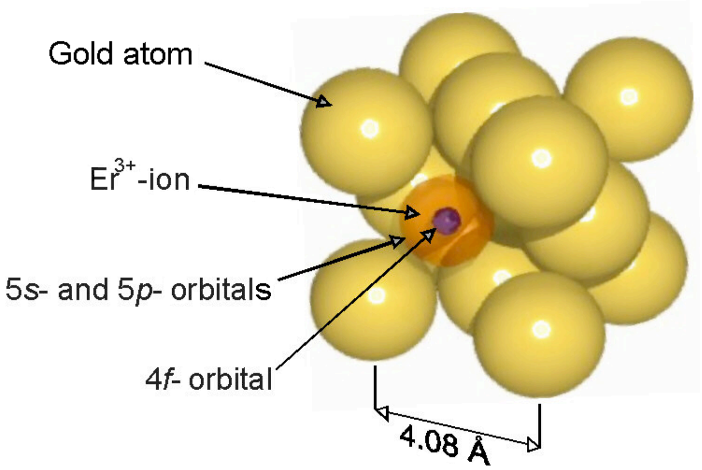

Figure 3.2: Schematic of a lattice section of the Au:Er-alloy. The Er^{3+}-ions take regular sites within the Au-lattice. The only partially filled Er $4f$-shell lies deep within the ion.

netic moment of these electrons just assuming **LS** coupling [Wil69].

$$\mu = -g_j \mu_\mathrm{B} J \ . \tag{3.3}$$

Here g_j denotes the Landé-factor, μ_B is the Bohr magneton and J is the total angular momentum. With $\mathbf{L} = 6$, $\mathbf{S} = 3/2$ and $\mathbf{J} = 15/2$ the ground state is 16-fold degenerated.

However, for lower temperatures the influence of the crystal field generated by the host material can not be neglected. The 16-fold degenerated ground state splits up. The lowest energy states are a Γ_7-Kramer-doublet. The next excited multiplet is seperated from this Γ_7-Kramer-doublet by $\Delta E/k_b = 17\,\mathrm{K}$ [Hah92] for gold and by $\Delta E/k_b = 25\,\mathrm{K}$ [Hah92] for silver. So for the typical working temperature of an MMC only the Γ_7-Kramer-doublet can be assumed to be occupied. Therefore, the hole system can be treated as 2-level-spin system with an effective spin $S = 1/2$ and an effective Landé-factor of $g_j = 6.8$ [Tao71, Abr70b].

To deduce the relevant heat capacity and magnetization some assumptions are made, which lead in the end to a very accurate description of the system on the required level. The first approach to describe the system is to consider non interacting magnetic moments, which is not true for temperatures below 100 mK depending on the erbium concentration and the applied magnetic field. The corresponding effects will be added later. For such a system the heat capacity can be described by the Zeeman splitting of the two energy levels in a B-field B. From the Helmholtz free energy F of such a micro-canonical ensemble the heat capacity can be described by:

$$C_z = -T\frac{\delta^2 F}{\delta T^2} = N k_\mathrm{B} \left(\frac{\delta E}{k_\mathrm{B} T}\right)^2 \frac{e^{\delta E/k_\mathrm{B}T}}{(e^{\delta E/k_\mathrm{B}T}+1)^2} \tag{3.4}$$

The number of Er^{3+}-ions is given by N, the energy splitting is given with $\delta E = g_j \mu_\mathrm{B} B$ and k_B is the Boltzmann constant. The heat capacity of N Er^{3+}-ions for such a two level system shows the typical Schottky anomaly with a maximum at $k_\mathrm{B} T \approx 0.42\,\delta E$ and a maximum height of $C_z \approx 0.44\,N k_\mathrm{B}$.

The magnetization of this system is given by:

$$M = -\frac{1}{V}\frac{\delta F}{\delta B} = \frac{N}{V} g_j S \mu_\mathrm{B} \mathcal{B}_S \left(\frac{g_j S \mu_\mathrm{B} B}{k_\mathrm{B} T} \right) \tag{3.5}$$

The Brillouin function $\mathcal{B}_S$ is $\mathcal{B}_{1/2}(x) = tanh(x)$ for $S = 1/2$.

This system follows the expected Curie behavior for large T, for low T more and more magnetic moments are aligned with the B-field such that the system saturates at $M = \frac{N}{V} g_j S \mu_\mathrm{B}$.

These equations can be used the overall behavior of an MMC, but quantitative deviations from measurements are still present. They can be understood by introducing a finite interaction between the magnetic moments [Sch00]. The direct overlap of the wave functions of two $4f$-electrons can be neglected. Two other interaction mechanisms can be identified, which play a major role and influence the heat capacity and magnetization of the sensor material.

The Ruderman-Kittel-Kasuya-Yoshida (RKKY) interaction [Rud54, Kas56, Yos57], which describes the interaction of two dipoles at a distance r_{ij} with effective spins S_i and S_j via the electron spins of a surrounding metallic host material. The Hamiltonian is given by:

$$\mathcal{H}_{i,j}^\mathrm{RKKY} = \Gamma_\mathrm{RKKY} \left(S_i S_j \right) F \left(2 k_\mathrm{F} r_{ij} \right) \tag{3.6}$$

with

$$F(x) = \frac{1}{x^3} \left(\cos x - \frac{\sin x}{x} \right) \ , \tag{3.7}$$

the Kittel-function. k_F the Fermi wave vector and Γ_RKKY describing the strength of the interaction.

The second relevant process is dipole-dipole interaction, which is described by the Hamiltonian:

$$\mathcal{H}_{i,j}^\mathrm{dd} = \Gamma_\mathrm{dd} \frac{S_i \cdot S_j - 3 \left(S_i \cdot \hat{\mathbf{r}_{ij}} \right) \left(S_j \cdot \hat{\mathbf{r}_{ij}} \right)}{\left(2 k_\mathrm{F} r_{ij} \right)^3}. \tag{3.8}$$

The unit vector between the two magnetic moments is given with $\hat{\mathbf{r}_{ij}} = (r_i - r_j)/|r_i - r_j|$. The interaction strength is given with Γ_dd

Both described interaction have an interaction strength $\Gamma \propto 1/T^3$, therefore their relative strength can be described by the parameter $\alpha = \Gamma_\mathrm{RKKY}/\Gamma_\mathrm{dd}$.

While the dipole-dipole interaction is almost identical for silver and gold, the RKKY interaction changes by about a factor of 3. This results in $\alpha = 5$ for Au:Er [Fle03] and $\alpha \approx 12.5$ for Ag:Er [Hen17].

In [Sch00, Fle03] a simulation of the Au:Er sensor is done, including a numerical diagonalization of the complete Hamiltonian. The dipole-dipole and the RKKY interaction are taken into account for up to 10 magnetic moments on a finite cubic lattice with about 100 to 400 atoms. These results were compared to a mean field simulation as well as to measurements. The agreement between the specific heat capacity and the magnetization of Au:Er obtained by simulation and measurements can be seen in figure 3.3. The last expansion of the theory model to describe the thermodynamic properties of Au:Er is the influence of nuclear quadrupole moments present in ^{167}Er and in gold. With a nuclear spin of 7/2 the ^{167}Er in the sensor introduces an additional heat capacity between 30 mK and 100 mK as described in [Fle00, Fle03]. To remove this contribution to detector heat capacity the sensor is made with an erbium sample enriched with ^{168}Er, which contains no nuclear quadrupole moment. This way the the natural abundance of ^{167}Er with 22.9% can be reduced to 1.2% of ^{167}Er in the used sample.

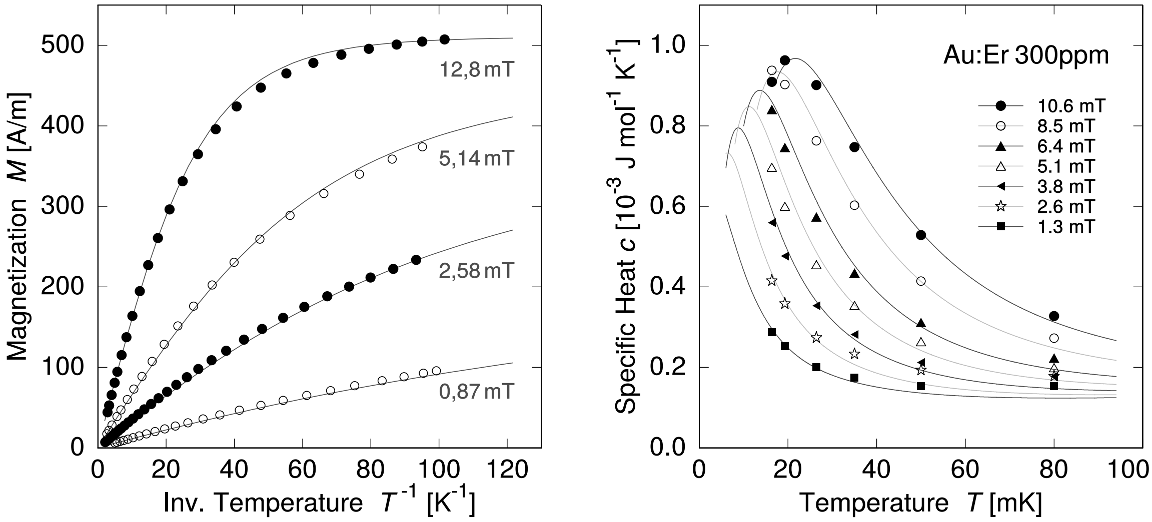

Figure 3.3: **(left)** Inverse temperature dependence of the magnetization $M(T^{-1})$ and **(right)** temperature dependence of the specific heat $c(T)$ of Au:Er for different magnetic fields.

For gold the natural isotope ^{197}Au is used which has a nuclear spin of $I = 3/2$. It has further more a large electric quadrupole moment [Pow74]. In a perfect fcc lattice structure of a ^{197}Au crystal the resulting energy levels are degenerate. Due to the presence of defects, e.g. the $\approx$ 300 ppm of Er^{3+}-ions in the Au:Er sensor a finite crystal field acts on the nuclear spin system and the degeneracy is split up, which leads to an increase of heat capacity at mK temperatures [Her00]. This additional heat capacity was observed in MMC's [Fle98, Ens00].

This effect due to the quadrupole moment of ^{197}Au can be avoided by using silver as metallic host material for erbium. Both natural isotopes ^{107}Ag and ^{109}Ag have a nuclear spin of $I = 1/2$ and therefore do not have a quadrupole moment.

Thanks to measurements performed with MMC's having Ag:Er sensors scaling laws for the thermodynamic properties of Ag:Er could be found, starting from the theory of Au:Er [Hen17]. The important parameter is the ratio between RKKY interaction strength and the dipole-dipole interaction strength α, since this ratio changes from Au to Ag. The specific heat capacity c_{Er} of the erbium ions in silver is given by:

$$c_{\mathrm{Er}}(B,T,x,\alpha) = \frac{\alpha'}{\alpha} \times c_{\mathrm{Er}}\left(B,T,\frac{\alpha}{\alpha'}x,\alpha'\right) \tag{3.9}$$

as well as the magnetization:

$$M(B,T,x,\alpha) = \frac{\alpha'}{\alpha} \times M\left(B,T,\frac{\alpha}{\alpha'}x,\alpha'\right) \tag{3.10}$$

with $\alpha' = 5$ for Au as host material, an erbium concentration x and $\alpha' = 12.5$. These scaling laws allow to predict the thermodynamic properties of fabricated sensors of MMC's with a high accuracy.

3.3 Sensor read-out geometry

The MMCs used for this thesis have a double meander read out geometry. The static magnetic field, which needs to be present at the location of the sensor material to induce the temperature dependent magnetization is created by a superconducting current I running through a meander shaped coil positioned underneath the sensor material. This planar geometry allows for a fabrication of these detectors via photo lithography. A schematic drawing is shown in figure 3.4. The provided B-field is proportional to the persistent current I. The filling factor F is a measure for the B-field strength for a certain current that is seen by the sensor material and is for this geometry $F = 0.5$ at maximum, since roughly half of the magnetic field lines are underneath the meander coil where no sensor is present. This can be dramatically improved by the introduction of a so called sandwich design, where the provided current also runs through a second superconducting layer above the sensor material. A schematic of such a sandwich design can be found in figure 4.1. This way the provided B-field strength is almost completely between the meander coil and the second superconducting layer. Filling factors $F \approx 1$ can be reached [Heu11]. Both types of superconducting coils are used for the detectors presented within this thesis.

The used MMC's have a gradiometric read-out scheme as depicted in figure 3.4. Two pixels, consisting of the meander shaped coil with a sensor and absorber on top, are connected in parallel to a read-out coil, which is close to a SQUID. In addition, the superconducting planar meander shaped coil that provides the current I for the creation of the B-fields works as signal pick-up coil. This connection scheme has the advantage, that the created signals in the two pixels have a different polarity, while read-out with the connected SQUID. This way two pixels can be connected to one read-out channel, which reduces the complexity of the read-out. Furthermore, only temperature differences ΔT occurring in the single pixels are recognized by the read-out. Any substrate temperature change which is present for both pixels will be canceled for perfectly symmetric pixels.

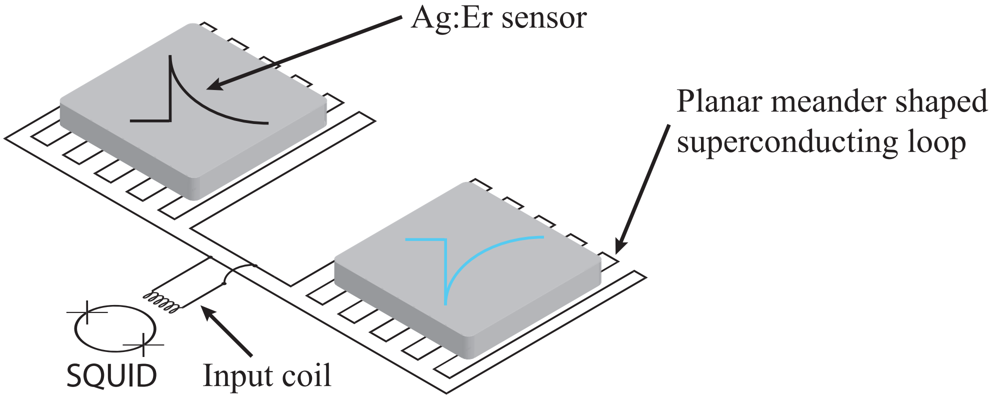

Figure 3.4: Schematic drawing of 2 pixels connected in parallel to an input coil of an SQUID in a gradiometric set up.

The created flux $\Delta\Phi_\mathrm{s}$ in the SQUID is given by:

$$\Delta\Phi_\mathrm{s} = \frac{M_\mathrm{is}}{L_\mathrm{m} + 2\left(L_\mathrm{i} + L_\mathrm{p}\right)} \left(\Delta\Phi_1 - \Delta\Phi_2\right) \tag{3.11}$$

Here the mutual inductance between the SQUID and the input coil is defined with M_is gving the coupling strength. The screening current I splits corresponding to the inductances of the single meander L_m, the SQUID input coil L_i and some parasitic inductance L_p following Kirchhoff's law. L_p is typically dominated by the aluminum bonding wires between the double meander and the SQUID input coil.

$\Delta\Phi_1$ and $\Delta\Phi_2$ are the magnetic fluxes created in the two pixels.

3.4 Signal shape and spectral resolving power

The spectral resolving power of an MMC is defined by the signal to noise ratio (S/N) of the detector system. This ratio can be optimized by many parameters like the operating temperature, the strength of the magnetic field applied to the paramagnetic sensor material and many more. In the following the expected signal height and shape and the corresponding thermodynamical noise are derived which allows to maximize S/N.

3.4.1 Signal

The signal shape and in particular the signal height in terms of change of temperature δT per energy input δE depend on the thermodynamic properties of the detector for given operation conditions like the temperature, the persistent current and many more.

3.4.2 Signal shape

The detector response can be derived by describing the detector as a thermodynamic system, consisting of two sub systems as depicted in figure 3.5 and explained in [Fle05]. As there is the electron system and the spin system of the Er-ions. The phonon system is excluded due to its negligible contribution to the heat capacity at the typical working temperature of MMCs. Systems like the nuclear quadrupole moments of the host material or the implanted ^{163}Ho in the absorber are not considered here as well. The influence on the pulse shape of implanted ^{163}Ho will be discussed in chapter 5.

The electron system includes the electrons of the gold absorber and the Ag:Er sensor with heat capacity C_e. Since sensor and absorber are in strong thermal contact, the electrons are considered to belong to one system. The second system are the Er^{3+}-ions with heat capacity C_{er}, which are located in the sensor material. In principle also the phononic system with heat capacity C_{ph} is present. But for the typical working temperatures of the MMC's the phononic contribution to the heat capacity of the system is negligible.

The C_{er} system couples to the C_e system via the thermal conductivity $G_{er/e}$. The C_e system couples to a thermal bath with temperature T_0 via a weak thermal link with $G_{e/b}$. The resulting system can be described by two coupled differential equations, one for each system. The solution for an instant energy input $E\delta(t)$ into the C_e-

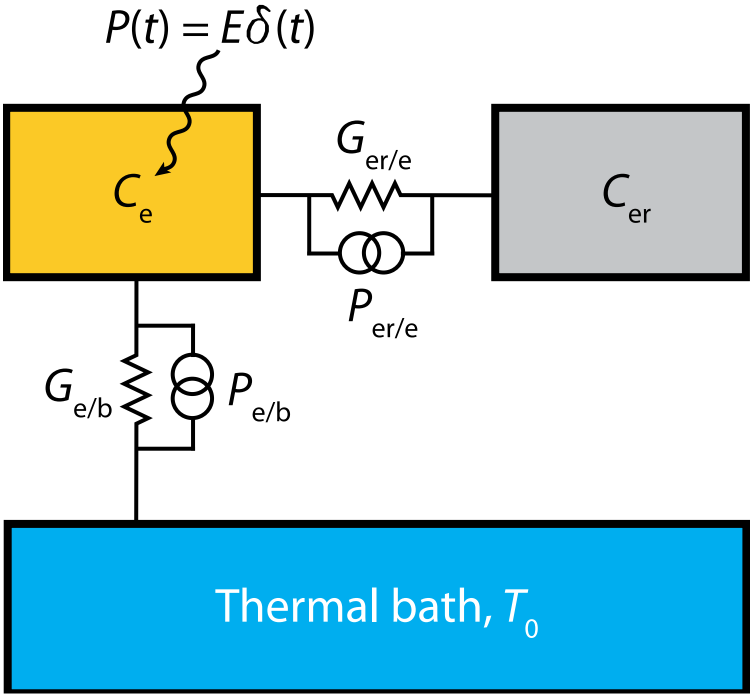

Figure 3.5: Schematic drawing of the relevant thermodynamic sub systems in an MMC.

system is given with:

$$\Delta T_{\mathrm{er}} = T_{\mathrm{er}} - T_0 = \frac{E}{C_{\mathrm{e}} + C_{\mathrm{er}}}\left(-\mathrm{e}^{-t/\tau_0} + \mathrm{e}^{-t/\tau_1}\right) =: \frac{E}{C_{\mathrm{er}}} p(t) \tag{3.12}$$

ΔT_{er} is here the relevant change of temperature since the change of temperature in the erbium system induces spin flips and therefore a change of magnetization. The expected signal shape is a fast exponential rise with the typical time constant τ_0 until the sub-systems are in equilibrium, followed by an exponential decay with a time constant τ_1. In principle these time constants are complex and dependent on the heat capacities and the thermal conductivities of the detector system as depicted in [Fle05]. However, for a weak thermal link to the bath $G_{e/b} << G_{er/e}$ and $C_e \approx C_{er}$ we get the decay time $\tau_1 = C_{tot}/G_{e/b}$ with $C_{tot} = C_e + C_{er}$.

For $C_e \approx C_{er}$ the expected energy resolution is maximized as will be explained in 3.4.3. The rise time τ_0 depends on the coupling strength between the electrons and the spin system of the erbium ions given by the Korringa relation. With this coupling a typical time constant $\tau_K \propto T^{-1}$ is associated.

$$\tau_0 = (1 - \beta)\tau_K \tag{3.13}$$

The fraction of the total heat capacity located in the spin system is given with $\beta := C_{er}/(C_{er} + C_e)$.

3.4.3 Noise

Here the relevant noise contributions are discussed which influence the detectors performance. This includes not only noise sources present in the detector itself but also noise contributions coming from the SQUID read out, which are the dominant contributions for the measurements presented in this thesis.

Thermal noise

A fundamental noise contribution are thermodynamic energy fluctuations between the different sub-systems of the detector. These fluctuations can be described by a spectral power density $S_p = 4k_\mathrm{B}T^2G$ which is frequency independent and is proportional to the corresponding thermal conductivity G among the sub-systems. Following again the thermodynamic model presented in figure 3.5 and by introducing the corresponding noise sources $P_{e/b}$ and $P_{er/r}$ two coupled differential equations can describe the system. The resulting spectral power density in the Fourier space solved for the energy fluctuations is given by:

$$S_{\mathrm{E_{er},td}}\left(f\right) = k_\mathrm{B}C_\mathrm{er}T^2\left(\left(1-\beta\right)\frac{4\tau_0}{1+\left(2\pi\tau_0 f\right)^2}+\beta\frac{4\tau_1}{1+\left(2\pi\tau_1 f\right)^2}\right) \tag{3.14}$$

with the approximations $C_\mathrm{e} \approx C_\mathrm{er}$ and $\tau_0 \ll \tau_1$ [Fle05]. For typical detector parameters this converts to a flux noise of $S_{\Phi,\mathrm{td}} \approx 2 \times 10^4\,(\mathrm{\mu}\Phi_0)^2/\mathrm{Hz}$ in the superconducting pick-up coil, while the actual flux change for a 10 keV photon in such a detector would be $10\,\mathrm{m}\Phi_0$.

Magnetic Johnson noise

Random electron movements in a metal due to the finite temperature of the detector can cause magnetic Johnson noise if they move close to the superconducting pick-up coil. The Brownian motion creates small changing magnetic fields according to Maxwell's equations. The most crucial components are the sensor, the absorber and the used copper support structure for the detector. The small changes in magnetic field can couple into the pick-up coil or directly into the SQUID. The spectral power density for MMC's

$$S_{\Phi,\mathrm{J}}\left(f\right) = \frac{2.376}{4\pi}\mu_0^2 k_\mathrm{B}T\sigma A p\left(\mathrm{e}^{-2\pi d/p} - \mathrm{e}^{-2\pi(d+h)/p}\right) \tag{3.15}$$

was derived in [Pie08, Pie12] based on [Har68, Ens00]. Assumed was a metallic cube at temperature T with an electrical conductivity σ and an edge length h. The cube has a distance d to the squared meander shaped pick-up coil with a stripe to stripe distance p and an overlap area A. For a typical absorber this results in a noise density of $S_{\Phi,\mathrm{J}}(f) \approx 0.7\,(\mu\Phi_0)^2/\mathrm{Hz}$, which is in first order frequency independent. A cut-off frequency can be observed for here irrelevant frequencies above 100 MHz caused by the skin-effect which reduces the effective volume of the absorber.

Er noise

The Er^{3+}-ions present in the paramagnetic sensor alloy are a noise source themselves [Dan05]. They show a relevant contribution towards the low frequency domain with $S_{\Phi,Er} \propto f^{-\zeta}$ where ζ is geometry and fabrication dependent parameter which varies between 0.8 and 1. This contribution is proportional to the number of erbium atoms in the sensor material and is not temperature dependent between 30 mK and 2 K [Fle05]. A possible explanation for this almost $1/f$-noise behavior could be a finite and broadly distributed response time of the orientation of interacting clusters of magnetic moments which was measured via the imaginary part of the susceptibility of Au:Er [Hof12, Wiß13]. Empirically is the power density given by:

$$S_{\Phi,\mathrm{Er}} = \frac{\mu_0^2 \left\langle G^2 \right\rangle}{p^2} S_{\mathrm{m}}(f) N_{\mathrm{Er}}. \tag{3.16}$$

The magnetic constant is μ_0, the distance between two meander stripes is p, the number of erbium atom is N_{Er} and G is a geometry factor describing the magnetic field distribution of the field created by the provided current in the meander shaped coil in the sensor material. And $S_{\mathrm{m}}(f) \approx 0.12\,\mu_{\mathrm{B}}^2 \times (f/\mathrm{Hz})^{-\zeta}$ describing the fluctuations of the magnetic moment of a single erbium ion. For typical detector parameters a noise of $S_{\Phi,\mathrm{Er}}(1\,\mathrm{Hz}) \approx 5 \times 10^4\,(\mu\Phi_0)^2/\mathrm{Hz}$ is expected.

Read out noise

MMCs are read out using a 2-stage SQUID set up described in chapter 4.4. The noise contribution from the SQUID read out is the dominant one for the here presented measurements. It is the only relevant one from the read out chain, since the SQUID read out also acts as a low temperature amplifier. All other noise contributions coming from the read out chain can therefore be neglected. This read out noise has a frequency independent white noise part with a typical level of $S_{\Phi,\mathrm{SQUID-white}} \approx 1\,(\mu\Phi_0)^2/\mathrm{Hz}$ with a cut of frequency defined by the read out electronics. A typical cut off frequency is about 10 MHz. Furthermore, SQUIDs have a $1/f$ contribution which becomes dominant at about 1 kHz.

Fundamental limit of the energy resolution

If all noise contributions which might be optimized or avoided are neglected and only the fundamental thermal fluctuation of energy within the detector system for a given temperature is assumed a fundamental detector energy resolution can be calculated. This calculation is assuming so to speak a perfect read out chain, where all other noise contributions are negligible small compared to the thermal fluctuations and the corresponding noise.

The detector response is Gaussian and the broadening of this Gaussian at full width half maximum is given with:

$$\Delta E_{\mathrm{FWHM}} = 2\sqrt{2\ln 2}\left(\int\limits_0^\infty \mathit{SNR}^2(f)\,\mathrm{d}f\right)^{-1/2} \tag{3.17}$$

Here $SNR^2(f)$ is the squared frequency dependent signal-to-noise ratio. It is defined by

$$\mathit{SNR}^2(f) = \frac{|\tilde{p}(f)|^2}{S_{\mathrm{E_{er}},\mathrm{td}}(f)} \tag{3.18}$$

where $\tilde{p}(f)$ is the Fourier transform of the expected signal with the in chapter 3.4.2 calculated rise and decay time and $S_{\mathrm{E_{er}},\mathrm{td}}(f)$ is the density of the thermodynamic noise.

As shown in [Fle03] this can be approximated to

$$\Delta E_{\mathrm{FWHM}} \approx 2\sqrt{2\ln 2}\sqrt{4k_{\mathrm{B}}T^2C_{\mathrm{e}}}\left(\frac{1}{\beta(1-\beta)}\frac{\tau_0}{\tau_1}\right)^{1/4} \tag{3.19}$$

with $\beta = C_{\mathrm{er}}/(C_{\mathrm{er}} + C_{\mathrm{e}}) \approx 1/2$ and $\tau_0 \ll \tau_1$. For this calculation the signal shape discussed in 3.4.2, the spectral power density of the thermodynamic systems, the operating temperature and the heat capacities of sensor and absorber are considered. The best energy resolution can be reached for $\beta = 1/2$, which is true for matching heat capacities of absorber and sensor.

3.5 Thermodynamic properties of ^{163}Ho in Au

The exact amount of implanted ^{163}Ho per detector pixel is always a trade off between several parameters like fraction of unresolved pile up events, number of needed detectors and the total measurement time of the experiment. The energy resolution

ΔE_{FWHM} is another parameter that needs to be considered since it is fundamentally limited by the total heat capacity of the detector as described in section 3.4.3 and the implanted ^{163}Ho could lead to a non-negligible contribution to the heat capacity of the detector. In the following a theoretical description for the expected specific heat of implanted ^{163}Ho atoms in gold is given. In fact the ^{163}Ho -ions have $J = 8$, $L = 6$ and $S = 2$ and therefore a contribution to the heat capacity similar to the Au:Er can be expected. For these theories always the diluted case with Ho^{3+}-ions surrounded by gold atoms is considered as proposed by simulations of the implantation process [Gam17]. Since the Au:Ho is quite similar to the system of Au:Er basically the same mechanisms for the heat capacity can be considered, although the corresponding coupling strength might be different ones.

3.5.1 Properties of Ho^{3+}-ions

In the diluted alloy a ^{163}Ho -ion substitutes an Au-ion in the fcc crystal lattice structure very similiar to the case of Au:Er (see picture 3.2) and loses three electrons to the de-localized electron system of the surrounding Au atoms. So the Ho^{3+}-ion is left in an [Kr]$4d^{10}4f^{10}5s^25p^6$ electron configuration with a spatial extent of about $R = 1\,\text{Å}$. The electrons of the unfilled $4f$-shell cause a paramagnetic behavior of the alloy since they carry a permanent magnetic moment. This is shielded quite well from the outer Au crystal field lattice by the electrons of the outer shells since the $4f$-orbital is located quite deep in the Ho-ion, $R = 0.3\,\text{Å}$. So interactions with the crystal field can be neglected while calculating the spin-orbit coupling of the Ho^{3+}-ions using Hund's rules. The angular momenta L,S and J are determined this way. And with the Landé factor g_J

$$g_J = 1 + \frac{J(J+1) + S(S+1) - L(L+1)}{2J(J+1)} \tag{3.20}$$

follows for the magnetic moment μ_J

$$\mu_J = g_J \mu_B J \tag{3.21}$$

with the Bohr magneton $\mu_B = 9.274 \times 10^{-24}$ J/T. For Ho^{3+}-ions $\mu_J = 10.6\,\mu_B$ with $J = 8$, $L = 6$, $S = 2$ and $g_j = 4/3$.

In the case of just isolated Ho^{3+} magnetic moments the ground state is 17-fold degenerated due to the magnetic quantum number m_J ranging from $-J$ to J. The exited states of the magnetic moments caused by spin-orbit coupling are on an energy scale of several thousand Kelvin. Therefore, the Ho^{3+}-ions can be considered as a single-level system for temperatures well below room temperature, since the occupation probability of an excited state is negligible small [Sch00] at least for the absence of any external fields which might brake the degeneracy of the ground state. Such fields as for example an external magnetic field, the crystal field of the surrounding host material and the hyperfine interaction of the electrons with the nucleus of the ^{163}Ho are of course present and add energy levels to the system. The effect of the fields is small and can therefore be treated as perturbation to the ground state. In the following several possible perturbations of the ground state are discussed and the influence on the energy level splitting and the corresponding additional heat capacity is estimated.

3.5.2 Zeeman effect

As external magnetic fields the earth magnetic field and the magnetic field created by the persistent current running in the meander under the absorber can be considered. These fields **B** brake the spatial symmetry and the corresponding energy splitting can be described by the Zeeman effect with the Hamiltonian H_Z given as:

$$H_Z = g_J \mu_B \mathbf{B} \cdot \mathbf{J} \tag{3.22}$$

The related energy eigenvalues E_Z are given with:

$$E_Z = g_J \mu_B |\mathbf{B}| m_J \tag{3.23}$$

Here $\mathbf{B} \parallel J_Z$ is considered. The estimated strength of the earth magnetic field is about 60 μT. The resulting energy splitting is in range of 50μK. Therefore is the additional heat capacity negligibly small. The magnetic field created by the persistent current in the meander is even smaller for the typical detector geometry. The ^{163}Ho is implanted in a distance of about 9 μm from the B-field generating meander coil. The field strength at that distance is below 1 μT. So no significant contribution to the heat capacity of Ho^{3+}-ions can be expected from the Zeeman effect.

3.5.3 Crystal field

The Au-ions surrounding the Ho^{3+}-ions create an electrostatic field which does not brake the spin-orbit coupling of the electrons in the $4f$-shell, since this shell is located deep in the holmium atom and is shielded by the surrounding electrons. As explained in section 3.5.1 the spin-orbit splitting is several thousand Kelvin and therefore the Ho^{3+}-ions can be considered to be in the degenerate ground state. But this ground state is effected by the crystal field created by the surrounding host material. The theoretical expectation of the splitting is in the region of about 10 K to 100 K and therefore needs to be considered.

In the theoretical model the crystal field is described by one electrostatic potential which contains all the electric fields of the single ions. Since the ^{163}Ho is implanted in gold the potential has the symmetry of an fcc-lattice and can be described by crystal field functions of fourth and sixth order.

This is done by transforming this field functions into quantum mechanical operators with an equivalent symmetry [Ste52]. The resulting Hamiltonian [Lea62] is still dependent on the parameters W and $x \in [-1, 1]$ which need experimental input due to the very complicated nature of the ionic wave functions. They basically define the scale of the energy splitting. For these parameters theoretical [Ble89] and experimental [Mur70] constraints exist. These parameters were calculated by the two groups for Holmium in Gold. They determined the conflicting values for W and x with $W = -0.112$, $x = -0.357$ [Mur70] and $W = -0.113$, $x = -0.576$ [Ble89]. Dependent on the parameter set one could expect a significant contribution to the heat capacity of the system due to the crystal field for temperatures around 20 mK.

3.5.4 Hyperfine interaction

The interaction of the nuclear magnetic moment with the magnetic moment of the electrons is the hyperfine interaction. The nucleus of ^{163}Ho has a nuclear spin of $I = 7/2$ and a resulting magnetic dipole moment $\mu_I = g_I \mu_N I$. Where $g_I = 1.2$ is the nuclear $g-$factor and $\mu_N I = 5.051 \times 10^{-27}\,\mathrm{J/T}$ is the nuclear magneton. The Hamiltonian H_{HF} for this interaction is then given by:

$$H_{HF} = A \cdot hI \cdot J \tag{3.24}$$

Planck's constant is h, A is the material dependent hyperfine coupling constant and I are the nuclear spin operators. The expected energy scale for the hyperfine interaction is of the order of 100 mK and needs therefore to be considered. In literature values for the hyperfine coupling constant A for Ho^{3+}-ions with $A = 812$ MHz [Abr70a] can be found. However these were determined for different host materials then gold. Therefore, a different crystal field might have been present. The effect of the crystal field on the magnetic hyperfine interaction should be negligibly small but a change of A might occur. Depending on A a specific heat capacity c_{ion} between $0\,k_\mathrm{B}$ and $1\,k_\mathrm{B}$ per ion in the relevant temperature range below 100 mK can be expected.

3.5.5 Magnetic moment interaction

Up to this point the Ho^{3+}-ions are considered to have no mutual interaction. Simulations have shown [Gam17] that the expected concentration for the implantation process used for ECHo is in the region of a few percents. Therefore, also the mutual interactions between the Ho^{3+}-ions should be considered which induce an additional contribution to the specific heat per Ho-ion. In principle both following interactions are dependent on the total angular moment J, which will be used to describe the interactions. Note that this description can be adapted to be described by the effective spin S like in chapter 3.2.2. This is because of the isotropy of the Γ_7 ground state doublet.

One interaction is the magnetic dipole-dipole interaction between the magnetic moments μ_i and μ_j at the positions r_i and r_j Here is $\mu_j = g_J \mu_B J$ was used. The Hamiltonian is given by:

$$H_{ij}^{dipole} = \frac{\mu_0}{4\pi}(g_J \mu_B)\frac{1}{r_{ij}^3}[J_i \cdot J_j - 3(J_i \cdot r_{ij})(J_j \cdot r_{ij})] \tag{3.25}$$

The distance between the magnetic moments is given by r_{ij}. The interaction itself is anisotropic and decreases with $1/r_{ij}^3$.

Another indirect mutual interaction is the RKKY[1] interaction. Here the localized $4f$-electrons of the single Ho^{3+}-ions interact mutual via the de-localized electron system of the conduction band. The Hamiltonian is given by:

$$H_{ij}^{RKKY} = \Im^2 \frac{g_J^2(g_J - 1)^2}{g_J} \frac{4V_p m_e^* k_F^4}{\hbar(2\pi)^3}(J_i \cdot J_j)F(k_F r_{ij}) \tag{3.26}$$

The effective mass of the free electrons is m_e^*, V_p is the volume of the primitive unit cell and $k_F = 1.2 \times 10^{10}\, m^{-1}$ is the Fermi wave vector of the gold conduction electrons. The Kittel function $F(\rho)$

$$F(\rho) = \rho^{-3}(cos\, \rho - \frac{1}{\rho} sin\, \rho) \tag{3.27}$$

and the parameter $\Im$ describe the strength of the exchange interaction between 4f-electrons and the conduction band. Also here decreases the interaction with $1/r_{ij}^3$. Due to the large similarities to the case of Au:Er no large contributions from the RKKY interaction and dipole-dipole interaction are expected.

With this expectations for the heat capacity of ^{163}Ho in gold in mind a change of the signal shape and of the detector performance is expecetd due to the implanted ^{163}Ho . The results will be discussed in chapter 5, where the influence of implanted ^{163}Ho in a gold absorber of an MMC is studied.

---

[1] Ruderman-Kittel-Kasuya-Yosida

4. ECHo detector preparation and SQUID read out

In this chapter the two used detector chips will be presented, as well as the preparation for the implantation, the designed circuit board and copper support structure for the detector chip and the basic principle of the SQUID read out.

4.1 maXs-20 sandwich detector

The maXs-20 design [Heu11] is designed for x-rays up to 20 keV and a very good spectral resolving power. In fact these detectors showed the best energy resolution ever achieved with MMCs $\Delta E_{\mathrm{FWHM}} = 1.6\,\mathrm{eV}$ and a fast signal rise time $\tau_r = 90\,\mathrm{ns}$ [Kem18]. The detector chips consist of an 1D-array with 16 pixels corresponding to 8 read out channels. The detector geometry is based on the "sandwich" design with a spiral shaped pick-up coil and a superconducting layer above the sensor material described in chapter 3.3. A schematic drawing can be seen in picture 4.1. It consists of a detector array with 16 pixels aligned in a row. Due to the typical gradiometric design of these detectors two pixels are read out by one read out chain using the signals polarity to distinguish. Due to the spiral detection coil with superconducting cap a filling factor close to $F \approx 1$ can be reached for the magnetic field for the sensor, which increases the detectors performance. As depicted in the schematic drawing, for this detector stems have been implemented. These are gold structures between the absorber and the sensor, which reduce the athermal phonon loss [Fle09]. Shortly after the deposition of energy in the absorber a small fraction of energy creates athermal phonons. Due to the large wavelength of athermal phonons, they can pass with a certain probability through the sensor directly into the substrate and deposit their small fraction of energy there. A small fraction of energy is therefore lost for some of the measured signals. The resulting signals have a smaller amplitude, which leads to low energy tails of measured spectral lines. This can be avoided by the stems, which reduce the probability for a athermal phonon to travel directly to the substrate dramatically, due to the reduced contact area between absorber and sensor. The signal rise time can be kept at the intrinsic rise time corresponding to the Korringa constant. The detector chips have been fabricated with photo lithographic micro structuring in the clean room of the Kirchhoff-Institute for Physics, Heidelberg University.

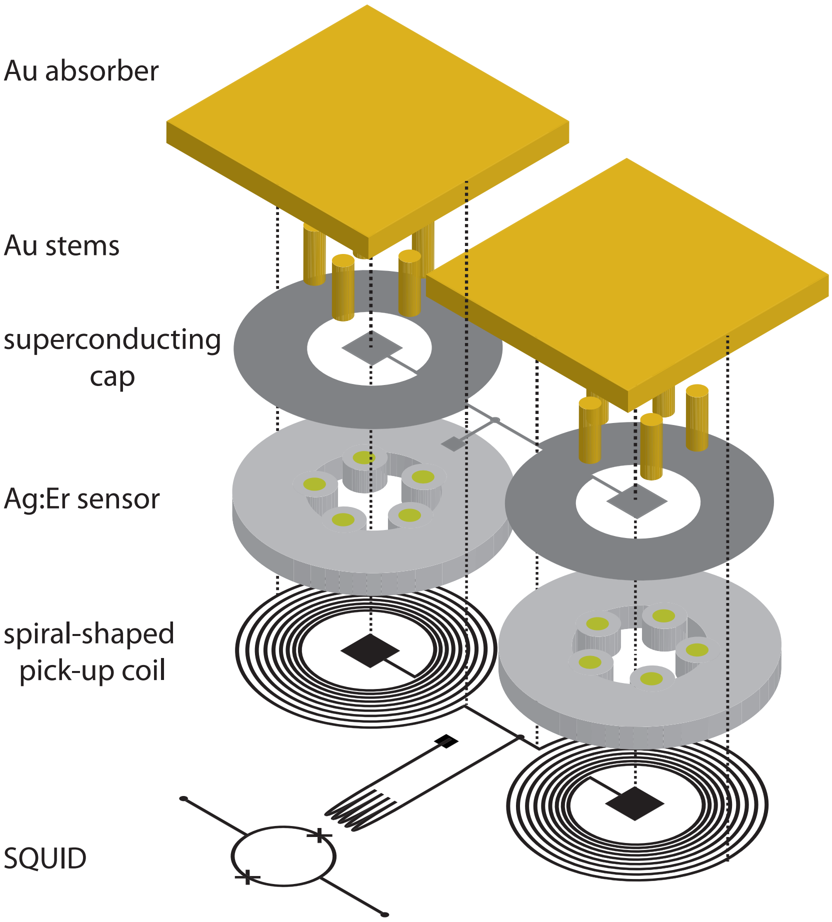

Figure 4.1: Schematic drawing of the maXs 20 detector design, based on the MMC principle.

4.1.1 maXs-20 with enclosed ^{163}Ho

For the used detector chip all pixels have been implanted with ^{163}Ho . The implantation process was performed at ISOLDE-CERN in an off line process. For this a ^{163}Ho target was prepared via neutron irradiation of an enriched ^{162}Er target at the research reactor Institute Laue-Langevin in Grenoble, which decays to ^{163}Ho . During this neutron irradiation not only ^{163}Ho is produced but also other isotopes of holmium and lighter and heavier elements. To reduce the production of unwanted radio nuclide's the ^{162}Er target gets purified before the irradiation. Afterwards a second chemical purification by a nuclear chemistry group in Mainz [Dor18] via column chromatography is done. This way a purified holmium sample is produced. A γ analysis of the purified sample showed that no radioactive nuclide's where present besides ^{166m}Ho, which could not be chemically separated. The fraction of ^{166m}Ho to ^{163}Ho was determined with 10^{-4}. This unwanted isotope of holmium could be further reduced via a mass selection process of ^{163}Ho in the ion beam implantation facility ISOLDE at CERN [Nil03]. There the chemically purified sample was ionized and implanted into the detector via a selective ion beam. The planned activity was about 1 Bq per implanted pixel.

4.2 ECHo-1k detector

The second used detector design is called ECHo-1k. The design and fabrication steps are discussed in [Weg18]. The detector chip has 72 pixels in 4 rows, which can be read out by 36 read out channels. These pixels follow the classical double meander MMC design. Figure 4.2 **(left)** shows a drwanig of the ECHo-1k design, while figure 4.2 **(right)** shows a photo of a fully micro fabricated ECHo-1k detector chip. As can be seen in picture 4.2 2 readout channels at the top left and the bottom right of the chip are temperature detectors. They have a double emander in which only one side

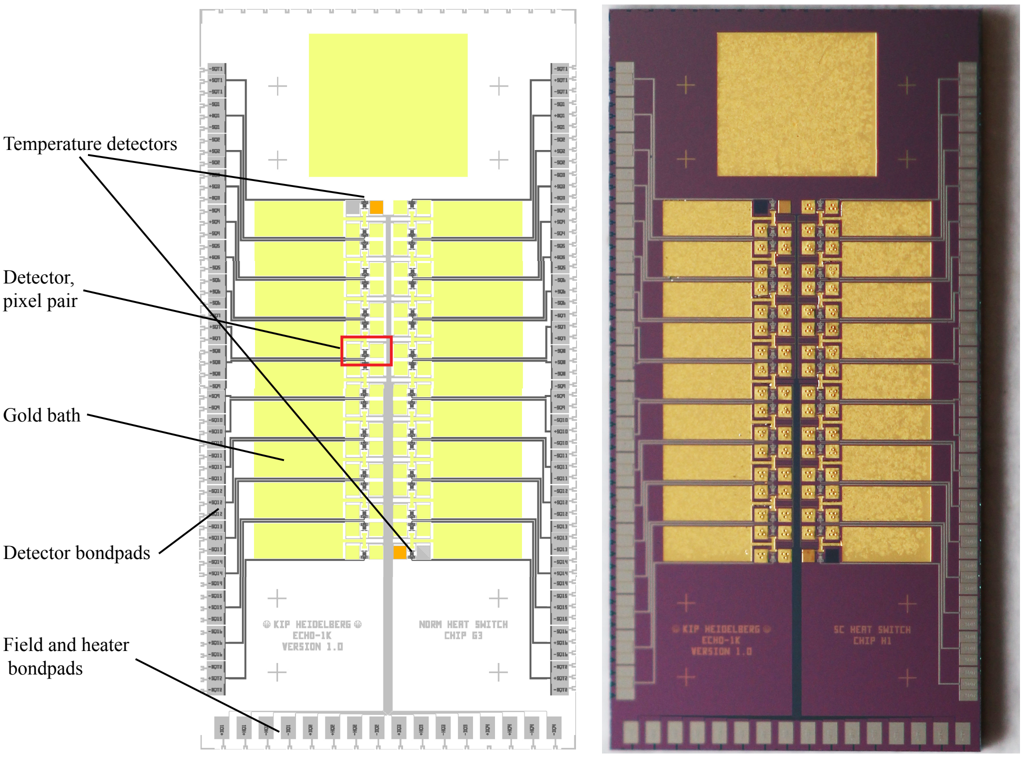

Figure 4.2: ECHo-1k detector design.**(left)** Schematic design of the chip. **(right)** Real picture of a micro fabricated ECHo-1k detector chip.

is equipped with a sensor. Because of that temperature changes of the full detector chip induce a change of magnetization in this sensor. Therefore, by monitoring the output signal of this channel a direct information on the present temperature on the chip can be extracted.

The bigger golden areas next to the pixel rows are the thermal baths, with a way higher heat capacity then the detector ones. They are connected via small gold paths (weak thermal links) with the single pixels. To reach a better thermalization of the whole detector set up, small gold wires are bonded between the gold baths always to the next neighbors. The big quadratic gold area in the middle top of the chip is ten connected to the next small Au bath and to the copper support structure.

The single pixel has dimensions of $180\,\mu\text{m} \times 180\,\mu\text{m} \times 5\,\mu\text{m}$. It is connected via 3 stems with the underlying sensor which is with $175\,\mu\text{m} \times 175\,\mu\text{m} \times 1.3\,\mu\text{m}$ slightly smaller. One detector pixel has a heat capacity of about 3 pJ/K at 20 mK. For each pixel pair superconducting niobium lines connect the pixels with the bondpads for the SQUID read out at the left and right edge of the chip. On the bottom of the chip the field and heater lines are placed. They are used to provide the persistent current in the meanders. The chip is split in 4 independent quadrants, which have their own field and heater lines. One field and heater line pair is used to provide the persistent current in all pixels of one quadrant.

The design allows for a parallel read out with 36 read out SQUID's of all the detector channels, like it is performed for this thesis, it furthermore allows to connect all needed components for a microwave SQUID multiplexed read out, which will allow, in future phases of ECHo, detector channel numbers up to 1000 per read out wiring.

A simulation of the detectors energy resolution was performed, based on the descriptions in chapter 3. By considering the input parameters like the Er concentration in the sensor material, the persistent current in the meander, the sensor height and the actual noise density at the operating temperature of about 10 mK this simulation leads to an expected energy resolution of $\Delta E_{\text{FWHM}} \approx 3\,\text{eV}$.

The position of the pixels in long lines with a very small distance from each other allow for a smooth implantation process. At RISIKO in Mainz [Kie19] the mass separator has a beam size of roughly 0.7 mm in diameter. This way the implantation area on the chip can be scanned by the ion beam in rows. Furthermore, the space between the implantation areas is kept small to achieve a high implantation efficiency.

4.3 Implantation of ^{163}Ho

The planned activity for the implantation process was 2 Bq per pixel. For the implantation itself, the chip was prepared in a way that only 57 pixels are implanted. Left out are the temperature detectors, the two pixels to the left or right of the temperature detectors and 7 more pixels called background (BG) pixels. The BG pixels always have their partner pixel belonging to one read out channel implanted with ^{163}Ho . This way in situ background measurements and the presented measurement in chapter 5 of the additional heat capacity due to ^{163}Ho could be performed.

Both detector chips use gold absorbers. The preparation of these absorbers with ^{163}Ho on a single chip basis is a non-standard technique and was developed within this thesis. The absorber consists of two gold layers with ^{163}Ho in between. The thickness of this layers is in both cases $5\,\mu$m below and above the ^{163}Ho . With this implantation geometry a 4π-encapsulation of gold surrounding the ^{163}Ho is reached.

The detectors are fabricated to the first $5\ \mu$m of gold with well-established clean room techniques [Weg18]. In this shape the detector is fully functional and could be used for e.g. x-ray measurements. After this the detectors are tested and the once showing a good performance are ready for the implantation preparation. In the following the necessary preparations for the implantation are described. The chips are glued with photo resist on a glass plate which allows for safe handling of the chips in the clean room for the further processes. Here two aspects are important. First, the processed chip needs to be surrounded by a structure with the same height as the detector chip with no significant gap between the detector chip and the surrounding structure as can be seen in figure 4.3 **(right)**. This ensures a proper photo resist distribution on the detector chip during the following micro structuring processes. The detectors are spin coated with about 3000 rpm with photo resist and due to the surface tension of the photo resist at the edges of the substrates side walls build up. To avoid these walls at the detector chip, the surrounding chips are needed. The walls effect the precision of the following photolitographic processes.

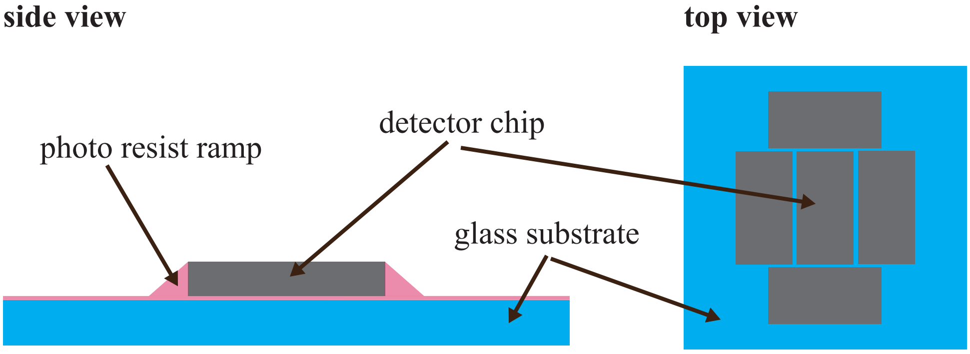

Figure 4.3: Implantation preparation of the detector chip. **(left)** Side view of the chip with photo resist ramp. **(right)** Top view of the chip with surrounding substrates of same height.

The photo resist is processed with a maskless aligner. The laser is abbreviated by a non flat photo resist surface. The other important detail are the photo resist ramps from the glass substrate to the detector chip, which can be seen in figure 4.3 **(left)**. They ensure a closed layer for all further sputtered metal layers. Which will become important for the implantation process itself, explained later.

Once the detector chip is prepared like this the actual structuring process can start as depicted in figure 4.4. In 4.4 **(1.)** a photo resist with a height of about 8 μm is used, which matches the height of the absorbers above the detetcor substrate. This way the structured squares of 150 μm × 150 μm on the 180 μm × 180 μm absorber area of the ECHo-1k detector chip are well-defined. The 15 μm to each border of the absorber area ensure a 5 μm encapsulation of the implanted ^{163}Ho in all directions. After these squares are structured 4.4 **(2.)** another 100 nm Au layer is sputtered on the whole set up. This way the implantation area where the charge accumulates during the ion implantation is electrically connected to the big surrounding gold surface and the charge can be removed by a clamp to ground on the glass substrate during the implantation process. To ensure the contact between the sputtered Au on the glass substrate and the gold on the absorbers the photo resist ramps described above are necessary. As **(3.)** step the actual ^{163}Ho implantation process takes place. Right after the implantation process 4.4 **(4.)** another 100 nm of gold are sputtered to protect the implanted ^{163}Ho before the further processing. In the next step the photo resist is removed and only the 150 μm × 150 μm ^{163}Ho and Au layer on the absorber remains. Then a final photo resist layer is structured similar to the one in step **(1.)**. Therefore, the detector chips need to be glued again on the glass substrate, before a 165 μm × 165 μm square is structured on the absorbers 4.4 **(5.)**. In these squares another 5 μm of gold are sputtered 4.4 **(6.)**. As already mentioned the different square sizes ensure a 5 μm thick gold layer in every direction

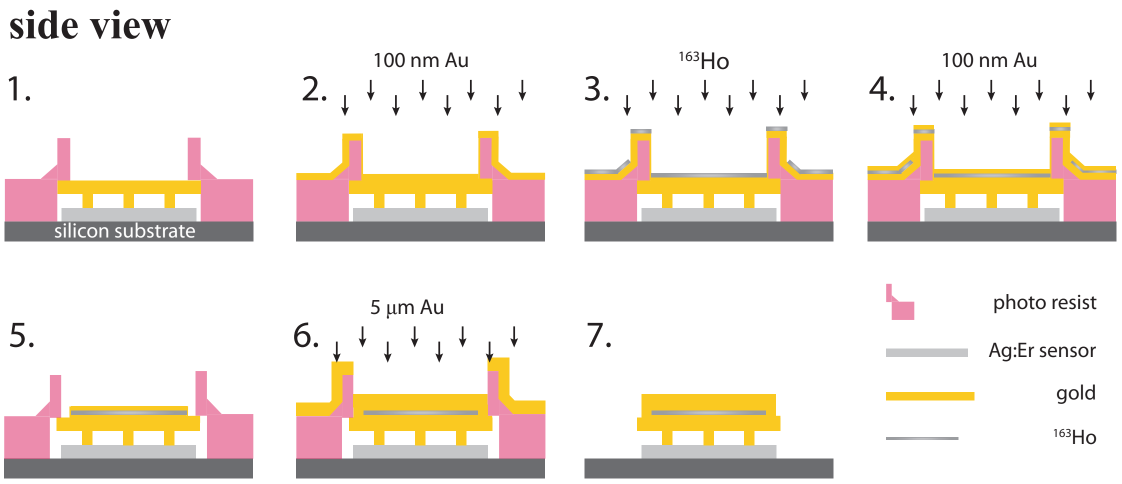

Figure 4.4: Implantation processes for a single chip.

around the ^{163}Ho 4.4 **(7.)**. This way a quantum efficiency close to 100% is reached. Furthermore, the chosen dimension guarantee safety margins which also ensure a complete encapsulation if the squares are slightly miss-aligned. This procedure was used for both detector designs with only slight changes.

With this geometry only every 10^{-9} ^{163}Ho decay suffers from an energy loss. This number is based on simulations performed by F. Mantegazzini [Vel19a]. Here the integrated survival probability of 10^7 photons with an energy between 1.8 keV and 3 keV with a distribution following the ^{163}Ho spectral shape is calculated with 10^{-5}. For this energy range the biggest photon loss is expected. And with a branching ratio of about 10^{-4} for photons per decay this number can be given. The thickness around the ^{163}Ho is a optimization parameter. With a reduced thickness lower heat capacities can be reached and therefore the detectors performance can be improved. The desired implantation activity is about 10 Bq per pixel. Simulations by L. Gamer [Gam17] have shown that with an ion implantation as it is performed by RISIKO in Mainz at the moment only activities of about 3 Bq can be reached. This is caused by the fact, that at a certain point every implanted ^{163}Ho -ion sputters away an already implanted ^{163}Ho -ion. This limit might be overcome by an implantation of ^{163}Ho together with pulsed laser deposited gold. A typical implantation depth for the here used implantation parameters is about 5 nm.

4.4 Low temperature read out

The typical read out scheme used for MMCs consists of a 2-stage SQUID read out [Dru07]. SQUIDs are very sensitive current sensors that allow to detect the change of a magnetic flux $\Delta\Phi$ created by a current I_s in the input coil of the SQUID. The working principle is based on the Josephson effect [Jos62] and a detailed description can be found in [Cla04]. In the following just a brief overview over the used set up will be given. It consists of 2 stages. The first stage is a dc-SQUID, called front-end SQUID, since it is directly connected to the detector chip. The second stage is a series of N dc-SQUIDS working as low temperature, low noise voltage amplifier.

4.4.1 Working principle of a dc-SQUID

A superconducting loop with two Josephson junctions make up a dc-SQUID. A schematic drawing can be seen in picture 4.5 **(left)**. The Josephson junctions are non superconducting contacts which interrupt the superconducting loop and allow flux to enter and leave the loop. They have a typical thickness of a few nm. A hysteretic behavior of the SQUID is avoided by shunt resistors parallel to each of the two junctions. For small bias currents I_b applied to the dc-SQUID Cooper pairs can

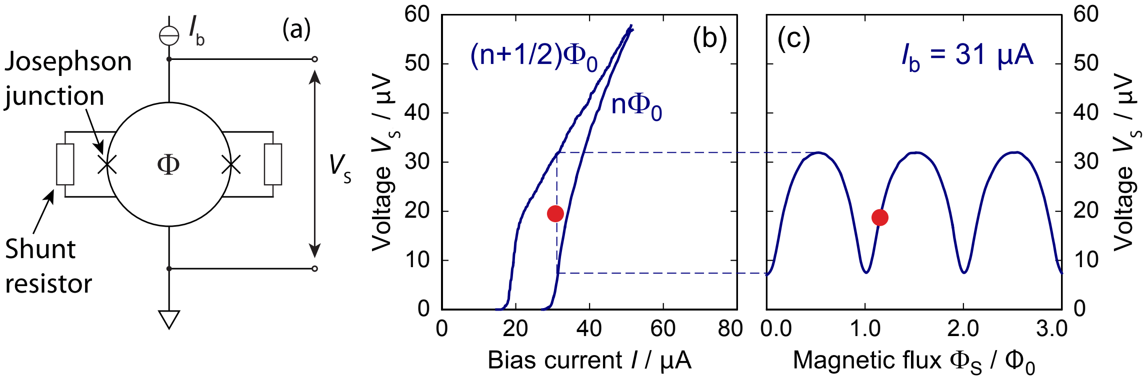

Figure 4.5: (left) Schematic of dc-SQUID. The red dot marks a possible working point. **(mid)** Voltage drop V_s across a dc-SQUID versus the applied bias current I_b of the dc-SQUID.**(right)** Voltage drop V_s across a dc-SQUID versus the change of magnetic flux Φ_s for a fixed bias current.

tunnel through the thin barriers without any voltage drop. If the current exceeds a critical current I_c a finite voltage drop can be measured. This critical current I_c is dependent on the present magnetic flux Φ in the superconducting loop and shows a periodic behavior for multiples of the magnetic flux quantum $\Phi_0 = h/2e \approx 2.07 \times 10^{-15}$ Wb. For $I_b > I_c$ the current can no longer be carried only by Cooper pairs but by quasi particles as well, both tunneling through the barrier. In picture 4.5 **(mid)** the corresponding voltage drop V_s across the SQUID is shown dependent on the bias current I_b for multiples of Φ_0 and $(n + 1/2) \times \Phi_0$. As depicted in figure 4.5 **(right)** this property leads to periodic change of voltage for change of flux. This highly non-linear behavior needs to be linearized by a feedback loop so called flux locked loop mechanism, which will be explained later.

4.4.2 Two-stage setup and linearization of the SQUID signal

One important parameter for all the presented measurements is the signal to noise ratio. An amplifier which adds only little additional noise is therefore advantageous. For a single dc-SQUID readout the noise would be dominated by the read out electronics of the SQUID which is operated at room temperature. It provides the bias current I_b and reads out the voltage drop V_s. The low noise amplifiers operated at low temperatures are realized by the 2nd stage, a N-SQUID series array. The readout scheme is depicted in figure 4.6. The dc-SQUID is color coded in violet and is operated in voltage-bias mode, the N in series connected dc-SQUIDs working as low temperature amplifier (blue) are operated in a current-bias mode. The voltage drop

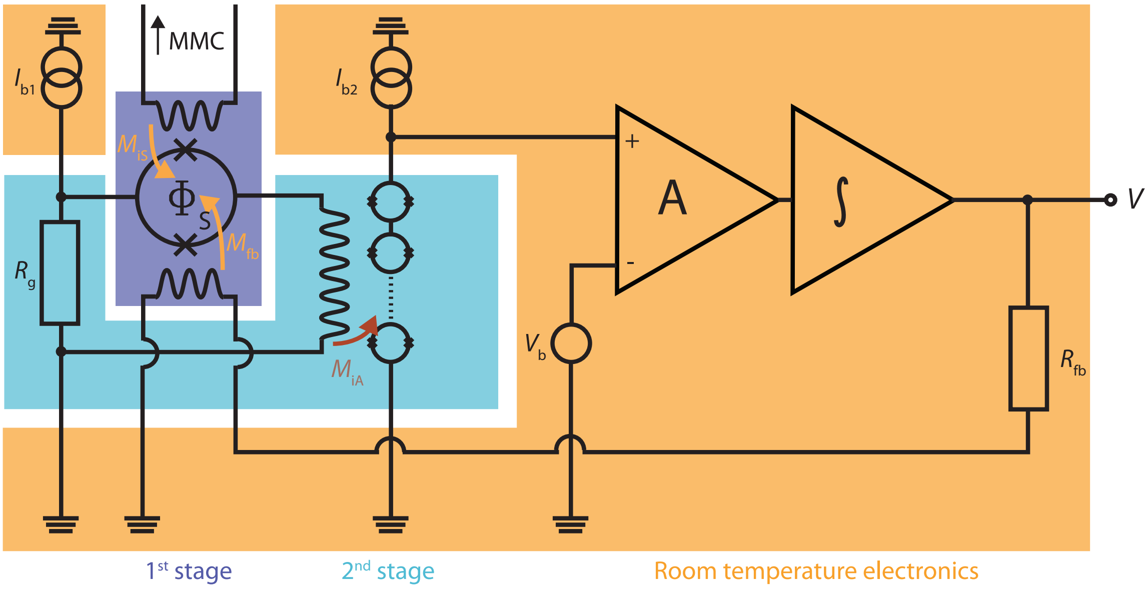

Figure 4.6: Schematic of a 2 stage SQUID setup. In orange are the parts of the read out electronics placed at room temperature. In violet is the front end SQUID and in pale blue is the second amplifier SQUID stage, both operated at mK temperature. (© D. Hengstler)

across that amplifier module is read out by room temperature electronics[1] (orange).

To linearize the signal a feedback mechanism is implemented that keeps the first-stage SQUID at a constant working point. All the current sources that are necessary to operate the SQUIDs are also part of the room temperature electronics as can be seen in picture 4.6. The second-stage SQUID array is operated with a bias current I_{b2} similar to the single dc-SQUID case. If all the N SQUIDs in series add up coherently for the same magnetic flux, their $V_{\mathrm{s}} - \Phi_{\mathrm{s}}$ characteristic is N times higher than the one of a single dc-SQUID in terms of V_{s}. To decrease the heat load next to the detector, where the front-end dc-SQUID is mounted, and to match the low impedance input of the 2nd-stage SQUID array the dc-SQUID is operated in a voltage bias mode. Therefore, is the bias current I_{b1} split between the front-end SQUID and a gain resistor R_{g}. If $R_{\mathrm{g}} >> R_{\mathrm{SQUID}}$ then the resistance of the SQUID defined by the working point, the voltage across the front-end SQUID stays almost constant and only a small current $I < I_{\mathrm{b1}}$ flows trough the SQUID and through the input inductance of the SQUID array. This way a change of magnetic flux Φ_{s} in the front end SQUID can be converted into a change of flux in the array. Since the gain resistor R_{g} can be located quite far away from the connected MMC, the power dissipation next to the detector can be minimized.

At this point the signal is amplified but still periodically for a change of flux Φ_{s}. By

---

[1] XXF-1 from Magnicon GmbH, Barkhausenweg 11, 22339 Hamburg, Germany

a flux-locked loop technique the signal is linearized. A change of flux Φ_s generated by an MMC in the front-end SQUIDs results in a change of current in the input coil of the second-stage amplifier SQUID. This creates an already amplified voltage drop across the SQUID array, which is further amplified with respect to an offset voltage V_b by a differential room temperature amplifier. This signal is integrated and fed back to the 1st-stage SQUID via a feedback resistance R_fb. The corresponding current I_fb flows through a feedback coil next to the 1st-stage SQUID and generates a flux $I_\mathrm{fb} \times M_\mathrm{fb}$ which compensates the initial change of flux $\Delta\Phi_\mathrm{s}$. This way the SQUID is kept at a constant working point in the $V_\mathrm{s} - \Phi_\mathrm{s}$ characteristics as can be seen in figure 4.5 **(right)**. The voltage drop across R_fb is then read out as linearized signal. To reach a good S/N the voltage offset V_b is chosen in a way that the $V_\mathrm{s} - \Phi_\mathrm{s}$ characteristics at the working point is the steepest and I_b1 and I_b2 are chosen that the voltage swing is maximal.

4.5 ECHo-1k: holder and circuit board

The ECHo-1k detector chips is glued to copper support structure, which can be mounted on the mixing chamber platform of the cryostat. Due to the good thermal conductance of the support structure and the platform, the temperature of the detector chip can be assumed to be the same as the one of the mixing chamber platform down to a certain temperature, which can be determined by a magnetization measurement. To improve the thermal contact between detector chip and copper support structure gold wires are bonded between the thermal baths on the chip and the underlying copper. The 1st-stage SQUIDs of the detectors for the read out are glued as well next to the chips on the copper holder. These front-end SQUIDs are connected via aluminum bonds with the detectors and the dedicated circuit board, which is the connection to the rest of the read-out chain. The aluminum bonds are kept as short as possible, since they introduce a parasitic inductance L_p, which increases with longer bonds. This worsens the inductive coupling strength M_{is} between SQUID and input coil and leads therefore to a smaller signal size. One prepared set up can be seen in picture 4.7. Here the gold bonds between the gold heat baths among each other and to the copper support structure as described in section 4.2 can be seen. Next to the detector the front end SQUID chips are located, each providing 8 front end SQUIDS. Furthermore, a small slit in the copper structure between the detector copper area and the SQUID copper area can be seen. Actually, the SQUID chips are glued on small copper bars which can be placed in holes in the copper support structure. They are fixed with srews from the outside. This way the SQUID chips can easily be exchanged if necessary without ungluing the whole set up. Furthermore, no direct good thermal contact between detector and SQUID is present

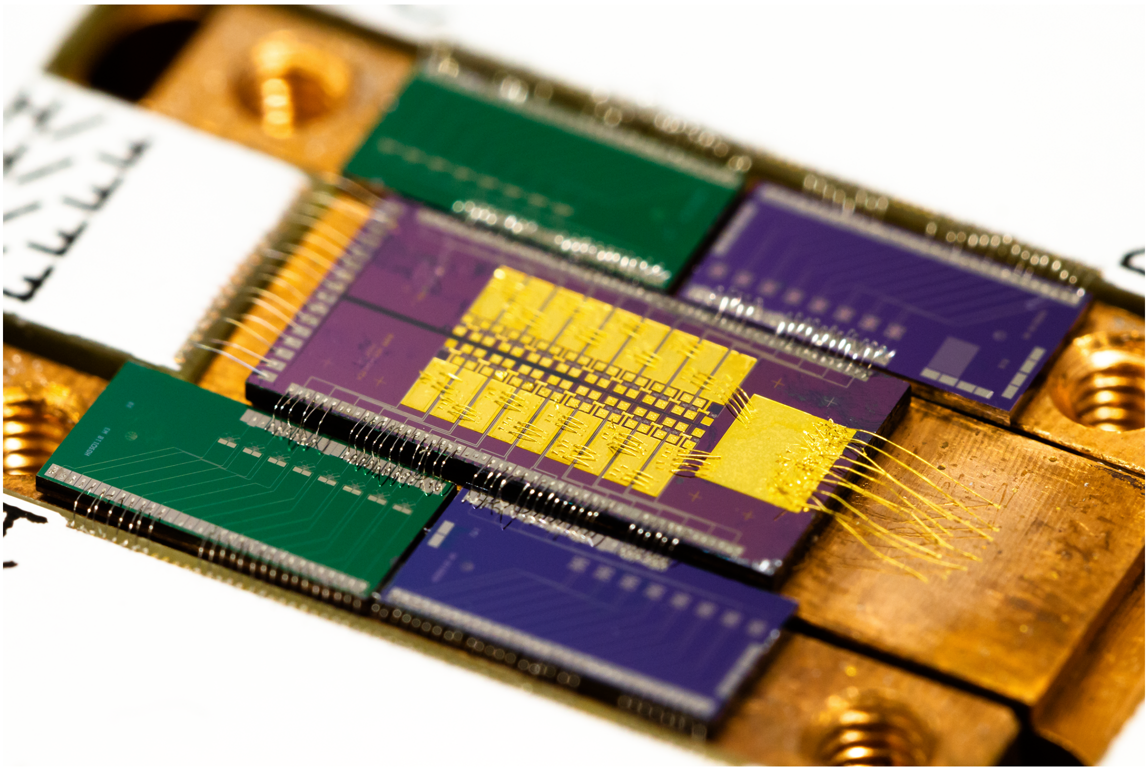

Figure 4.7: Detector chip together with front-end SQUIDs on a copper support structure, bonded to the dedicated circuit board.(© R. Hamann)

due to the slit. The aluminum bonds between these two are superconducting and have therefore a comparable bad thermal conductance. This way energy dissipated at the SQUIDs is prevented from directly flowing to the detector.

The copper support structure and the corresponding circuit board have been designed within this thesis. These parts are T-shaped, as can be seen in picture 4.8 **a)**. This way the whole set up can be shielded with an aluminum cup as it is shown in picture 4.8 **c)**. The cup itself gets superconducting below 1.2 K at the working temperature of the whole set up and has a good ratio between opening diameter of about 3 cm and a depth of 15 cm. This way external magnetic fields can not reach the front-end SQUIDs and the detector chip with high fluxes. The superconducting material expels all magnetic fields and the loop of the cylinder part of the cup conserves all magnetic fluxes. This leads to screening currents which keep the flux at the site of the detectors constant.

In picture 4.8 **b)** the used amplifier module is shown, which hosts the 2nd-stage SQUID read out. These modules are connected via superconducting wires with the circuit board of the detector chip. Here 12 channels are mounted on one module. Two array SQUIDs are hosted on one SQUID chip in the same superconducting cup.

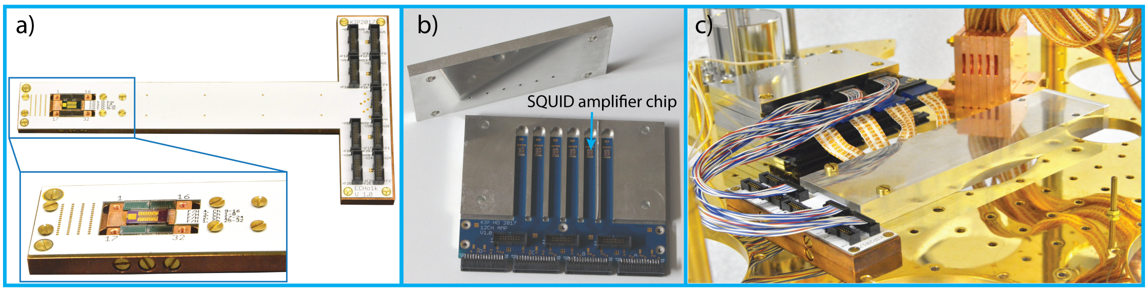

Figure 4.8: a) Detector chip mounted on the support copper structure, connected to the T-shaped circuit board. **b)** 2nd-stage amplifier module. **c)** Complete mounted experiment, including a aluminum shielding around the detector chip.

These modules are shielded as well with tin plated copper. These materials allow for a proper shielding, since the tin gets superconducting as well and the copper guarantees a good thermal conductance to transport the dissipated heat from the 2nd-stage SQUIDs to the mixing chamber of the cryostat. The full in the cryostat mounted and connected experiment can be seen in picture 4.8 **c)**.

5. Measurement of the heat capacity of ^{163}Ho ions in Au

To reach a sub-eV sensitivity on the effective electron neutrino mass within ECHo a ^{163}Ho energy spectrum with a good energy resolution and high statistics is needed. To achieve that goal the activity per MMC pixel needs to be maximized and the heat capacity per pixel needs to be minimized. The activity per detector should be high to maximize the number of decays per pixel per time period, which will bring more statistics with the same effort and therefore a higher sensitivity on the electron neutrino mass as described in chapter 2.3. A higher activity will bring a higher fraction of unresolved pile up events and an additional contribution to the total heat capacity of the detector C_{det} as well (see chapter 3.5). The heat capacity is a crucial detector parameter since it determines the signal height with $\Delta T = \Delta E/C_{\mathrm{det}}$ and influences the thermodynamic noise of the system. Because of this, the fundamental limit of achievable energy resolution for MMC's is given by $\Delta E_{\mathrm{FWHM}} \propto \sqrt{C_{\mathrm{det}}}$. As the maximum allowed activity per pixel a is basically defined by the fraction of allowed unresolved pile-up events f_{upu} to about $a = 10\,\mathrm{Bq}$ per pixel still the question remains, if such an implanted activity per pixel will spoil the needed energy resolution of the MMC. To define the optimal parameters for the ECHo experiment a measurement of the heat capacity due to a fixed number of ^{163}Ho ions implanted in a detector was performed. In the following the determination of the specific heat per Ho-ion in Au as host material will be discussed and the maximum allowed activity per pixel will be determined.

5.1 Experimental set up

The basic idea is to measure two identical MMC pixels, one with ^{163}Ho implanted, the other one without ^{163}Ho . As describe in 3.1 the signal height and shape are dependent on the thermodynamic systems which characterize the MMC. This allows to extract some thermodynamic properties of the additional ^{163}Ho in one of the MMC's by comparing the signals for the exact same energy input. In particular, if the signal shape due to a well-defined energy input of a pixel with implanted ^{163}Ho is compared to the one of a pixel without ^{163}Ho , the contribution to the total heat capacity due to the implanted ^{163}Ho ions can be determined. For this measurement an ECHo-1k detector chip was used, as described in chapter 4.2. This chip was implanted with ^{163}Ho at RISIKO in Mainz and the planned activity was about $1\,\mathrm{Bq}$.

As described in chapter 4.2 the chip has 72 detector pixels connected to 36 read-out channels gradiometrically. The chip was prepared in a way, that only 53 pixels where implanted with ^{163}Ho . For 7 double meander MMCs only one of the two pixels of the gradiometer was implanted. This allows further in-situ background studies, as described in chapter 7 and at the same time this asymmetric detectors can be used for a ^{163}Ho heat capacity measurement. The set up can be seen in picture 5.1. An external ^{55}Fe calibration source was used to irradiate both pixels. For the characterization of the signal shape, pulses generated by the K_α photons at 5.89 keV where used.

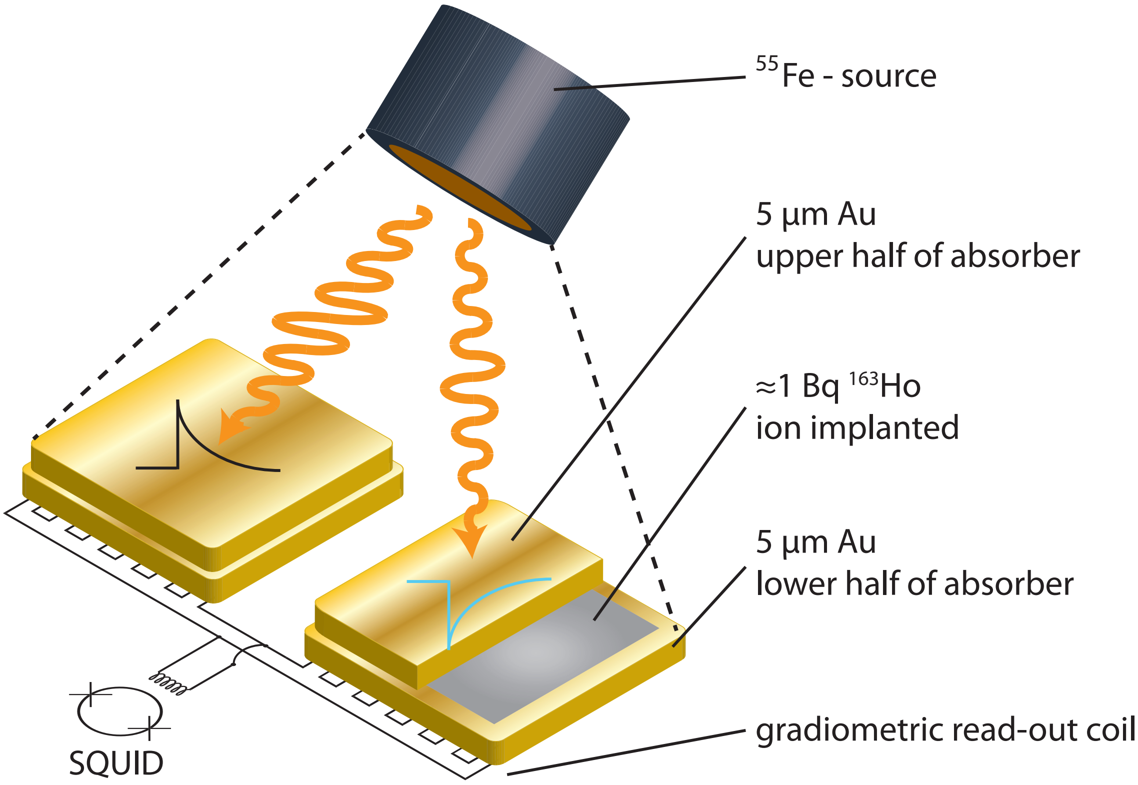

Figure 5.1: Schematic drawing of the experimental setup. One pixel is implanted with ^{163}Ho , the other one not. The pixels are connected gradiometrically and read out by the same front end SQUID. The signals are polarity coded.

Due to the same read-out chain for both pixels from the front end SQUID onward, differences in signal height and shape due to the read out chain are minimized. Furthermore, is the geometric difference between these pixels minimized by the close distance on the chip. This way differences in geometry which might be introduced during the fabrication process, e.g. small gradients in layer thicknesses, are reduced. In fact the later measurement of this chip presented in chapter 7 shows, that the same energy input for a nominally symmetric pixel pair (both implanted with ^{163}Ho) belonging to the same gradiometric setup leads to an identical measured voltage amplitude on a 2% level, checked for 11 pixel pairs.

In one pixel only photons from the ^{55}Fe-source are measured while in the other pixel also events due to the decays of ^{163}Ho are measured. For several temperatures between 10 mK and 85 mK the energy spectra have been obtained. The temperature has been adjusted by resistive heating at the experimental platform in the cryostat controlled by a PID-controller. Typically, the measurements were started after 10 minutes from the moment when the desired temperature was reached in order to avoid the tail of the transient. The thermometer feeding the PID-controller was mounted on the experimental platform. Already after 3 min. no significant change of signal amplitude for the MMC's for a fixed energy could be seen. The temperature control itself was regulated on a ±0.5 mK level, which was sufficient for this experiment and reduced the adjustment time for a planned temperature drastically. In principle way better temperature stabilizations can be reached. The measurement took about 1 hour until roughly 1000 counts in the K_α-line of the ^{55}Fe-source where reached. In addition one longer measurement at 12 mK has been performed to extract the detectors performance and the activity of ^{163}Ho in the implanted pixel. Furthermore, the persistent current that is provided to create the static magnetic B-field for the Ag:Er sensor has been changed once from 20 mA to 50 mA.

5.2 HC of ^{163}Ho -ions in Au: Results

The achieved energy resolution at 12 mK was $\Delta E_{\mathrm{FWHM}} = 23.5$ eV extracted from the K_α-line at 5.89 keV as can be seen in figure 5.2. This result was obtained by fitting a convolution of the Gaussian detector response and the intrinsic Lorentzian line-shape of the ^{55}Fe - K_α line. The free fitting parameter was the width of the Gaussian detector response. This energy resolution is about 5 times higher than the expected one following the simulations for this detector as described in 3. The deviation can be explained by an increased read out noise which was specifically present in this measurement. The responsible parts in the read out chain have been changed for all further measurements. However, the measured energy resolution introduces an error on the amplitudes of the signals of about 0.07% and can therefore be neglected. In good approximation is the amplitude A of the signal directly proportional to $1/C_{\mathrm{tot}}$. A comparison of the amplitudes of the two pixels with and without implanted holmium directly gives a difference in heat capacity for two otherwise identical MMC's.

In picture 5.3 two typical averaged pulses measured at 58 mK with a provided current of 20 mA and an energy input of 5.89 keV for each pixel are shown. Given is the

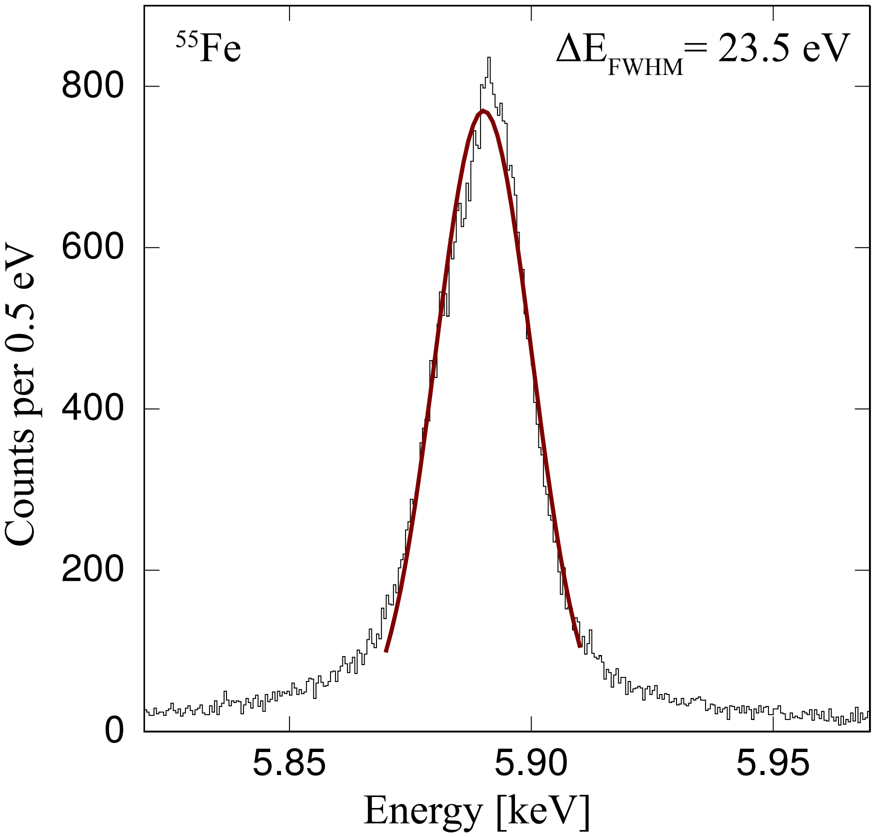

Figure 5.2: Energy spectrum of the ^{55}Fe - K$_\alpha$ line measured at 12 mK with 50 mA persistent current. This pixel contained ^{163}Ho . The detector energy resolution at 5.89 keV is $\Delta E_{\mathrm{FWHM}} = 23.5\,\mathrm{eV}$.

output voltage at the end of the read out chain versus time for the triggered signal. The time window was chosen to be about 2 ms in total, which allows to resolve the fast rise time of the signal. In blue is the signal of the MMC with ^{163}Ho implanted and black is the signal of the pixel without ^{163}Ho . The rise time of both pulses is about 1 μs. This time is not the intrinsic rise time of about 100 ns as expected from the coupling of the electron system to the spin system of the sensor material described by the Korringa constant as presented in chapter 3.2.2, but is limited by the low pass behavior of the readout chain. Both pulses show a typical decay time of several ms. A slightly longer decay time is observed for the pixel with implanted ^{163}Ho . As described in chapter 3.4.2 this decay time can be approximated for MMCs with $\tau_{\mathrm{d}} \approx C_{\mathrm{det}}/G_{\mathrm{link}}$. The heat conductivity G_{link} defined by the weak thermal link is by design the same for both pixels. The larger decay time τ_{d} can therefore be explained with a larger heat capacity C_{det} for the pixel implanted with ^{163}Ho .

The signal in the pixel with ^{163}Ho implanted is significant smaller for the same energy

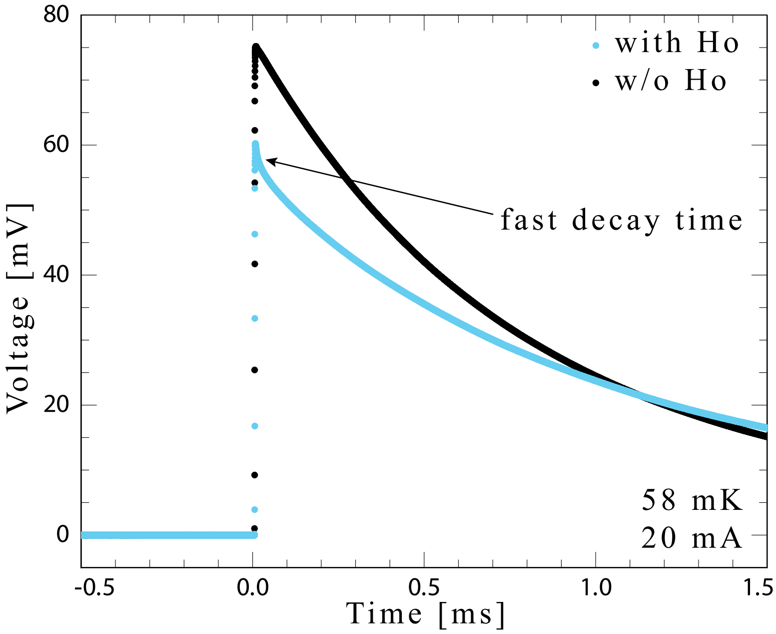

Figure 5.3: Signal comparison between the pixel with ^{163}Ho and without ^{163}Ho at 58 mK and 20 mA persistent current for the same energy input of 5.89 keV. The shown signals are an average of about 1000 pulses.

input. Furthermore, an additional fast decay time in the 10 μs range can be seen, which is not present for the pixel without ^{163}Ho implanted. Figure 5.4 shows the signal shapes for the two pixels for all measured temperatures within a 2 ms time window for **a)** and **b)**. In figure 5.4 **c)** and **c)**, the time window is 40 μ s and the y-axis is logarithmic. Shown is the digitized voltage signal. In the top row in figure 5.4 **a)** and **b)** is shown, that for all measured temperatures the pixel with ^{163}Ho implanted always has a significant smaller amplitude for the same energy input. Furthermore, the amplitude of the signals for both pixels changes for the change of temperature of the thermal bath especially from 16 mK to 11 mK, which allows to conclude that the chip temperature still follows the bath temperature. This was achieved with a very good thermal coupling of the detector chip to the thermal bath via gold bonds. In both figures a change of the long decay time $\tau_\mathrm{d} \approx 10\,\mathrm{ms}$ for higher temperatures to faster decay times can be observed. As mentioned above, this time is approximated with $\tau_\mathrm{d} \approx C_\mathrm{det}/G_\mathrm{link}$ and the decrease for higher temperatures for such an MMC detector is expected [Fle03].

In the lower row in figure 5.4 **c)** and **d)** both pixel signals show the expected behavior of a decrease of decay time in the ms range due to the change of heat capacity with temperature and the change of thermal conductance of the weak thermal link as described in 3.2.2. The fast decay time present in the signal of the pixel with

^{163}Ho implanted is temperature dependent as can be seen in picture 5.4 **d)**. For temperatures up to 16 mK this fast decay is not noticeable. From 36 mK to 83 mK it changes from about $\tau_\mathrm{r} = 10\,\mu\mathrm{s}$ to $\tau_\mathrm{r} = 5\,\mu\mathrm{s}$. This behavior can be explained

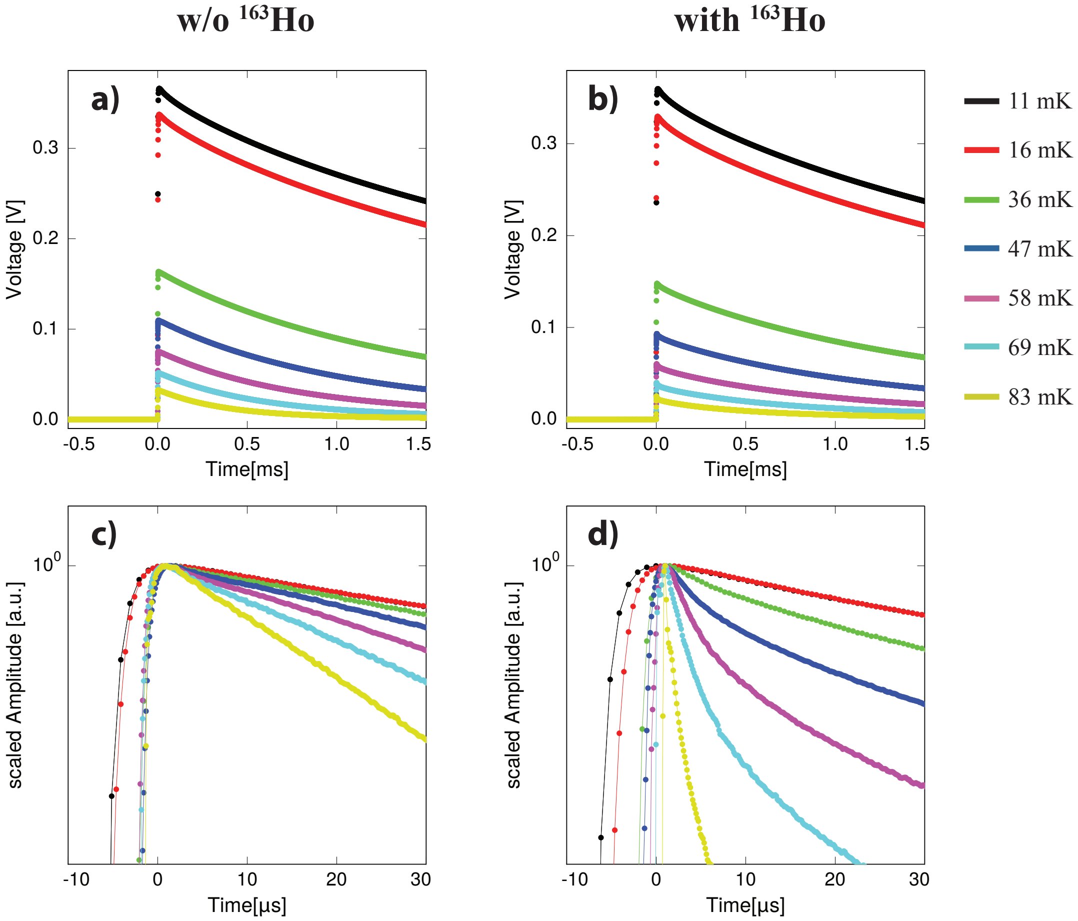

Figure 5.4: a) and **b)** show signals from the pixels without and with ^{163}Ho for 5.89 keV energy input for different bath temperatures. The persistent current was 20 mA. **c)** and **d)** show the corresponding zoom of the to maximum of the signals. The voltage is plotted here on a logarithmic scale. The signals have been scaled and shifted to have the maximum at the same position at 1.

by an extension of the schematic heat capacity drawing 5.5. The new extended scheme is shown in figure 5.5. By introducing another heat capacity system C_ho connected to the heat capacity system of the electrons C_e this fast decay time can be explained. As described in chapter 3.2.2 for a thermodynamic system with two sub-systems connected to a thermal bath the signal shape can be described by just two time constants. To introduce a new time constant, another sub system needs to be added. The new sub system C_ho corresponding to this new decay time is

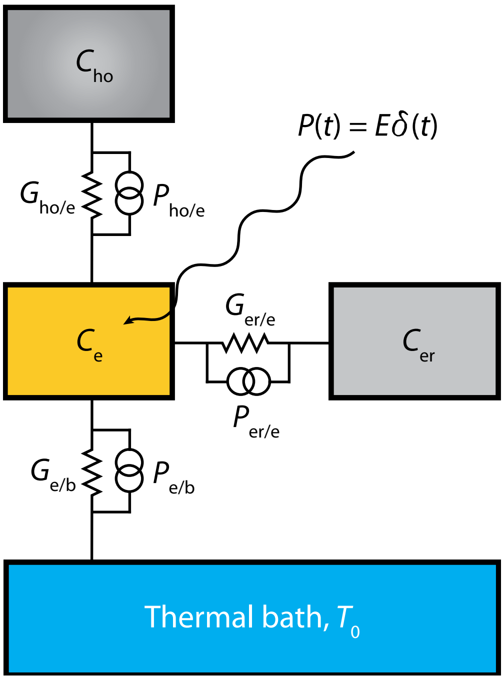

Figure 5.5: Drawing of the thermal subsystems present in the MMC with ^{163}Ho implanted.

most probably introduced by the implanted holmium ions. As described in chapter 3.2.2 the measured signal is proportional to the change of magnetization due to a temperature change in the system of the Er-ions C_{er}. The thermalization of the electron system C_e and C_er happens on a ns timescale, afterwards the whole system thermalizes on a ms timescale with the thermal bath. If now an additional heat capacity system C_ho is coupled on a microsecond timescale to C_e, C_e and C_er will still thermalize very fast and the maximum amplitude of the signal will correspond to the heat capacity of the two sub systems following $A \propto E/(C_\mathrm{e} + C_\mathrm{er})$. Now these two sub systems together thermalize with C_ho on a μs timescale which drops the amplitude fast, since now the energy is distributed among all three subsystems.

The interesting amplitude, which has the heat capacity information of all three subsystems needs therefore to be extracted by the amplitude corresponding to the signal decaying with the ms timescale to the bath. Since all thermalization processes start at once the amplitude of the ms signal, already starts to decay once the energy is deposited. To extract the full amplitude corresponding to the heat capacity of all three sub systems the ms decay needs to be fitted and extrapolated to the beginning of the pulse. So for every temperature the amplitude of the signal with ^{163}Ho was extracted by fitting an exponential decay to the signal, excluding the first fast decay and extrapolating this fit to $t = 0$, the time of the energy input.

5.3 Relative contribution of implanted Ho-ions to the HC of an MMC

The most important quantity for the ECHo project in this measurement is the relative change of heat capacity of the detector system due to ^{163}Ho . It is given with:

$$\frac{A_{\mathrm{w/o}} - A_{\mathrm{Ho}}}{A_{\mathrm{Ho}}} = \frac{C_{\mathrm{ho}} - C_{\mathrm{w/o}}}{C_{\mathrm{w/o}}} = \frac{\Delta C}{C_{\mathrm{w/o}}} \tag{5.1}$$

This quantity was calculated for every temperature for both persistent currents as shown in figure 5.6. The label $^{*}_{\mathrm{w/o}}$ describes the corresponding quantity of the pixel without implanted ^{163}Ho . While the qualitative behavior for the two provided currents is almost identical the curve for the 50 mA current is shifted towards higher temperatures. This is expected since here the relative change of heat capacity is

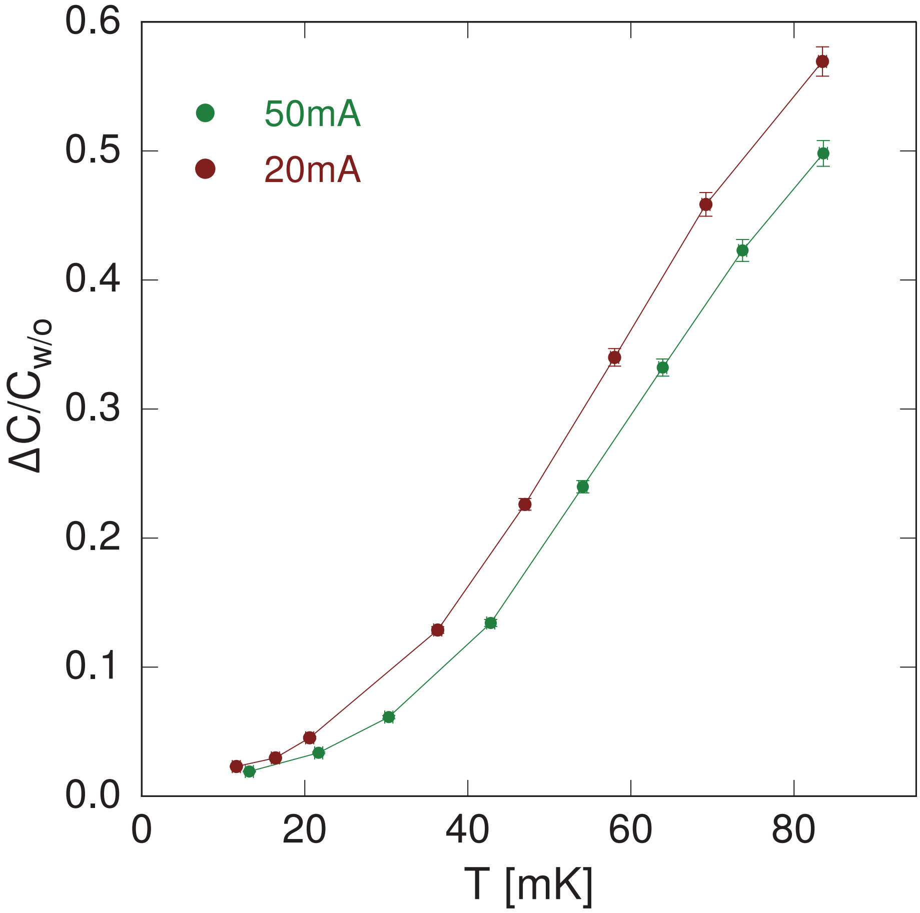

Figure 5.6: The relative change of the total detector heat capacity $C_{\mathrm{w/o}}$ due to the implanted ^{163}Ho for different temperatures and different persistent currents.

plotted. While the heat capacity of the electron system C_e and the heat capacity of the holmium system C_ho is not affected by a higher magnetic field due to a higher provided persistent current, the heat capacity of Er-ion system C_er increases.

The implanted activity was estimated with $a = 0.9$ Bq extracted from the long measurement by the number of counts in the MI resonance line of the ^{163}Ho energy spectrum and the total time of the measurement. Here the simple 7 resonances ^{163}Ho theory was assumed to calculate the relative spectral weight of the MI resonance line. This way the measured activity can be scaled to the total amount of implanted activity with $a = 0.9$ Bq. For this amount of holmium an increase of about 4 % in total heat capacity of the detector was measured at 20 mK.

For optimal read out conditions, where the energy resolution is determined by the thermal fluctuations of the heat capacity systems, a 2% worsened energy resolution then without ^{163}Ho can be expected for about 1 Bq of ^{163}Ho , following $\Delta E_\mathrm{FWHM} \propto \sqrt{C_\mathrm{tot}}$. This change is negligible small.

5.4 Specific heat per Ho-ion in Au

To extract an absolute value for the single pixel, the voltage signal needs to be converted into a temperature signal by knowing the calibrating magnetization curve measured as change of voltage per change of temperature. Once the temperature pulse is obtained, the total heat capacity of the detector can be extracted by the analysis of the temperature due to a known energy input following $\Delta T = \Delta E / C_\mathrm{det}$. Of course is the heat capacity C_det temperature dependent as well, but can be considered to be constant in good approximation for the typical $\Delta T = 1\,\mathrm{mK}$ and $T_\mathrm{bath} > 10\,\mathrm{mK}$. The energy input is well known with 5.89 keV as energy position of the main photon peak of the used ^{55}Fe source. The absolute change of temperature is dependent on the magnetization $\Delta M / \Delta T$ of the sensor material and the coupling factors between the change of magnetization in the meander and the final change of voltage measured at the ADC. The coupling factor of $3.83\,\mathrm{V}/\phi_0$ was measured for the here used detector channel. The magnetization can be measured with the temperature channel present on the ECHo-1k detector chip. This channel follows as well the gradiometric design but on the one meander only the Ag:Er temperature sensor is present and on the other pixel just the bare meander is realized. This way changes of temperature on the substrate lead to a change of output voltage at the SQUID electronics. For this measurement the mixing chamber of the cryostat is heated to about 600 mK for 5 minutes, to ensure that the whole experimental platform and especially the detector chip has a comparable temperature. Then the heater is switched off and the whole system cools down again to the base temperature of the cryostat. Due to the good thermal coupling of the detector chip to experimental platform the temperature of the detector chip follows the temperature of the experimental platform down to 10 mK. Clearly this change of temperature leads to a change of magnetization in the sensor of the temperature pixel, which in turn leads to a change of voltage on the output of the SQUID read out. This change of magnetization is only dependent on the distribution and number of Er-ions in the sensor and the $B-$field distribution due to the applied current in the meander and the meander shape. In figure 5.7 **a)** the change of flux in the input coil of the front-end SQUID is shown versus $1/T$ (solid lines). The output voltage is converted into this change of flux by the charac-

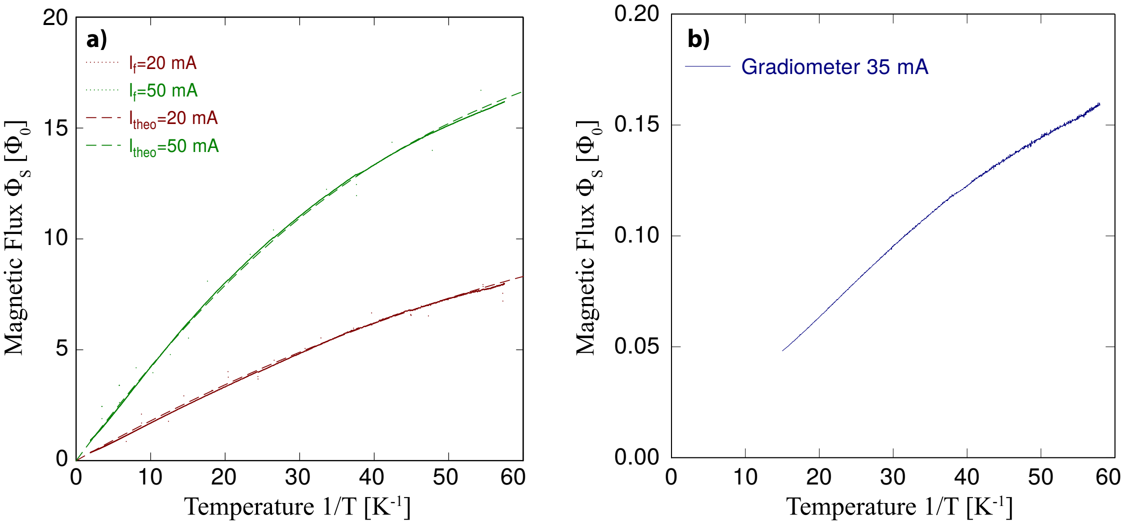

Figure 5.7: a) (solid lines) Magnetization of the temperature detector on the ECHo-1k chip for 20 mA and 50 mA frozen in current. (dashed lines) Simulation of the magnetization of the MMC system. **b)** Magnetization of a symmetric gradiometric pixel pair.

teristics of this specific read out chain. A numeric simulation of the sensor material for feedback parameters and the meander and sensor geometries of the discussed detector gives the dashed line as the expected change of flux. In this simulation the interaction of the Er-ions in a B-field enters [Fle03], as well as the sensor geometry, the measured Er concentration of the sensor and the persistent current. Since the behavior of the Er-ion system was simulated for Er in Au, scaling laws deduced in [Hen17] have been applied as well, to account for the Ag host material. Theory and experimental data are in very good agreement. In figure 5.7 **b)** the magnetization of a nominally symmetric pixel pair is shown. As can be seen small asymmetries in this pixel pair lead to a finite change of magnetization. The persistent current for this measurement was 35 mA. The expected error for the magnetization measurement of the detector is given by the comparison of the two magnetization measurements with about 1%.

Now for every amplitude at a certain temperature for a provided current the slope of this magnetization curve can be extracted as $\Delta M/\Delta T$ to calculate the absolute change of temperature.

The difference of the two amplitudes can then be considered to be the amplitude corresponding to the heat capacity of the ^{163}Ho system and an absolute value for the heat capacity for both used currents can be given. The result is plotted in figure 5.8. As expected no significant deviation for the two persistent currents can be seen.

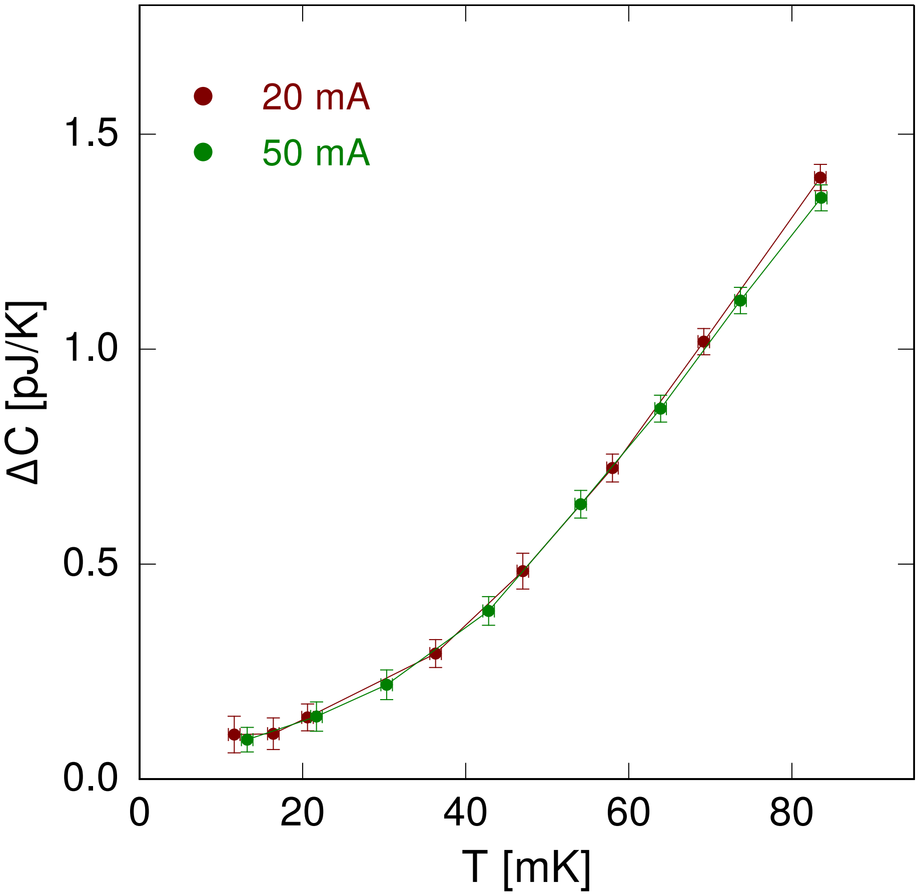

Figure 5.8: Total heat capacity due to ^{163}Ho for different temperatures and persistent currents.

The error in the input energy is well below 1 % as explained above, the error of the slope of the flux in the SQUID as well the error on the coupling factors of the read out chains are in the order of 1 %. Together with the maximum difference of about 2% in signal amplitude between 2 pixels belonging to the same gradiometric set up measured for 11 pixel pairs, the error on the total heat capacity of the holmium system is calculated. The error on the temperature is about 0.5 mK.

This measurement fits quite well with measurements done by M. Herbst and A.

Reifenberger [Vel19b] as can be seen in figure 5.9. The data for bulk holmium is taken from [Wil69]. Note that all other here presented measurements where performed with ^{165}Ho, which should behave exactly like ^{163}Ho in terms of thermodynamic properties, since ^{165}Ho as a nuclear moment of $I = 7/2$ as well.

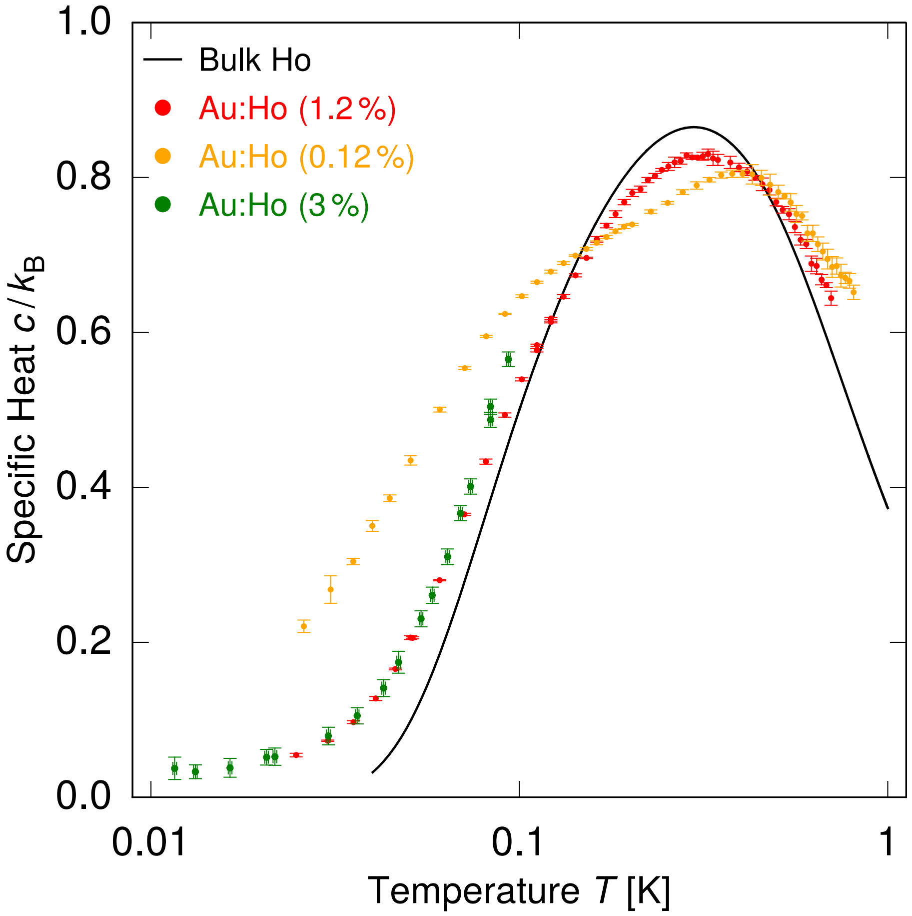

Figure 5.9: The change of the specific heat per Holmium atom versus temperature for different concentration of Au:Ho. The 3%-sample is the in this thesis measured specific heat.

As explained in [Wil69] is the specific heat of bulk holmium well understood. In bulk holmium only crystal field effects and hyperfine splitting play a significant role for the heat capacity at low temperatures. Both effects give rise to a Schottky anomaly. This anomaly occurs for two level systems naturally. For low temperatures only the ground state is occupied. With increasing temperature more and more electrons can occupy the excited state, more possible energy states are available, which corresponds to a broad peak in heat capacity. For higher temperatures both energy levels are more and more evenly occupied which decreases the heat capacity again. The Schottky peak for bulk holmium is at about 250 mK with a height of about $0.9\,k_\mathrm{B}$. The dipole-dipole interaction and the RKKY interaction do not play a significant role.

The $x_\mathrm{Ho} \approx 3\,\%$ sample measured within this thesis follows almost completely the curve for bulk holmium, which leads to the conclusion, that in this sample the hyperfine splitting and the crystal field contribution to the heat capacity play a major role. However, the measured data lies slightly above the specific heat of bulk holmium over the entire measurement range, most notably at around 40 mK. The average ^{163}Ho concentration of $x_\mathrm{Ho} \approx 3\,\%$ can be calculated by the measured activity, which allows to deduce a number of total ^{163}Ho -ions and the implantation volume, which is simulated in [Gam17]. These simulations show as well that small spacial deviations in concentration down to 1 % are possible. In general have samples with a rather low concentration of Ho-ions in average a larger distance between the holmium atoms, holmium-holmium interactions are therefore significantly weaker and the resulting effects of this holmium-holmium interactions manifest themselves at lower temperatures. The corresponding contribution to the heat capacity is no longer hidden underneath the Schottky anomaly of the hyperfine splitting and the crystal field effects. We thus observe a clear shoulder around 90 mK for the $x_\mathrm{Ho} \approx 0.12\,\%$-sample. Due to the areas with lower concentrations in the $x_\mathrm{Ho} \approx 3\,\%$-sample, this effect can also be seen for this measurement.

Due to a different measurement technique the samples with lower holmium concentration could be measured across the entire Schottky anomaly. By comparing these results with the $x_\mathrm{Ho} \approx 3\,\%$-sample it gets obvious that the obtained heat capacities for the $x_\mathrm{Ho} \approx 3\,\%$-sample and the $x_\mathrm{Ho} \approx 1.2\,\%$-sample are in very good agreement.

Due to the two completely independent measurements techniques two conclusions can be drawn. While the here presented measurement technique works on a μs to ms time scale the measurement technique for the other samples has a time scale of minutes. Due to this fact it is likely that all for the heat capacity the relevant processes have relaxation times of ms. Therefore, the $x_\mathrm{Ho} \approx 3\,\%$-sample should follow the $x_\mathrm{Ho} \approx 1.2\,\%$-sample and have a maximum at about 300 mK. The second conclusion is the fact that the implantation process itself seems not to influence the heat capacity of the detector on a significant level by e.g introducing defects in the Au matrix.

5.4.1 Significance for the ECHo Project

This results of the specific heat per Ho-ion in Au have 3 implications for the ECHo project, which are presented in the following.

Holmium Concentration

The holmium concentration has a direct impact on the specific heat of the material. For temperatures $T \lesssim 50\,\mathrm{mK}$, higher holmium concentrations of $x_{\mathrm{Ho}} < 2\,\%$ are advantageous, since they provide a lower heat capacity. The simulations of the implantation process of ^{163}Ho [Gam17] have shown, that for the current implantation procedure a saturation at about $3\,\mathrm{Bq}$ is expected due to back scattering effects, while the beneficial holmium concentrations of above $2\,\%$ are reached. This procedure will be changed to overcome the saturation effect by the co-implantation of Au. At this point an optimization towards holmium concentrations above $2\,\%$ is preferable.

Temperature

The typical operating temperature of an MMC is about $T \leq 20\,\mathrm{mK}$. At this low temperature the additional heat capacity due implanted ^{163}Ho is small. Just taking in consideration this heat capacity contribution lower temperatures are even more preferable, although the effect gets marginal.

Activity a per pixel

With the absolute value for the specific heat per Ho-ion in Au a maximal allowed activity a per pixel can be estimated, under the assumption that the heat capacity due to implanted ^{163}Ho is kept below the sum of the heat capacities of absorber and sensor. This amount of total heat capacity still allows for an acceptable energy resolution. The here measured $x_{\mathrm{Ho}} \approx 3\,\%$-sample yields a heat capacity of $3.3\,\mathrm{pJ\,K^{-1}}$ at $20\,\mathrm{mK}$ for the non-implanted pixel of the gradiometric set-up. From figure 5.9 a specific heat per ^{163}Ho ion of $0.05\,k_{\mathrm{B}}$ at $T = 20\,\mathrm{mK}$ can be extracted for the typical MMC with implanted ^{163}Ho used in ECHo. This allows implanting of about $37\,\mathrm{Bq}$ (equivalent to 5×10^{12} ^{163}Ho ions), before the combined heat capacity of sensor and absorber is reached. The planned activity of about $a = 10\,\mathrm{Bq}$ per pixel [Gas17] is therefore no problem. This $a = 10\,\mathrm{Bq}$ per pixel corresponds to about $40\,\%$ more total heat capacity of the MMC at $20\,\mathrm{mK}$, which worsens the energy resolution by a factor $\Delta E_{\mathrm{FWHM}} \propto \sqrt{C_{\mathrm{tot}}} = \sqrt{1.4} \approx 1.2$, if the energy resolution is determined by the thermodynamic energy fluctuations of the system for an ideal read out chain.

6. Experimental Results: Modane

In 2014 an MMC detector chip could be operated in the underground laboratory in Modane[1]. The goal of this measurement was to compare the performance of the detectors obtained in the underground lab with the one obtained operating the same detector in the laboratory of the Kirchoff-Institute for Physics above ground in terms of signal shape, energy resolution and background.

.

6.1 maXs-20 detector array with implanted ^{163}Ho

A maXs-20 detector-chip was used for this experiment as described in chapter 4.1. The results of this measurement are compared with a measurement above ground presented in [Has16] with the exact same detector chip.

The ^{163}Ho ion implantation was performed at ISOLDE, CERN in an offline process. For this implantation a chemically purified Ho-source was used [Dor18]. No radioactive contaminants besides $^{166\mathrm{m}}$Ho were detected by an x-ray measurement. $^{166\mathrm{m}}$Ho was present on a level of 10^{-4} compared to ^{163}Ho . After the mass selection during the ion implantation of ^{163}Ho , we expect no radioactive contamination on a relevant level anymore.

The used maXs-20 detector included the described stems, which should reduce drastically the athermal phonon loss to the substrate after a decay. This athermal phonon loss lead to low energy tails in the spectral shape of ^{163}Ho , observed in a previous experiment with MMCs implanted with ^{163}Ho [Ran17]. Already in [Has16] have been shown that these low energy tails are reduced to a not noticeable level with the introduction of stems.

In the underground lab the experiment is shielded by rock with 4800 m of water equivalent. There the number of impinging cosmic muons in the detector should be reduced by a factor of 10^6. This allows a direct comparison of the background rate from this below ground measurement with a second measurement performed in a lab in Heidelberg at sea level. It should indicate the need to perform the high statistics measurements below ground or with an active muon veto.

We were able to obtain a very clean ^{163}Ho spectrum in the underground lab with no radioactive contamination visible on the sensitivity level that was reached during

---

[1] http://www.lsm.in2p3.fr/

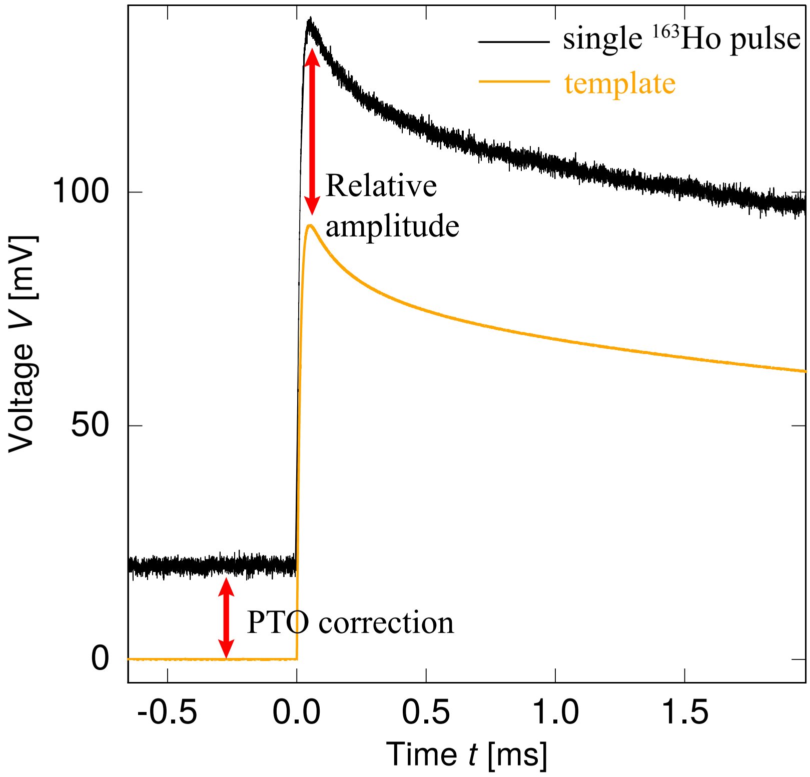

Figure 6.1: Typical triggered pulse, 16384 samples, 2 ms time window, 0.5 ms time window before the signal was triggered.

the measurements (see picture 6.2 **a)**). The measured activity per pixel was about 0.18 Bq. Four pixels were operated for 4 days for this underground measurement. The measurement above ground had 2 working pixels measured for 24 hours. For the data obtained a dedicated analysis structure has been established, which has been used for the second ^{163}Ho energy spectrum measurement as well presented in chapter 7. In the following the applied steps are discussed from the single event data to the final ^{163}Ho energy spectrum.

6.2 Data reduction

The single events are acquired with an ADC in a triggered mode. Whenever a change in voltage exceeds a certain threshold, the signal is recorded with a sampling rate of 125 MHz, an oversampling of 16 and a sample length of 16384. A typical pulse is shown in picture 6.1 (black). Here the first 4196 samples are recorded before the signal was triggered (pre-trigger). The distance from zero to the mean of the pre-trigger is called pre-trigger offset (PTO). The signal has a typical rise time of $\tau_r = 1\,\mu s$ and decays within $\tau_d \approx 5\,\text{ms}$. The rise time τ_r was limited by a low pass filter, introduced by the read out chain and does not correspond to the intrinsic rise time of the detector. In a first order approximation, where the change of temperature due to a signal is much smaller then the bath temperature $\Delta T << T_{bath}$ the signal shape is energy independent as described in 3.1. Figure 6.2 **d)** shows three single pulses corresponding to a deposited energy of 0.4 keV, 2.04 keV and 6.5 keV. These are normalized in amplitude. The template pulse, obtained by averaging about 1000 pulses of energy 2.04 keV is super imposed as well. The 4 traces have over the full time window the exactly same shape. The only visible difference is the noise of the signal which is constant for all pulses, but scales with the scaling factor A in this picture. Due to small changes in signal height and shape for different pixels and different read out chains the corresponding sub data sets analyzed individually.

For every data set a template fit is performed, where the template is generated out of about 1000 triggered signals with an energy of 2.04 keV. The generated template is a noise reduced pulse as depicted in 6.1 (orange). The template is used to fit every single recorded pulse belonging to one data set, having just a relative amplitude A and a PTO shift as free fit parameters. During this fit several additional parameters are determined, like the a χ^2-value as a measure on how similar the reference template is to the single fitted pulse. The χ^2-value is a good indicator for differences in pulse shape. The colors in figure 6.2 **d)** of the signals match the colored circles in figure 6.2 **b)**. There the relative amplitude A is plotted versus the χ^2-value of the fit. Signals with the same signal shape cluster around a χ^2-value, for this data set around 6.5×10^{-4}. This fact allows the first reduction of the data to exclude events with a different pulse shape. The higher the χ^2-value, the bigger the difference in signal shape. In figure 6.2 **c)** a signal with relatively high χ^2-value is shown. In particular this is a pile-up event where after a decay in one pixel, a second decay occurred in the second pixel of the double meander. Therefore, the second signal has opposite polarity. Again the color of the signal matches with the color of the circle in figure 6.2 **b)** which denotes the position of the signal in the rel. amplitude vs. χ^2 plot. This signal is a pile-up event where a second pulse in the other meander of the detector is visible during the event since both pixels are read out by the same SQUID. With the assumption that most of the triggered signals are "good" events a centroid of the χ^2-values can be automatically found and used to apply a 5σ cut. After the mean of the centroid is determined only 5σ-band around the mean is kept. The centroid can be seen in the histogram of the χ^2-values in figure 6.2 **e)**. The mean-value of the χ^2-distribution is indicated by the red line in figure 6.2 **e)** & **b)**. The orange dashed lines denote the 5σ band. With this cut about 99 % of the data is kept. The 5σ cut is a trade off between the need to keep as much signals as possible and to exclude as much background signals as possible. Assuming a Gaussian distribution around the mean of cloud the 5σ seem to be reasonable as can be seen in picture 6.2 **e)**. Especially towards lower energies, the χ^2-value calculated from the fit is not a

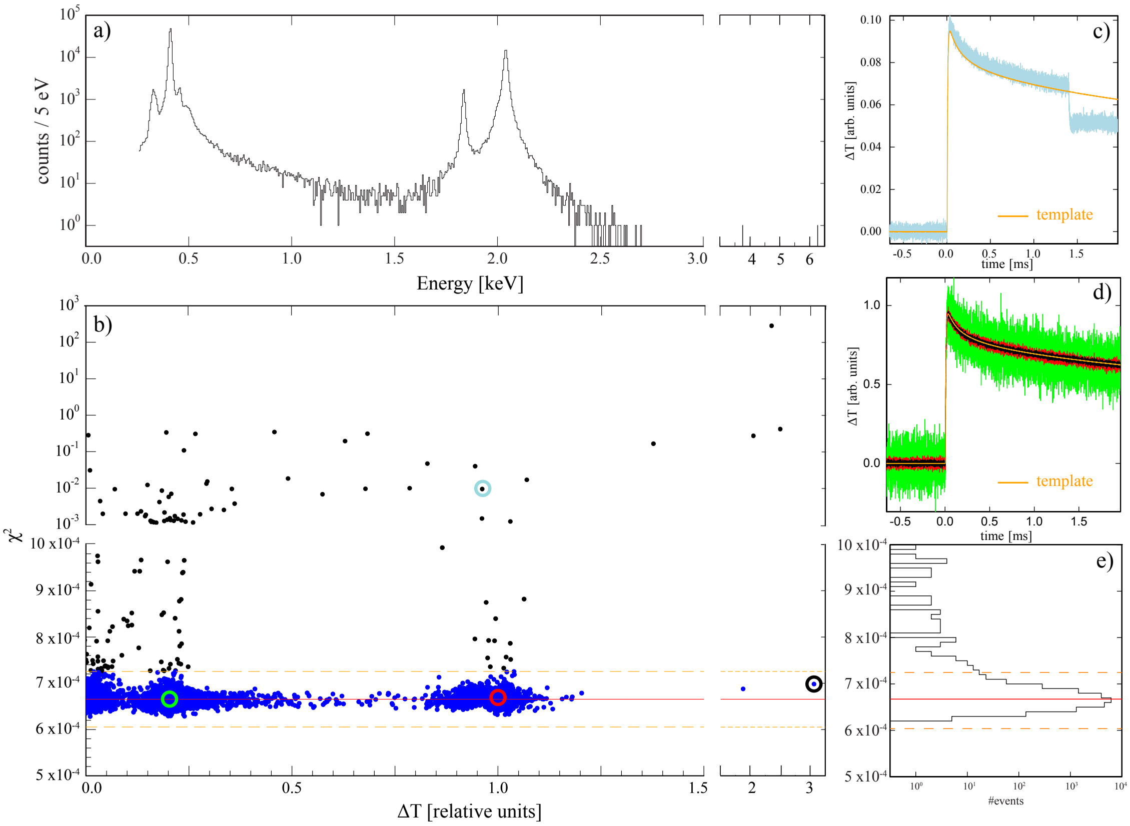

Figure 6.2: **a)** ^{163}Ho energy spectrum. **b)** Relative signal amplitude versus the χ^2-value of the template fit. **c)** Pile-up event. **d)** Three events with different energies scaled to one. **e)** Histogram of the χ^2-values.

very precise measure for background events. This is due to the low signal to noise ratio (S/N) for this region. Here more advanced techniques like a Kalman filter or machine learning algorithms could be used to achieve a better distinction between real and unwanted signals.

The next step is a pre-trigger offset correction. As can be seen in figure 6.3 showing the mean of the pre-trigger versus time for one detector pixel the PTO is not stable over time but presents a well-defined jump due to a change of working point in of the SQUID read out. It stays for several hours at one level and jumps then to another level. This can happen several times during one acquisition to several different values of the PTO. As described in chapter 4.4 the SQUID read out is linearized by a feedback loop. The working point of the SQUID is chosen to be at the steepest slope of the ϕ-V curve. Due to the sinusoidal character of this curve this point is not unique due to a discrete offset in V. The in figure 6.3 shown jumps correspond well to the measured $3.6\,\mathrm{V}/\phi_0$, which gives exactly the difference in V for two working points of the SQUID. In principle, due to the same slope at any of these working

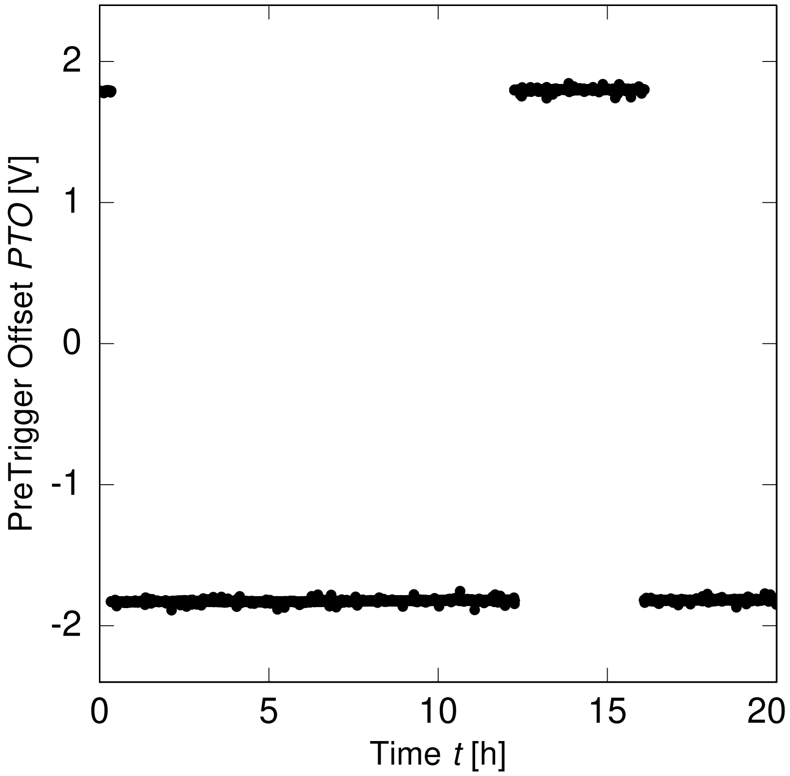

Figure 6.3: Pre-trigger offset versus time of a single data sub set.

points, the read out characteristics should be the same for any discrete offset of V. A different working has a different gain. This needs to be corrected by splitting the data sets in sub-files corresponding to time intervals with the same PTO. For future experiments these jumps might be reduced a lot by a well stabilized temperature and an improved electromagnetic shielding of the read out chain. In picture 6.3 the PTO is for 12 h at about -1.8 V, then jumps to an PTO-level of $+1.8$ V for 4 h, and jumps back again for the last 4 h. Even for the in principle identical PTO-level of -1.8 V the data files need to be split, since they have a small difference in gain before and after the jump to $+1.8$ V. This can lead to very small sub sets of data, which can later on not be processed any further, since it is necessary to recognize the spectral shape of ^{163}Ho for further calibration for each data set. In addition, PTO jumps corresponding to a fraction of ϕ_0 have been observed and could be due to parasitic magnetic field coupling to the SQUID. Also these have been corrected. As discussed in chapter 3.1 the signal shape and height are temperature dependent.

Although the temperature of the mixing chamber of a dilution refrigerator where the experiment was mounted was temperature stabilized small drifts of the chip temperature occurred. These are corrected in the following step. In a perfect scenario the

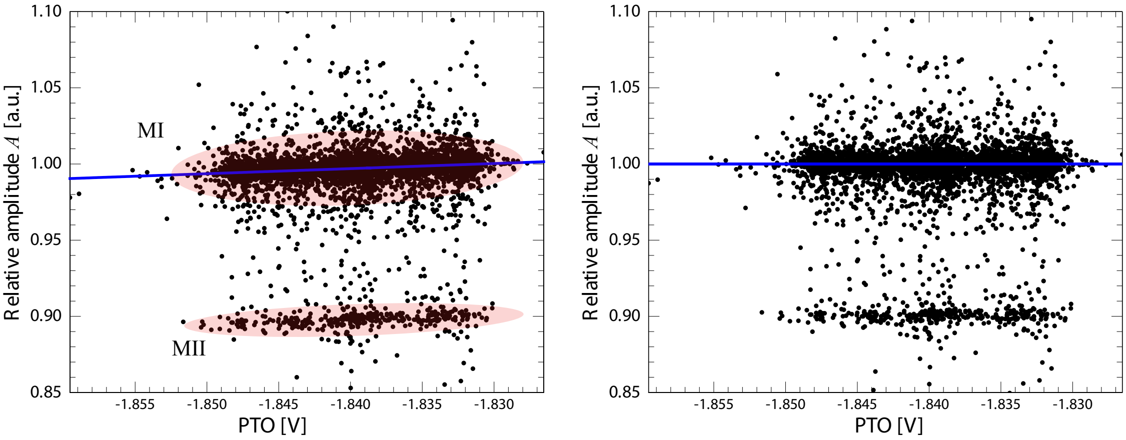

Figure 6.4: PTO versus the relative amplitude of single events. **(left)** Before the temperature correction. Marked in red are the signals belonging to the MI resonance line. **(right)** After the temperature correction.

detectors with their gradiometric pixel design are insensitive to global temperature changes. In reality small differences which evolve during the fabrication process of the detectors leave a very small sensitivity to the substrate temperature. This information can be recovered by the PTO-value which slightly drifts with a temperature change. This effect is independent of the change of working point of the read out SQUID. Since the PTO is already corrected for jumps it can be used to search for the temperature drift. In figure 6.4 **left** the PTO is plotted versus the relative amplitude of single events. A small change of bath temperature changes slightly the heat capacity of the detector and therefore the signal height changes as well slightly. This change can be followed by the PTO as seen in the here presented figure. For a specific resonance line, e.g. rel. amp. $= 1$ (MI) a slight slope can be seen. A linear fit of this region, taking only the signals belonging to the MI resonance line, is shown in blue. The linear fit function describing this slope

$$A(\mathrm{PTO}) = a \times \mathrm{PTO} + b \tag{6.1}$$

can be determined and used to divide the relative amplitude of every single event by this function dependent on the PTO-value measured for the event. This way a temperature drift can be corrected. The result can be seen in figure 6.4 **right**.

The last step of data treatment is the energy calibration. Up to this point only the relative amplitude of every single event was considered. The next step is to find the correlation between this amplitude and the actual input energy. One way to find this correlation is to use a source with a well know resonance energy. For MMCs optimized for energies up to 20 keV typically a ^{55}Fe-source is used which shows the x-ray resonance lines $\mathrm{K}_{\alpha,1}$ with energy of 5.898 keV, $\mathrm{K}_{\alpha,2}$ with an energy of 5.887

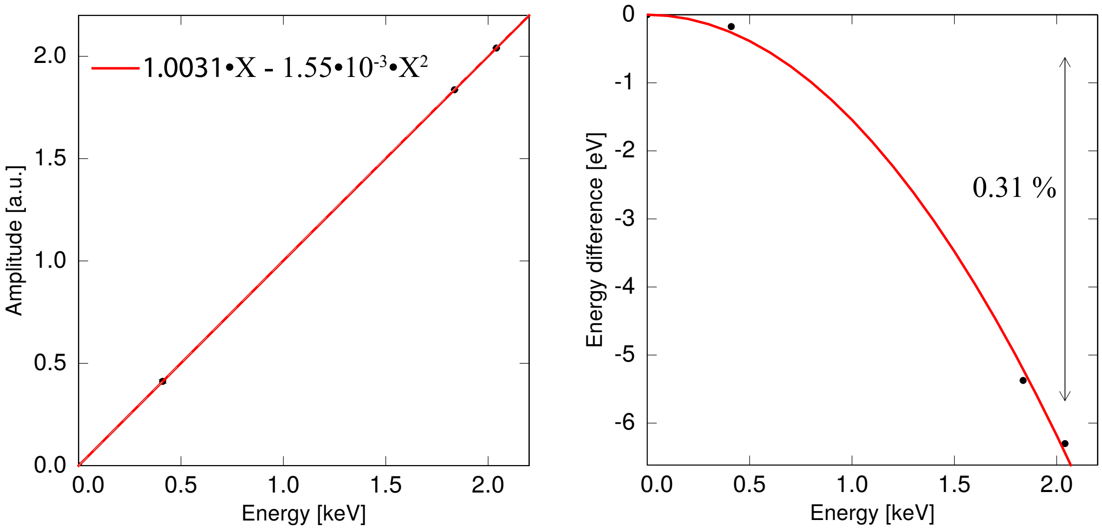

Figure 6.5: Detector linearity.**(left)** The resonance positions in the measured ^{163}Ho relative amplitude spectrum versus the in [Ran17] determine positions of the resonances in energy are shown. **(right)** The deviation to a linear correlation between these two peak positions is shown.

keV and K_β at 6.490 keV. An ^{55}Fe-source was used in a previous experiment to precisely determine the positions of the ^{163}Ho resonances [Ran17]. In that experiment the assumption was, that these resonances have in a first order approximation a symmetric line shape, which allows to determine the position of the peak by a fit of the data with a convolution of the Gaussian detector response and the Lorentzian line shape of the resonance. Due to this calibration for his and the following experiments the ^{163}Ho resonance lines can be used as calibration points. Of course has this calibration it's limits and needs to be improved by considering new descriptions of the theoretical ^{163}Ho spectrum and when a better energy resolution is achieved. For the following calibration of the energy spectra of ^{163}Ho it is more then sufficient. For the calibration a histogram of the relative amplitudes is generated. Then the MI, MII and NI resonance lines are identified. The MI line is fitted with a Voigt function[2] to determine the exact position of the peak. Then the position of the peak is scaled to the corresponding central energy of the MI line (2.040 keV). With this a first linear calibration is done. The non-linearity of the used detectors is very small, but nevertheless it can be corrected. In figure 6.5 **left** the in Ranitzsch et al. [Ran17] determined central energies of the ^{163}Ho resonances versus the central relative amplitude of the resonance peaks determined by a Gaussian are is plotted. The correlation is almost linear as expected. A small deviation from this behavior can be seen in figure 6.5 **right** with about 0.31 % at 2 keV. This deviation has a

---

[2] Voigt function as the convolution of the Gaussian detector response with the intrinsic Lorentzian line width of the resonance.

quadratic behavior which can be understood by the thermodynamic properties of the detector. As given by equation 3.2 the signal height is determined by the change of magnetization $\frac{\delta M}{\delta T}$ of the sensor material and the total heat capacity of the detector C_{tot}. These parameters are only slightly temperature dependent for the typical working conditions of an MMC as seen by the good linearity. Nevertheless, a small quadratic deviation is expected as described in [Bat16]. The correlation between an amplitude A and the input energy E is given for the presented data set in figure 6.5 by:

$$A(E) = 1.0031 \cdot E + 1.55 \cdot 10^3 \cdot E^2 \tag{6.2}$$

This function is determined for every single data set and then corrected for to get a linear correlation between input energy E and the relative amplitude A.

Afterwards some sanity checks are performed on the single data sets. The detector energy resolution ΔE_{FWHM} for the main resonances MI and NI are extracted by fitting again a Voigt function, where the width of the corresponding Gaussian detector response is left as a free fit parameter. This allows to identify data sets with a worsened energy resolution. These data sets can then be analyzed by hand and can be excluded from the main spectrum if necessary. A differing energy resolution can be caused by a slightly higher read out noise or by low statistics in a data set. When the data set does not allow to identify the resonances of the ^{163}Ho energy spectrum this can e.g. result in differing energy resolution values. For this data sets the energy resolutions cluster around $\Delta E_{\mathrm{FWHM}} = 9\,\mathrm{eV}$ for the NI resonance line. Here all data sets with an identical energy resolution of 9 eV within their fitting error are considered.

The background of the data sets is checked next. Therefore, the number of events in two energy intervals of the ^{163}Ho spectrum is determined. First from 2.9 keV, slightly above the expected Q_{EC}-value, to 5.8 keV. In this energy interval unresolved pile up events described in chapter 2.3.1 are expected. Here the distribution of these events over the data sets is checked. If one data set shows significant more events than other pixels the analysis steps are re-done and this is investigated further. A possible reason could be a different detector signal rise time due toa problem withthe read out chain or a damaged pixel. For this measurement there was no obvious deviation in this value for the data sets. The next interval is from 5.8 keV to 6.8 keV, which is defined by the maximal measured energy for this particular measurement. The upper limit of 6.8 keV for the energy interval is set by the maximal measured PTO-level of 2 V. The used ADC as a maximum Voltage acceptance of 2.5 V. So a pulse height of maximal 0.5 V is allowed before the signals start to get cut off. This signal height corresponds to an energy of 6.8 keV. In this energy interval no ^{163}Ho events and no pile up events are expected. So every event that survives the cut and calibration phase in this region is caused by an external background source, like cosmic muons, which are suppressed due to the 4800 m water equivalent above the detector, or natural radioactivity in the surrounding of the detector. Again, if a single data set shows a significant different value than the others, it can be further analyzed or even excluded. Another interesting value is the amplitude ratio of the MI and NI resonances. It should be same for all data sets and should be defined by theory at least on a few percent level. A possible deviation can be e.g. caused by an improper χ^2-cut, which cuts more events from one resonance then from the other one. At this point the small data sets are calibrated and checked in a way, that they can be added up to one energy spectrum.

6.3 ^{163}Ho energy spectrum

After all these checks the data sets are finally combined to the ^{163}Ho energy spectrum. Here the energy resolution of the single data sets can be kept. The summed spectra are then further analyzed. The final spectrum has 275 000 counts between $250\,eV$ and 6.8 keV and a detector energy resolution of $\Delta E_{\mathrm{FWHM}} = 9.0 \pm 0.4\,\mathrm{eV}$ at the NI resonance line was achieved as can be seen in figure 6.6. The value was extracted by the fit of a Voigt function. The resonance line NI is chosen since the theoretical line shape is clear with the present knowledge of theory. The error for the energy resolution is purely statistical. Systematic effects due to a not precise theory are not included.

6.3.1 Unresolved pile-up

As already explained in the energy interval between 2.9 keV and 5.8 keV the most prominent background should be due to unresolved pile up events. Here 1 count is found. To extract a pile up fraction for this number of counts an auto convolution of the measured spectrum is done. This pile up spectrum is then multiplied with a global scaling factor in a way, that the integral of the spectrum between 2.9 keV and 5.8 keV equals the number of measured counts in this interval. Then the unresolved pile-up fraction is given by the ratio of the two integrals for the full energy scale for the data and the scaled pile-up spectrum. The resulting pile-up fraction is $f_{\mathrm{pu}} = 3 \times 10^{-6}$, which is one order of magnitude away from the expected fraction of unresolved pile-up events $f_{\mathrm{pu}} = t \times a = 0.18 \times 10^{-6}$ with the measured activity a of 0.18 Bq and a rise time τ_r of 1 μs. Since here only one event was measured, this deviation might be explained by statistical fluctuations or the measured event is not an unresolved pile-up event. A comparison with the above ground measurement [Has16] with the same detector is not possible, due to the low acquired statistics of only 17500 counts in the spectrum. 0 events have been measured between 2.9 keV and 5.8 keV.

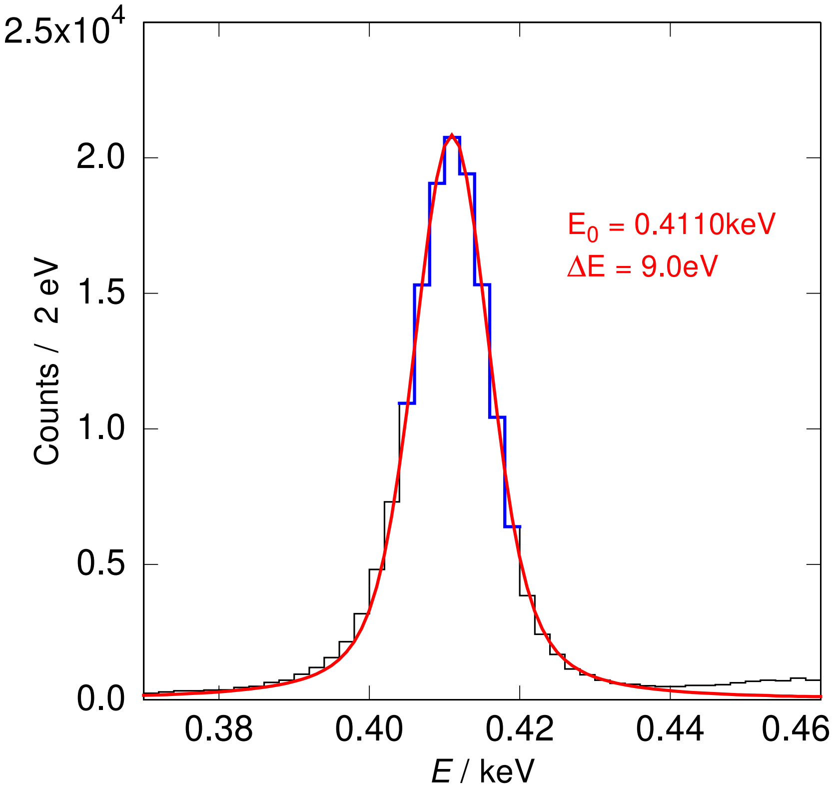

Figure 6.6: Measured NI resonance line of the full ^{163}Ho energy spectrum overlaid with a Voigt function fit, which allows to extract an energy resolution.

6.3.2 Background analysis

In this spectrum one count above 5.8 keV is present, which can not be explained by unresolved pile-up events. The count between 5.8 keV and 6.8 keV is a background event not induced by the ^{163}Ho decay itself. To calculate a background level the number of counts in a certain energy level is considered to have a flat probability distribution, meaning the probability for a certain energy for an event is the same for all energies. Since the event between 2.9 keV and 5.8 keV can also be caused by an external background, both events between 2.9 keV and 6.8 keV are considered for the deduced background level. Then an upper limit for a background level can be given by assuming a Poisson distribution of the events. For 2 counts between 2.9 keV and 6.8 keV a background level limit of below $BG < 2 \times 10^{-5}$ events/pixel/eV/day can be given. For the above ground measurement a background level with 0 counts between 2.9 keV and 6.8 keV in 24 h of $BG < 2 \times 10^{-4}$ events/pixel/eV/day can be deduced. At he present limit no statement about possible cosmic muon events in the detector can be made.

The measurement presented in chapter 7 with a comparable absorber size above ground has shown a background rate of about $BG < 1 \times 10^{-6}$ events/pixel/eV/day. Therefore, it can be stated, that at the present level of statistics no difference between the by rock shielded experiment and an experiment above ground can be found. Due to the small number of background events no finite answer for the need of a muon shielding or active muon veto can be given.

6.3.3 ^{163}Ho theory

This high statistic spectrum with a good energy resolution triggered improvements on the atomic description of the ^{163}Ho energy spectrum. Up to this point there have been attempts to describe the ^{163}Ho spectrum with various theories. Here to mention are the 2-hole excitation theory presented by A. Faessler et al. [Fae14] and the shake-off theory introduced by A. DeRujula et al. [DR15]. In the 2-hole theory not only the 7 resonance lines due to an electron capture from one of the allowed shells are present but during the capture process some energy can create a second hole in a shell by exciting another electron to an upper shell. The dysprosium can then reach its ground state by filling the two holes, which gives rise to new discrete peaks in the energy spectrum. This process is called a shake-up process. The expected amplitudes are quite small, since this process is less probable. In principle effects like 3-hole excitations are possible [Fae15], but the expected amplitudes are even smaller and do not play a role at the present statistics of data. This model was extended by A. DeRujula by introducing the shake-off process, were the electron from the second hole can not only be excited to a bound state, but into the continuum. This way the electron can take away kinetic energy which gives rise to continuous high energy tails to each 2-hole resonance peak. Both theories are shown in figure 6.7 and compared to the obtained data. Both theories are an improvement to the simple 7 resonance theory and the underlying atomic physics can explain additional sub structures, although the resonance intensities do not fit and the overall shape does not match the experimental data, for example in the "valley" between 0.6 keV and 1.6 keV.

A promising new theory are the *ab initio* calculations presented by M. Brass et al. [Bra18]. While in this work only excitations to bound states are considered, an extension of the model can in principle explain a few features present in the measured data as can be read in [Vel19a]. In figure 6.8 the experimental data is plotted and two fits, based on theoretic models are compared. The first fit in blue has the standard Lorentzian line shape as expected from scattering theory and used for the in figure 6.7 presented theory approaches. While the main resonance peaks are described very well, this line shape leads to small deviations above the NI resonance and the following "valley" between 0.6 keV and 1.6 keV. Small asymmetries in the line shape

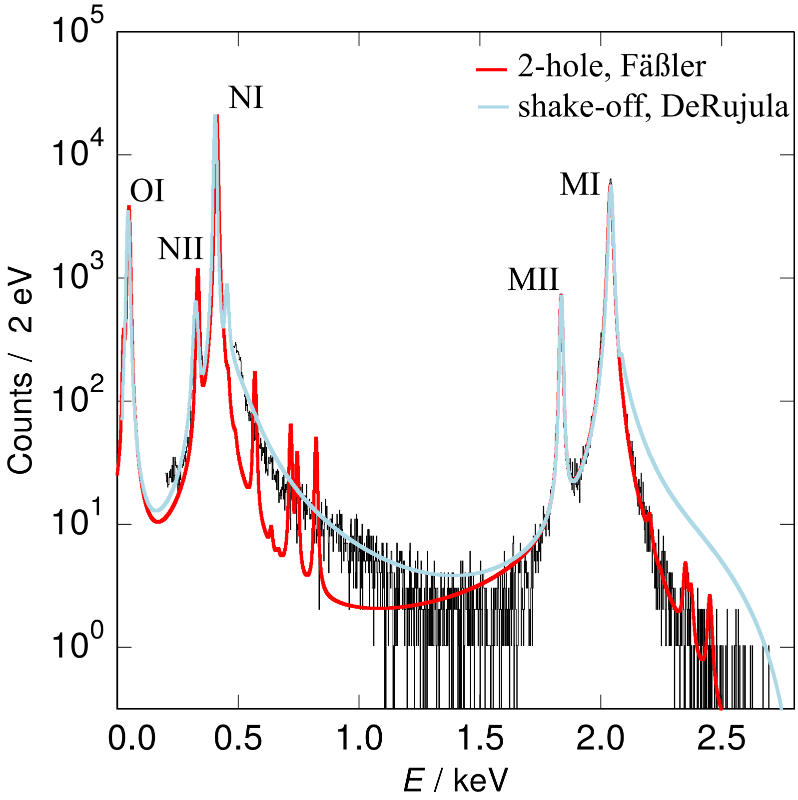

Figure 6.7: Measured ^{163}Ho energy spectrum, overlaid with the 2-hole theory of A. Fäßler and the shake-off theory by A. DeRujula.

are not covered. Furthermore, the theory seems to underestimate the spectral weight at the end point region.

Inspired by core level spectroscopy M. Haverkort introduced for the shake-off process an asymmetric Mahan line-shape broadening of the local atomic multiplets, which is used for Auger-Meitner decays. This asymmetric line shape allows to describe the experimental data even better, especially the "valley" and the sub structures above the NI line. In principle these sub structures are multiplets but the detector energy resolution of $\Delta E_{\mathrm{FWHM}} = 9\,\mathrm{eV}$ does not allow to resolve this feature. A small hint for such multiplets might be the low energy edge of the MI line, where a small kink can be seen. The full theory of ^{163}Ho is in development at the moment. The here presented theory does not contain all known important features to describe such energy spectrum and used several approximations which need to adapted to the case of ^{163}Ho .

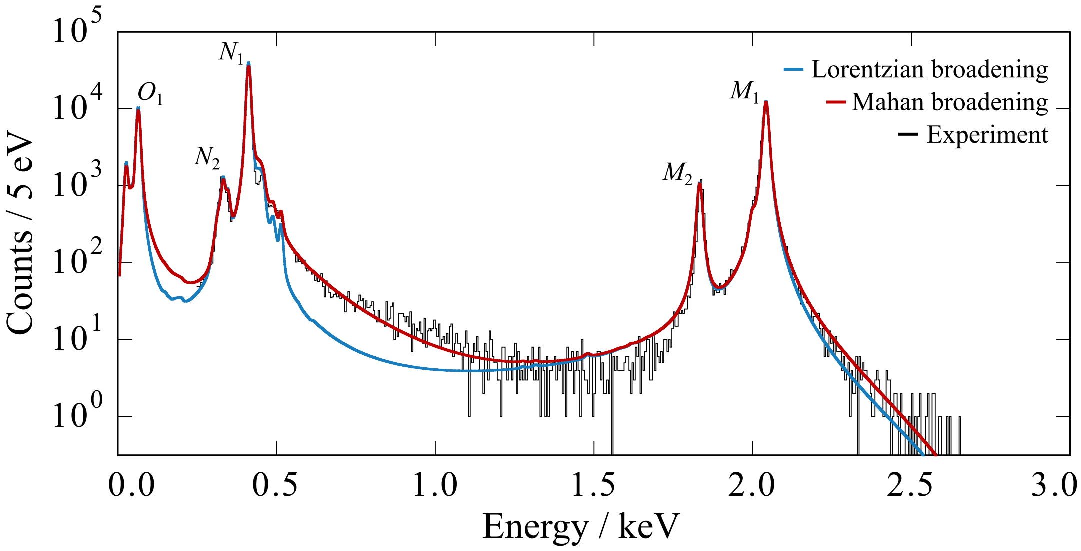

Figure 6.8: Measured ^{163}Ho energy spectrum, overlaid with a Lorentzian line-shape fit and a Mahan line-shape fit.

6.3.4 Q_{EC}-value

This new ^{163}Ho energy spectrum allowed a new calculation of the Q_{EC}-value performed by M. Brass [Vel19a]. Here $Q_{\mathrm{EC}} = 2.838 \pm 0.014\,\mathrm{keV}$ was calculated with a Bayesian parameter estimation. For the experimental and a *ab initio* theory for ^{163}Ho [Bra18] the spectral weight of the $3s$, $3p$ and $4s$ plus $4p$ resonances were determined. For this spectral weights a Gaussian likelihood and for the Q_{EC}-value a constant prior were assumed. The theoretical uncertainty is marginalized assuming a Jeffreys prior and the Gaussian variance is given by the statistical uncertainty. Note that the here calculated Q_{EC}-value is extracted from the spectral weight of the main resonances and is not dependent on the spectral shape of the end point region. This calculation is in good agreement with previous determinations of the Q_{EC}-value extracted from an MMC measurement of ^{163}Ho with $Q_{\mathrm{EC}} = 2.843 \pm 0.009^{\mathrm{stat}} \pm 0.060^{\mathrm{syst}}\,\mathrm{keV}$ [Ran17] and from a Penning trap mass spectrometry measurement with $Q_{\mathrm{EC}} = 2.833 \pm 0.030^{\mathrm{stat}} \pm 0.015^{\mathrm{syst}}\,\mathrm{keV}$ [Eli15].

6.3.5 Neutrino mass

The currently best upper limit from kinematic model independent measurements for effective the electron neutrino mass $m_{\nu_{\mathrm{e}}}$ is $m_{\nu_{\mathrm{e}}} < 225\,\mathrm{eV}$ is deduced from an x-ray spectrum of ^{163}Ho measured with Si(Li) detectors [Spr87]. This value can be slightly improved by a detailed analysis of the calorimetric ^{163}Ho energy spectrum we measured. To calculate a new upper limit on the effective electron neutrino mass a binned profile likelihood ratio analysis was performed [Bre19]. The likelihood ratio

LR for certain neutrino mass m_ν is given by:

$$LR_{m_\nu} = -2\,log\left(\frac{p(x|m_\nu,\alpha^{**}(m_\nu))}{p(x|m_\nu^*,\alpha^*(m_\nu))}\right) \tag{6.3}$$

Here $p(x|m_\nu,\alpha^{**}(m_\nu))$ is the likelihood function for a fixed m_ν and the best fit value for the nuisance parameters $\alpha^{**}(m_\nu)$, like the Q_{EC}-value or the energy resolution value where the fit is performed for a fixed m_ν. This value is divided by $p(x|m_\nu^*,\alpha^*(m_\nu))$ which is the likelihood value for the overall best fit with a varied m_ν and x is the measured data, i.g. the number of counts in each energy bin. The likelihood function $p(x|m_\nu,\alpha(m_\nu))$ is given by:

$$p(x|m_\nu,\alpha) = \prod_{\text{bins}\,i}\left(\frac{\mu_i(m_\nu,\alpha)^{x_i}e^{-\mu_i(m_\nu,\alpha)}}{x_i!}\right) \times p_{Nuisance}(\alpha) \tag{6.4}$$

$p_{Nuisance}$ describes the constraints on the nuisance parameters. For instance, it encodes that Q_{EC} was measured as $Q_{\text{EC}} = 2.838 \pm 0.014\,\text{keV}$. Equation 6.4 describes the number of counts in each bin as Poisson distribution. And the probability for a measured value x_i in bin i is calculated for a given expectation value μ_i, simulated for a given atomic theory, a certain neutrino mass m_ν and certain nuisance parameters α. To find the best fit values for α with and without a fixed m_ν to calculate LR for fixed m_ν steps 10^8 spectra are calculated, with a certain atomic theory prediction and the nuisance parameters, which are varied, assuming a Gaussian shape uncertainty on the parameters.

This whole LR analysis follows the idea to create a probability distribution for a certain test statistic $t_{measure}(\alpha)$ for a fixed neutrino mass m_ν and varying parameters α like depicted in figure 6.9 **(left)**. This test statistic $t_{measure}$ is as well calculated for the real experimental data set t_{data}, indicated by the blue vertical line. The result of the LR is now the area underneath the probability distribution to the right of t_{data} for every m_ν (dashed area) called p-value. If for a certain neutrino mass the p-value is smaller then 0.05, the value of the neutrino mass is excluded at 95 % C.L.. For large statistics this LR follows a χ^2 distribution.

The observed counts are analyzed in 62 bins, 60 of which are equal-sized bins spanning from 2.6 keV to 2.9 keV, complemented with an underflow bin from 0.1 keV to 2.6 keV and an overflow bin from 2.9 keV to 3.0 keV. As mentioned is the central value for each bin based on different ^{163}Ho theories. Used holmium models are the already presented ones: Mahan-Fit, enhanced Mahan-Fit, Lorentzian-Fit, 2-hole model, "ab initio" model and the simple 7 resonances model. These models are presented in figure 6.9 **(right)**. Note that here only the atomic physics is plotted without any phase space term. Depicted is the end point region, where the for the limit relevant bins are located. The enhanced Mahan fit is the normal Mahan fit, presented in [Vel19a] with a twice as high expected number of counts between 2.3 keV and 3 keV.

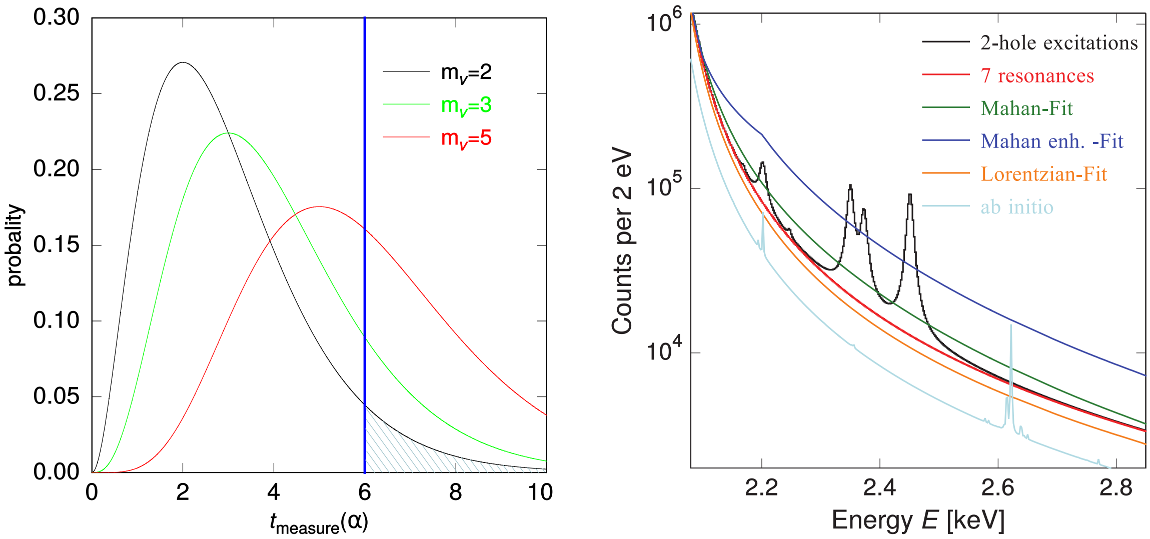

Figure 6.9: **(left)** Probability distribution for a test statistic $t_{measure}(\alpha)$. **(right)** Depicted are several ^{163}Ho theories, describing only the atomic physics of the spectrum. The phase space term is excluded.

The dominant systematic uncertainties on these predictions are modeled with the following nuisance parameters. Taken where $Q_{\text{EC}} = 2.838 \pm 0.014\,\text{keV}$ and the measured unresolved pileup fraction with $f_{\text{pu}} = 1 \times 10^{-6} \pm 0.5 \times 10^{-6}$. This Q_{EC}-value was taken, since it provides the smallest uncertainty and was extracted independent of the here relevant end point region. A Gaussian shape of the uncertainty was assumed. For the pile up fraction a distribution corresponding to the auto-convolution of the measured spectrum was assumed. The measured background is included as well with $BG < 2 \times 10^{-5}$ events/pixel/eV/day. For the BG no uncertainty was assumed, since the variation did not influence the results on the presented level. We simultaneously fit the electron neutrino mass and the nuisance parameters to the observed bin counts using the pyhf library [Hei19]. We then calculate confidence limits on the neutrino mass based on the profile log likelihood ratio as test statistics, using the asymptotic approximation in the analysis [Cow11].

The results are shown in figure 6.10. Here the inserted neutrino mass is plotted versus the calculated p-value for different input theories. The upper limit for m_ν 95% C.L. for each theory can be found in table 6.1. As can be seen the results differ on a 9 eV level. The results do not differ significantly since the error on the Q_{EC}-value is that large, that any difference in slope due to theory can also be achieved by a change of the Q_{EC}-value. For a smaller error the obtained results would differ more. In principle the uncertainty on the theory can be included in this hypothesis test. For the Combined-value in table 6.1 the Mahan-Fit theory (figure 6.9 **(right)** green) was taken as central prediction. As lower bound the Lorentzian-Fit was taken (figure 6.9 **(right)** orange) and as upper limit the enhanced Mahan-Fit (figure 6.9

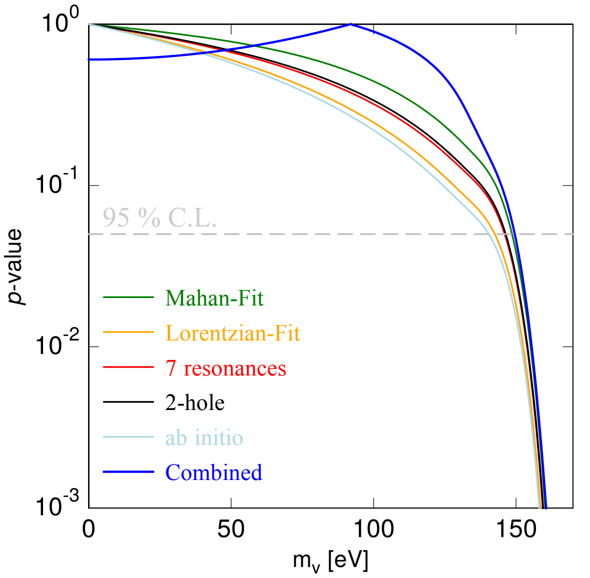

Figure 6.10: For different m_ν the calculated p-value is shown. Where this value crosses 0.05 a 95 % C.L. exclusion limit for this mass is reached.

Theory	m_ν-limit 95 % C.L. [eV]
Mahan-Fit	149
Lorentzian-Fit	143
7 resonances	147
2-hole excitations	147
ab initio	141
Combined	150

Table 6.1: m_ν-limit 95 % C.L. [eV] for different input theories.

(right) blue) was introduced. Here a Gaussian shaped uncertainty was assumed as well. The large upper bound on the theory prediction now allows for an excellent fit with slightly larger neutrino masses. In fact, the best-fit point of this combined analysis is at $m_\nu = 100\,\text{eV}$, though this is not statistically significant. At neutrino masses above around 140 eV, however, the variability in the combined atomic model cannot longer compensate for the dramatic effects of the neutrino mass, and the limits become similar to those of the individual atomic theories."

7. Experimental Results: ECHo-1K

In this chapter the first high statistics and high energy resoltution ^{163}Ho spectrum acquired for the ECHo-1k phase is presented. For this measurement 23 pixels of an ECHo-1k detector chip were operated at $T \approx 10\,\mathrm{mK}$ for 22 days. In total about 3×10^7 single ^{163}Ho events have been recorded. The energy resolution of the final spectrum was $\Delta E_{\mathrm{FWHM}} = 6.6\,\mathrm{eV}$ at the NI resonance line and $\Delta E_{\mathrm{FWHM}} = 6.7\,\mathrm{eV}$ at the MI resonance line. Therefore, this ^{163}Ho energy spectrum allows to investigate for the first time the full shape of the "valley" in the energy spectrum of ^{163}Ho between the NI-line (0.4 keV) and the MII-line (1.8 keV) and allows to look for the expected multiplet structures predicted by the *ab initio* calculations [Bra18] introduced in chapter 6. In general this data allows to test any given ^{163}Ho theory with more features than before.

7.1 Set up: ECHo-1K

The measurement was performed in a lab at the Kirchhoff-Institute for Physics, Heidelberg in a dry dilution refrigerator. The ^{163}Ho was implanted in the pixels of the ECHo-1k detector at the RISIKO facility, Mainz University [Kie19]. For this implantation a fraction of the chemically purified ^{163}Ho source was used [Dor18]. The planned activity was about 1 Bq. This is the exactly same detector chip as it was used for the heat capacity measurements presented in chapter 5. The readout chain was changed slightly, in particular in terms of noise. The better noise performance was achieved with the change of the front end SQUIDs and the array SQUIDs.

7.2 Activity

The measured activity varies from 0.3 Bq to 1.5 Bq as can be seen in the activity map in figure 7.1. The average activity was 0.9 Bq and is therefore quite close to the expected activity of 1 Bq. For every pixel, the activity is determined as explained in 6. The data files to calculate the activity were obtained over 24 hours. The pixels left without ^{163}Ho during the implantation are marked in violet and allow the in-situ background measurements. For this experiment only one of the 3 working BG detectors was connected. Furthermore, not all here presented detector channels were measured during this specific measurement. Marked with light blue is the detector channel for the heat capacity measurements presented in 6. Marked with pale red

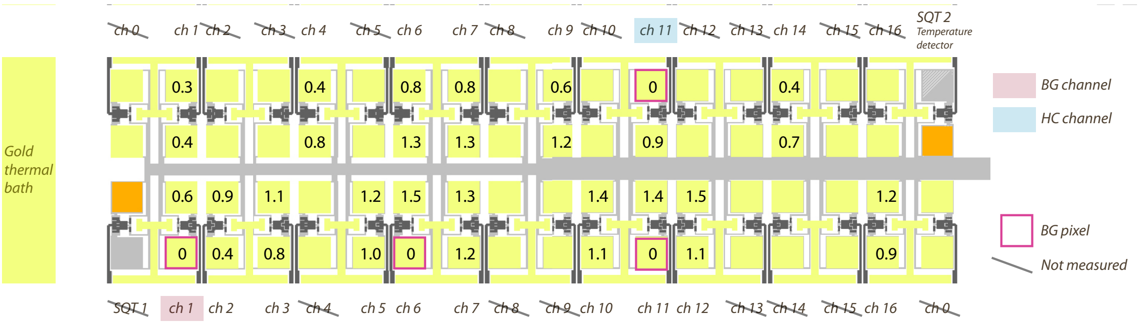

Figure 7.1: Activity map of the ECHo-1k detector chip. The numbers in the single pixels correspond to the measured activity in Bq. If no number is given, these pixels have not been measured.

is the background channel, which was operated for this measurement. The SQT 2 channel in the top right corner of figure 7.1 is the temperature channel, already used for the magnetization measurement presented in chapter 5.4.

During the implantation process the ion beam with a diameter of about 0.7 mm scans about 2000 times the two detector rows, each with a width of about 0.4 mm. The deviation in activity is not fully understood, although a gradient from the middle of the rows to the edges and from left to right can be observed, which might be explained by a small miss alignment during the implantation process, deviations of 50 % between neighboring pixels can not be explained this way and is still under investigation.

7.3 Data reduction

To obtain the full ^{163}Ho spectrum, the same analysis steps as described in 6 were performed. Due to the long measurement time many PTO jumps caused by jumps to a different working point of the read out SQUID were present. Furthermore, certain improvements in terms of noise during the measurement period were made. Both lead to 267 sub-files that had to be added. For the analysis of the acquired data, an improved temperature correction was used. The correlation between the PTO and the detector temperature relies on small deviations of the two pixels in the gradiometric set up. In this measurement the on chip temperature pixel was recorded during the full time. For each triggered signal in each detector channel, together with the other analysis parameters, also the average voltage of the temperature channel was recorded. This way a better temperature correction was possible. This temperature detector is the same one as used for the magnetization measurements described in chapter 5.4.

In order to decide if the preparation of one pixel satisfies the requirements for adding the data to the final spectrum several sanity checks are performed. For each file the energy resolution at the NI and MI resonance line, the spectral weight ratio of MI/NI, the mean distance from the linearity correction, the number of BG events between 2.9 keV and 5.8 keV and the number of BG events between 5.8 keV and 10 keV are determined. In total 267 files have been analyzed. The sanity check statistic for these files is presented in figure 7.2. In figure 7.2 **a)** and **b)** the calculated detector energy resolutions for the MI line and the NI line are shown. These values are obtained as explained in chapter 6 by a Voigt fit with the width of the convoluted Gaussian as free parameter. The parameters of the resoance lines are taken from [Ran17]. Marked in red in figure 7.2 **a)** and **b)** are outliers, which have not been included in the final spectrum. These files either belong to very small data sub sets, or to one specific channel with a periodically high noise level, caused by an external noise source, which was only seen by this specific channel. In figure 7.2 **b)** some data sets show very large distribution of energy resolutions for the MI line, which can be explained lower statistics and a larger intrinsic line width of the MI resonance line.

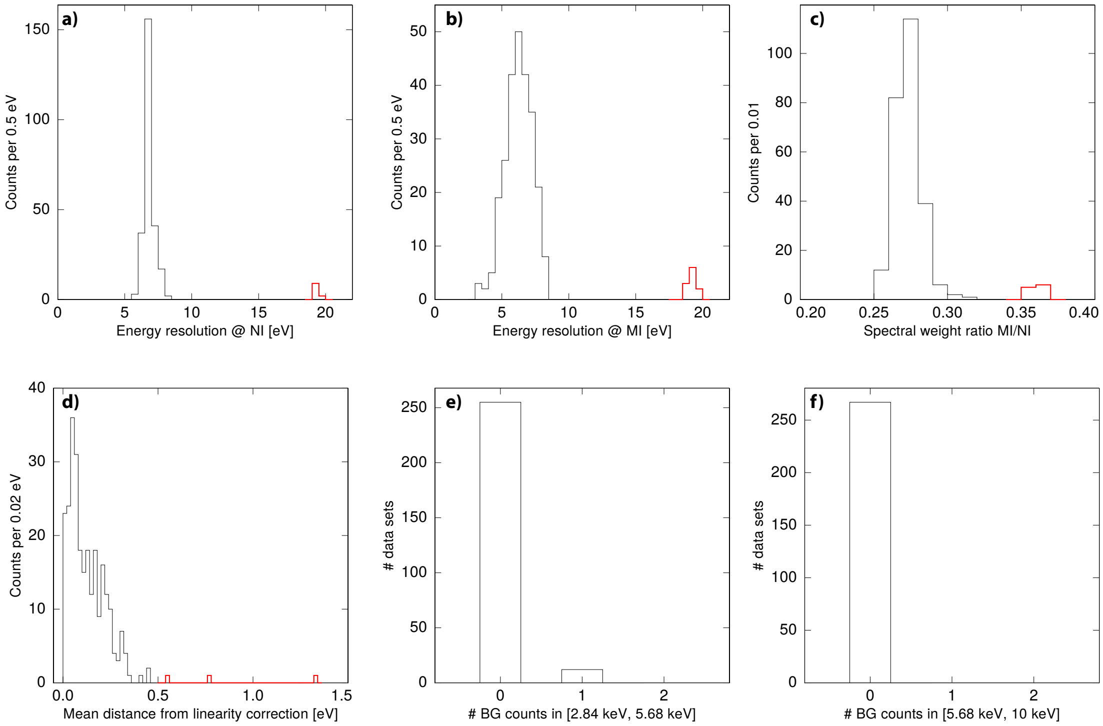

Figure 7.2: Shown are calculated parameters for each of the 267 data sets, which allow to identify automatically data sets, which need to be looked at separately.

In figure 7.2 **c)** the ratio of the spectral weights of the MI and NI resonance lines is shown. This ratio depends on the capture probability for 3s and 4s electrons and on the Q_{EC}-value. For $Q_{\mathrm{EC}} = 2.822\,\mathrm{keV}$, the simple 7 resonances theory from Fäßler and $m_\nu = 0$ this ratio is expected to be around 0.3. Once the spectral weight of these peaks is given by a theory, that describes the ^{163}Ho energy spectrum very well and the Q_{EC}-value is given with a higher precision the absolute value can be taken as measure. In principle could the applied constant χ^2-cut change this ratio, if e.g. the spread in χ^2 is significant larger for lower energies. This would exclude a larger fraction of counts from the NI line than from the MI line. Therefore, the amplitude ratio MI/NI would change. As can be seen, the data sets marked with red for this parameter, show a slightly shifted MI/NI-ratio. In fact these are the same data sets, that already showed a larger energy resolution in the MI line. Here again the low number of events in the data sets can lead to a failure of the χ^2-cut. Here the mean of the χ^2 distribution can be determined incorrect due to the low number of counts. The result is a χ^2-cut that changes the ratio of MI/NI. Such data sets are analyzed again by hand to check the applied data treatments. If e.g. no clear clustering in the χ^2-plot can be found these files are excluded.

As described in chapter 6 a linearity correction is performed for each data set. The residuals of the fit of the energy position of the main peaks are quadratically summed and the square root is calculated. The result for the data sets can be seen in figure 7.2 **d)**. Here again data sets with a deviation to the majority of data sets are checked again and the performed analysis steps are reviewed.

Finally, the two background regions already introduced in chapter 6 are checked. In the low energy background region (7.2 **e)**) unresolved pile-up events can occur. For this long measurement 12 events in this energy region where measured. These 12 events are distributed over 12 detector pixels with long time periods in between the events, which minimizes the chance for an extended BG problem with the pixels or read out chains.

The expected unresolved pile-up fraction f_{upu} with an average pixel activity a of 0.9 Bq and a signal rise time τ_{r} of about 1 μs is $f_{\mathrm{upu}} \approx 10^{-6}$. For the next ECHo phases the rise time needs to be improved to reduce the expected pile-up fraction. The corresponding *UPU* spectrum is an auto convolution of the measured ^{163}Ho energy spectrum as shown in figure 7.3 in red for one data set. In this one data set 1 *UPU* event is present. Here the spectral weight is $10^{-6}\times$ the spectral weight of the one data set ^{163}Ho energy spectrum with about 3.3 mio. counts. The expected number of counts for *UPU* events is between 2.9 keV and 5.8 keV about 0.4, deduced from the activity a of the detector pixels and the rise time τ_{r} of the detector signals. The 1 measured *UPU* event and the expected 0.3 *UPU* events might be in good agreement, considering the poor statistics in this energy region and the fact, that maybe not all events are *UPU* events. A way better analysis can be performed, once the spectral shape of the *UPU*-spectrum can be recognized and a pulse shape analysis is established that allows discriminating *UPU* events from real events.

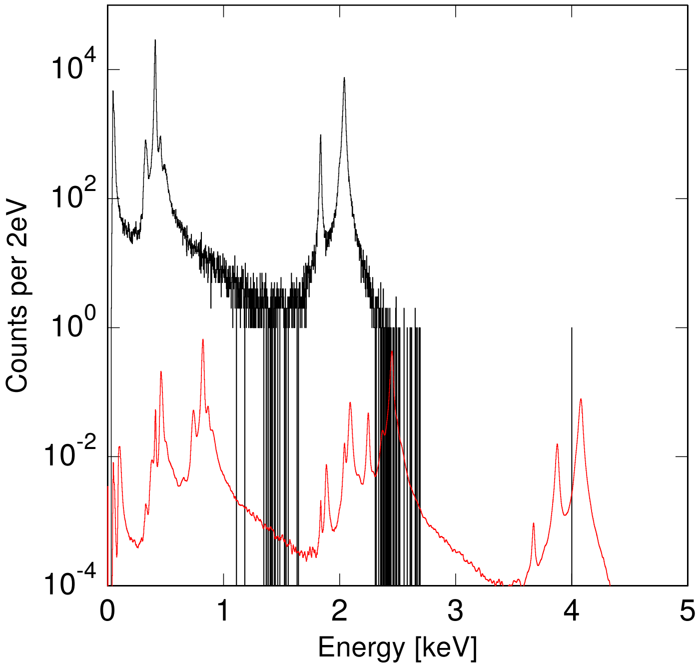

Figure 7.3: Shown is the measured ^{163}Ho energy spectrum (black) of one data set and the corresponding expected UPU-spectrum (red).

In the last plot, figure 7.2 **f)** the BG is shown in the energy interval between 5.8 keV and 10 keV. For this experiment no event was measured, which leads to an background level of $BG < 1 \times 10^{-6}$ counts/eV/pixel/day with the in chapter 6 described method assuming a flat distribution for the background events. Since here no events have been measured it is even more probable that the measured events in the energy region between 2.9 keV and 5.8 keV belong to unresolved pile-up events.

7.4 Spectral shape of ^{163}Ho

The full spectrum was obtained by the measurement of 23 pixels of an ECHo-1k detector chip for 22 days operated at $T \approx 10\,\mathrm{mK}$. This data was divided in 267 sub -files and added up coherently. The final spectrum has 2.7×10^7 counts.

The achieved overall energy resolution was $\Delta E_{\mathrm{FWHM}} = 6.6\,\mathrm{eV}$ at the NI resonance line and $\Delta E_{\mathrm{FWHM}} = 6.7\,\mathrm{eV}$ at the MI resonance line as can be seen in figure 7.4. Both values agree with each other within the statistical error of the calculation for the energy resolution. As already mentioned in chapter 5, these energy resolutions are not the intrinsic detector resolutions, which should be more around $\Delta E_{\mathrm{FWHM}} = 3\,\mathrm{eV}$ as described in chapter 4.2. The limiting factor here are the corrections of changes in temperature and gain during the measurement, which can be done only to a certain

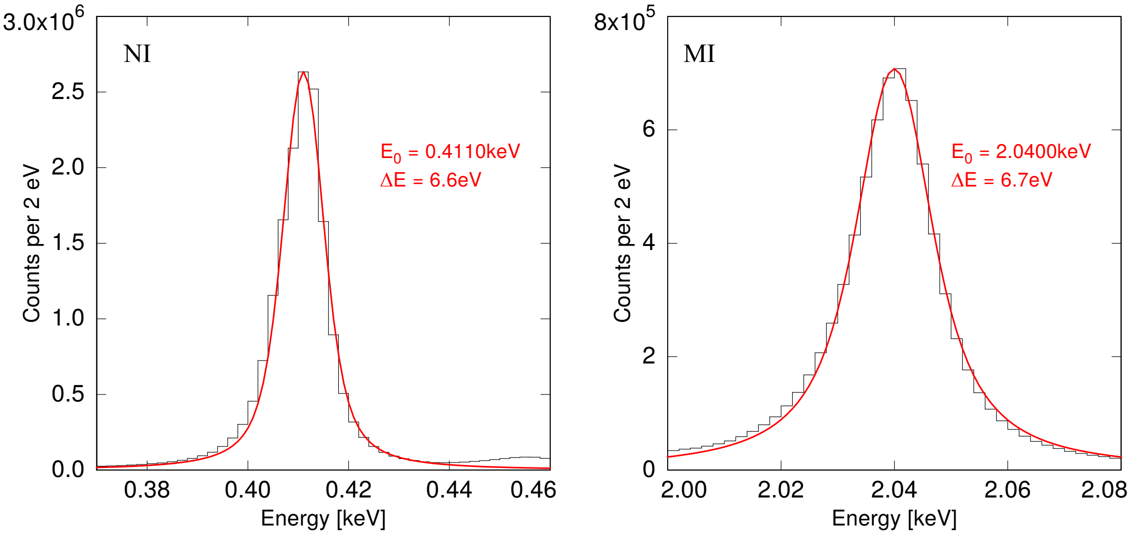

Figure 7.4: Energy resolution obtained for the NI resonance and MI resonance. The red curve is the fit result of the Voigt function, used to extract the energy resolution.

extent. A stabilization of both parameters, which is foreseen for the next ECHo experiments, will bring an energy resolution close to $E_{\mathrm{FWHM}} = 3\,\mathrm{eV}$. In figure 7.5 the complete obtained ^{163}Ho energy spectrum is shown. This spectrum with its 3×10^7 counts, an energy resolution of $\Delta E_{\mathrm{FWHM}} = 7\,\mathrm{eV}$ and no specific external background source noticeable on the presented level allows for a detailed comparison with any theoretical description of the ^{163}Ho energy spectrum. As can be seen 12 events in total are present in the unresolved pile-up region between 2.9 keV and 5.8 keV. This results in a measured unresolved pile-up fraction of $f_{\mathrm{upu}} \approx 4 \times 10^{-6}$. Expected with the given activity per pixel and the detector rise time are 3 events in this energy region. The corresponding to this value scaled unresolved pile-up spectrum is shown in red in figure 7.6 **(right)**. As already explained above a better analysis can be performed, once the spectral shape of the UPU-spectrum can be recognized and a pulse shape analysis is established that allows discriminating UPU events from real events.

In figure 7.6 **(left)**, the measured data is overlaid with the *ab initio* theory presented in [Bra18]. Although clear differences in spectral weight in the valley between 0.6 keV and 1.6 keV are visible, as well as at the end point region, this theory predicts already some small features, which got visible within this measurement. The spectral shape will change in this energy regions once excitations to the continuum are implemented in the theory calculations. This theory only allows excitations to bound states at the moment.

Small features, already seen in the data presented in chapter 6 are now clearly visible like the multiplet structure of the MI resonance line, predicted by the *ab initio* theory,

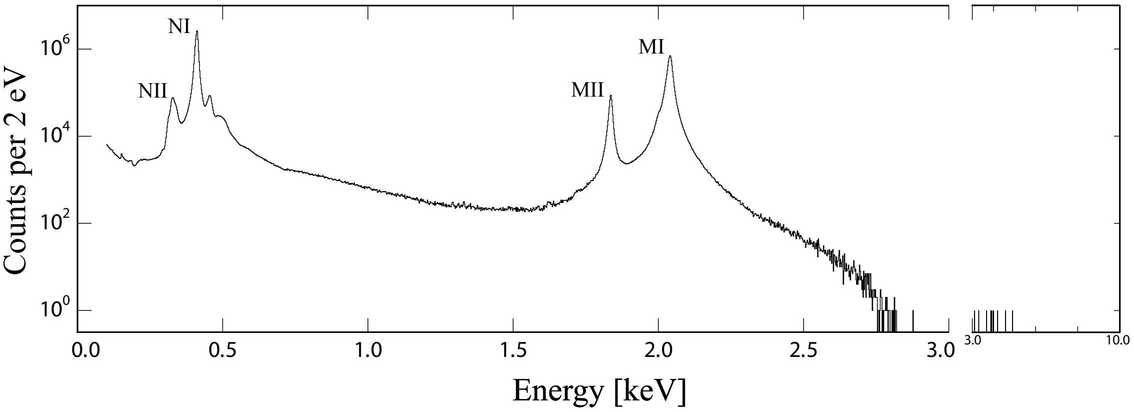

Figure 7.5: Full ^{163}Ho energy spectrum, 3×10^7 counts, $\Delta E_{\mathrm{FWHM}} = 7\,\mathrm{eV}$.

visible as a shoulder on the low energy side as can be seen in figure 7.7 **(right)**. But also the multiplet structure of the NII resonance line shown in figure 7.7 **(left)** is visible and the spectral shape of the peak above the NI resonance line can now be investigated further.

Details like the small "up" and "down" in the valley around 250 eV are similar predicted in [Bra18], as a result of interference between the electron wave functions during the capturing process. Other features like the very broad continuous structure from 700 eV to 1.6 keV or the broad structure from 2.4 keV to 2.8 keV still need to be investigated. This data delivers for sure enough input for the next theoretical descriptions of ^{163}Ho , brought forward by M. Haverkort.

7.4.1 In-situ background measurement

The background (BG) level was determined with $BG < 1 \times 10^{-6}$ counts/eV/pixel/day taking into account the measured 0 events between 5.8 keV and 10 keV. Here the same assumptions were made as in chapter 6. Furthermore, an in-situ background measurement was performed. For this measurement an asymmetric pixel pair was measured, marked with red in figure 7.1. This channel is 1 out of 7 in-situ background detectors, which have one pixel implanted wit ^{163}Ho and one without. Every triggered event in the pixel without ^{163}Ho implanted is treated as external background event. This way external background sources can be measured for energies between 12 eV and 10 keV. To extract an energy calibrated background spectrum, the template signal for the fit for this BG pixel is taken from the neighboring pixel with ^{163}Ho implanted. This allows for an energy calibration, which should not be off more then 2%, which is the typical variation of the signal height coming from the two double meanders for the same energy input. Furthermore, the 5σ χ^2-cut from the pixel belonging to the same double meander is taken and applied to the

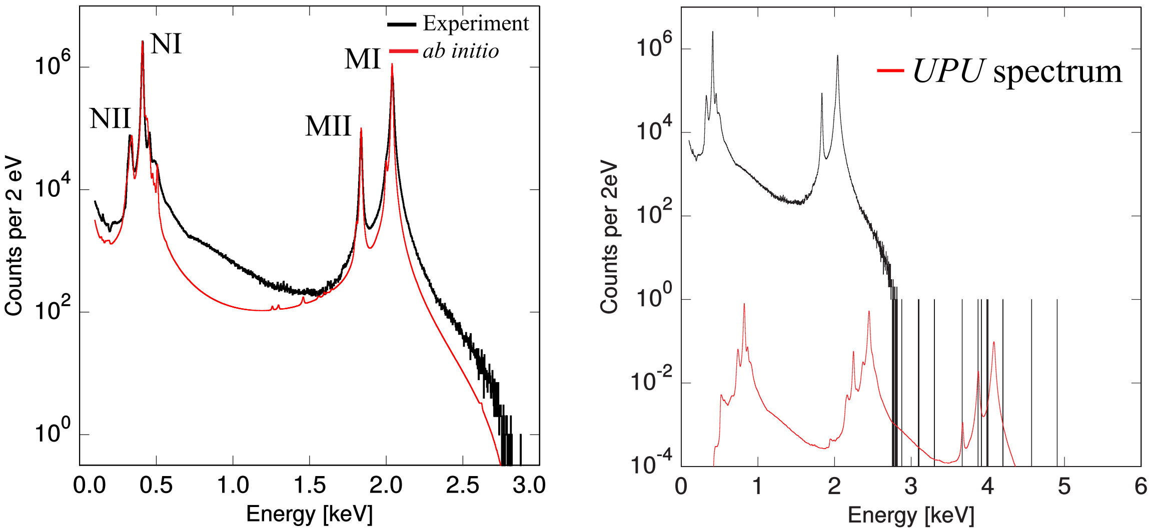

Figure 7.6: **(left)** Full ^{163}Ho energy spectrum, 3×10^7 counts, $\Delta E_{\mathrm{FWHM}} = 7\,\mathrm{eV}$. In red is the *ab initio* theory overlaid. **(right)** Full ^{163}Ho energy spectrum overlaid with the expected unresolved pile-up spectrum in red.

BG pixel. This way the remaining energy spectrum in the BG pixel should be very similar to a BG spectrum, that can be expected on a pixel with ^{163}Ho due to external background sources. The BG spectrum is shown in figure 7.8 **(left)**. As can be seen, the BG shape follows an exponential decay, while most of the counts are present below 1 keV. Between 1 keV and 10 keV only 2 more counts are present. The exponential decay was expected, since the trigger level of this pixel was chosen to be very low to record also signals with a low energy. The set trigger level corresponds to the minimal recorded energy of 12 eV. Due to the small signal size towards low energies and the relative high noise, no effective pulse shape discrimination can be performed anymore with the applied χ^2-method. At about 20/,eV a prominent peak in the BG spectrum can be seen. This peak is caused by two very discrete background sources. One background signal are rectangular signals with exactly the same height, distributed over the whole measurement period. They were probably caused by cell phones, searching for the radio network. The other signal are high frequency peaks, triggered as well and distributed over the whole measurement period. Both signals are not sorted out by the χ^2-cut due to the bad S/N. This exponential decay defines the threshold of the here presented ^{163}Ho spectra. All of the here presented spectra have this exponential decaying BG and in principle also the peak at about 20/,eV. That is why the threshold of the here presented spectra was chosen to be 100/,eV. This way the BG peak is for sure excluded and the BG contribution to the ^{163}Ho spectrum is minimal.

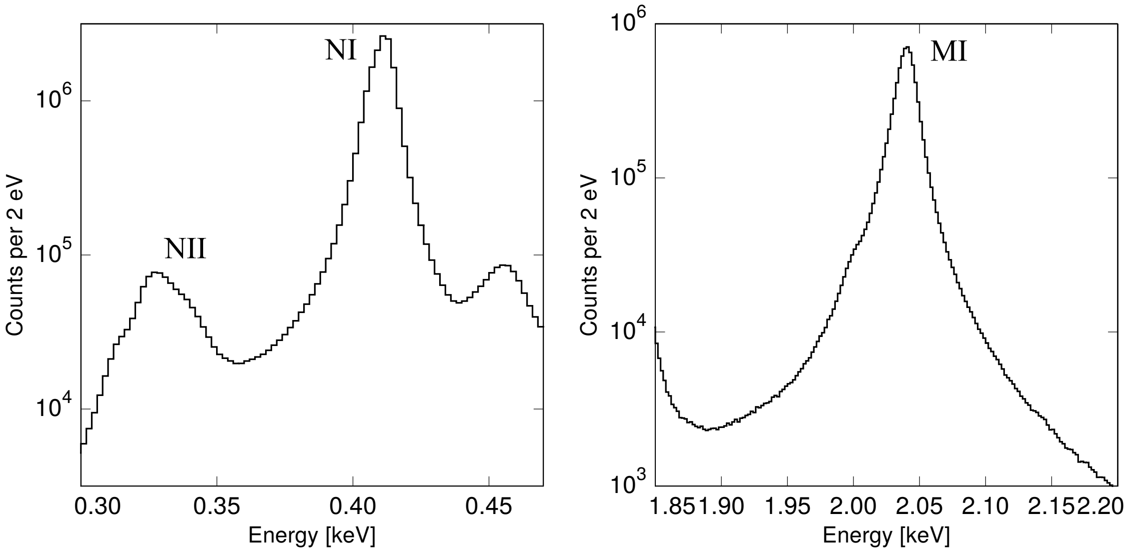

Figure 7.7: The NI and MI resonance lines of the measured ^{163}Ho energy spectrum with 3×10^7 counts and $\Delta E_{\mathrm{FWHM}} = 7\,\mathrm{eV}$.

7.4.2 Q_{EC}-value determination

For the full data set with about 30 mio. counts a fit of the Q_{EC}-value was performed by M. Brass following the same method explained in chapter 6 and in [Vel19a]. The result is $Q_{\mathrm{EC}} = 2.842 \pm 0.016\,\mathrm{keV}$, which is in very good agreement with all previous mentioned measurements. The calculated error is almost the same since the error introduced by the systematic uncertainties related to the spectral shape are the same. Small deviations are probably due to statistical fluctuations.

Another method to extract the Q_{EC}-value from this data is presented in the following. The idea is that the shape of the ^{163}Ho spectrum is defined by a phase space term PS and some term $A(E)$ that is defined by atomic physics.

$$\frac{dW}{dE} = (Q_{\mathrm{EC}} - E)^2 \sqrt{1 - \frac{m_\nu^2}{(Q_{\mathrm{EC}} - E)^2}} \times A(E) \tag{7.1}$$

The neutrino mass m_ν is in good approximation $m_\nu = 0$, since almost all recent measurements predict a limit for m_ν of below 1 eV. This small m_ν does not influence the shape of the measured spectrum significant with the given statistics.

This reduces the description of the spectral shape to:

$$\frac{dW}{dE} = (Q_{\mathrm{EC}} - E)^2 \times A(E) \tag{7.2}$$

$$\tag{7.3}$$

Furthermore, should be the influence of the not perfect atomic theory $A(E)$ be minimal in the last 100 eV close to the endpoint, since here no noticeable additional

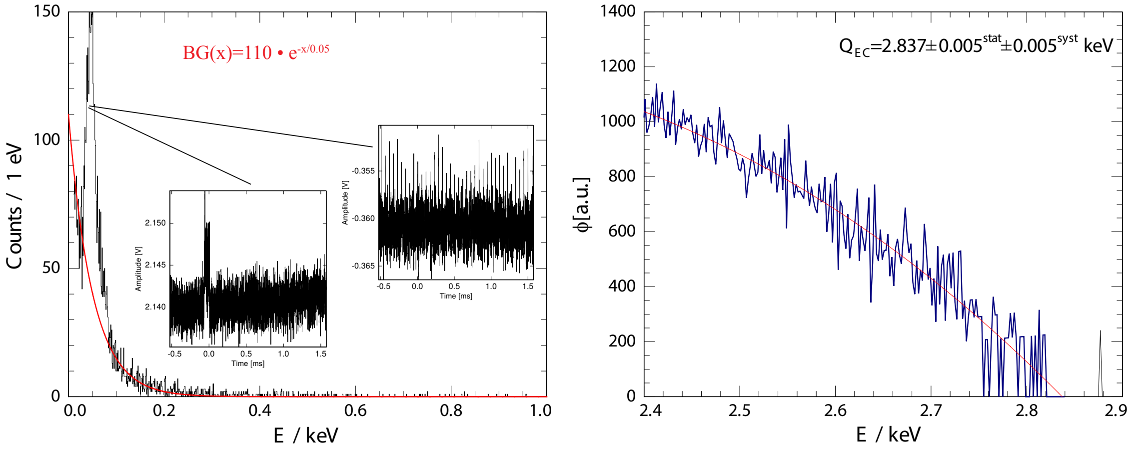

Figure 7.8: (left) BG spectrum, obtained from a pixel without ^{163}Ho implanted and calibrated with the neighboring pixel with ^{163}Ho of the gradiometric set up. **(right)** Kurie plot of the end pointregion of the ^{163}Ho energy spectrum. In red is the fit, where the Q_{EC}-value is extracted from. In blue is the data taken for the fit.

peaks from higher order processes in the electron capture spectrum are expected at the current level of measured statistics.

To fit the Q_{EC}-value to the end point region, the whole measured spectrum $MS(E)$ is divided by the atomic theory $A(E)$ given by M. Brass [Bra18]. The square root of the left overs $\phi(E)$ are plotted in figure 7.8 **(right)**.

$$\phi(E) = \sqrt{\frac{MS(E)}{A(E)}} \tag{7.4}$$

This kind of data presentation is a Kurie plot, defined for β-decay spectra. The slope of $\phi(E)$ should be given by $(Q_{\mathrm{EC}} - E)$, which allows to extract the Q_{EC}-value with a linear fit. As can be seen in figure 7.8 **(right)** the curve does not follow a purely linear behavior, which can be explained by a not perfect theory in this energy regime. In fact a broad structure from 2.4 keV to 2.8 keV is observed. This small discrepancy in theory is modeled by a polynomial. In red is the fit of $(Q_{\mathrm{EC}} - E)$ times a polynomial of second order.

$$\phi(E) = (Q_{\mathrm{EC}} - E) \times (aE + bE^2) \tag{7.5}$$

With $a = -399$ and $b = 578$ the result is $Q = 2.837 \pm 0.005^{stat} \pm 0.005^{syst}$ keV. While the statistical error is given by the fit, the systematic error is given by the variation of the energy interval the fit is performed on, here marked with the blue line. The count at 2.878 keV is explicitly excluded, since it is most probably an unresolved pile up event. Higher order polynomials and neutrino masses up to 5 eV do not change the result on the presented level. The fit was stable and the statistical

Theory	m_ν-limit 95 % C.L. [eV]
Mahan-Fit [Vel19a]	47
Lorentzian-Fit [Vel19a]	48
7 resonances [Fae14]	47
2-hole excitations [Fae15]	48
ab initio [Bra18]	47
Combined	50

Table 7.1: m_ν-limit 95 % C.L. [eV] for different input theories.

errors on the factors of the polynomial where comparable small. This way the most precise determination of the Q_{EC}-value was achieved in good agreement with all other presented measurements.

7.4.3 Neutrino mass: ECHo-1k

The acquired data with about 30 mio. counts and an energy resolution of $\Delta E_{\mathrm{FWHM}} = 6.7\,\mathrm{eV}$ at the MI resonance line can be used for setting a new limit on the effective electron neutrino mass m_v. Within this thesis an approach based on binned profile likelihood ratio analysis was developed as described in chapter 6.

The first overflow bin was now from 0.25 keV to 2.6 keV, since here way more counts in the end point region were present. The Q_{EC}-value was kept the same as in the previous calculation with $Q_{\mathrm{EC}} = 2.838 \pm 0.014\,\mathrm{keV}$, since it was determined independently of this measurement and not taking into account the end point region of the spectrum. The unresolved pile-up fraction was adapted according to the here presented measured level of $f_{\mathrm{upu}} \approx 4 \times 10^{-6}$, the error was kept at 50 %. The background was modeled by the in the previous sections presented results. A flat background distribution with $BG = 1 \times 10^{-6}$ counts/eV/pixel/day plus the determined exponential decay are assumed and scaled to the measured values. Again no error on the background model was assumed due to the negligible influence on the here presented results. Taking the same theories as described in 6, the results presented in table 7.1 are obtained. The corresponding p-values for different neutrino masses are shown in figure 7.9 **(left)**. Again only small deviations for the different input theories are seen. This is still to the fact that at this level of statistics, energy resolution and uncertainties on the unresolved pile-up fraction and the Q_{EC}-value, the limit on the neutrino mass is basically given by the difference between the last measured count in the energy spectrum and the Q_{EC}-value, not by the actual spectral shape of the theory. The probability, that the last count in the ^{163}Ho energy spectrum is really due to a decay of ^{163}Ho , and not due to a background event is here together with

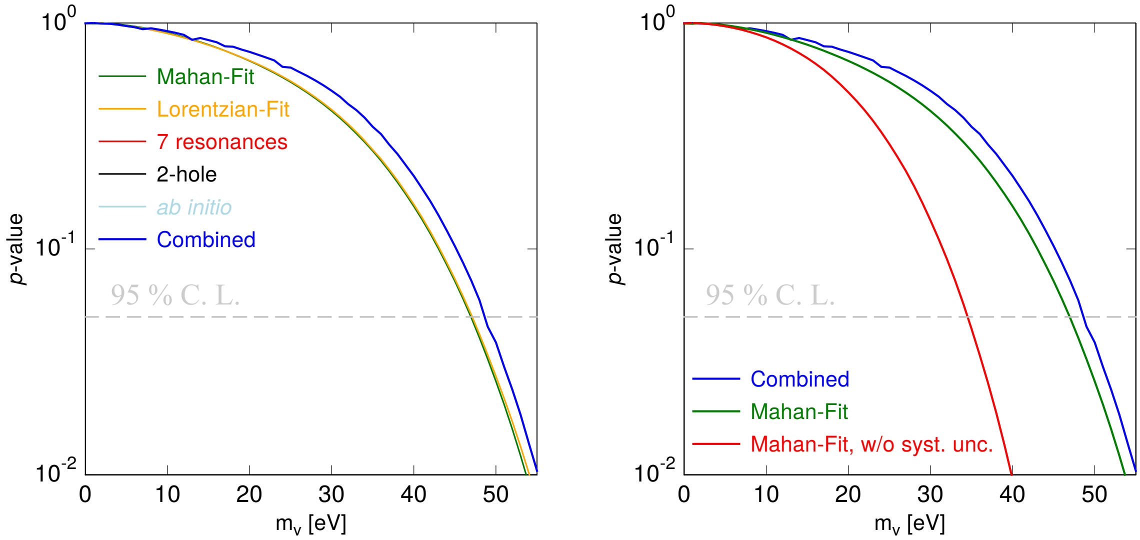

Figure 7.9: For different input theories the p-values for different neutrino masses are shown. Marked with the grey dashed line is the value corresponding to a 95 % C.L..

the uncertainty on the Q_{EC}-value the important factor. This can be seen in figure 7.9**(left)** and **(right)** where the difference in the obtained effective m_ν is small for different input theories and changes only slightly more for the Mahan input theory with an error on the spectral shape (Combined), but changes a lot more if all uncertainties on the nuisance parameters are neglected. Due to the here presented analysis about 10^{10} events are needed to reach a $10\,eV$ limit on m_ν assuming the here presented uncertainties and the Mahan fit as input theory.

This is still a preliminary analysis of the data and different analysis methods are still under investigation. With this analysis a conservative limit on the effective electron neutrino mass with $m_\nu < 49\,\mathrm{eV}$ 95 % C.L. can be provided which is significantly better then the present best limit of $m_\nu < 225\,\mathrm{eV}$ 95 % C.L. [Spr87], measured by an x-ray spectrum of ^{163}Ho . Here an improvement by a factor 5 was obtained. In the future a better theory description and a ^{163}Ho energy spectrum with even more statistics and a better energy resoltion will allow to deduce a sub-eV limit on the effective electron neutrino mass.

8. Summary

The ECHo experiment can be classified as the so, called direct neutrino mass measurements. In fact the goal of the ECHo project is to achieve a subeV sensitivity on the effective electron neutrino mass by the analysis of the end point region of a high statistics and high energy resolution ^{163}Ho electron capture spectrum. For this measurement metallic magnetic calorimeters with enclosed ^{163}Ho are used. MMCs are low temperature detectors that provide a very good spectral resolving power with $\Delta E_{\mathrm{FWHM}} = 1.6\,\mathrm{eV}$ at $6\,\mathrm{keV}$, a rather fast signal rise time with $\tau_{\mathrm{rise}} = 90\,\mathrm{ns}$ and a good energy linearity of below $1\,\%$ at $6\,\mathrm{keV}$ [Kem18]. Since the neutrino mass is deduced from the spectral shape, the background of such a measurement needs to be precisely known as well. Furthermore, is the determination of the Q-value of this decay of major importance, since the uncertainty on the Q-value has a big effect on the determination of the neutrino mass. In addition, a good theoretical understanding is required to deduce a neutrino mass from the spectral shape.

For all here presented measurements the experimental platforms including the connecting circuit boards have been designed and assembled as well as parts of the read out chain have been tested and mounted to reach the best possible performance for each experiment. Furthermore, was a pre and post processing with micro fabrication in the clean room on a single detector chip bases developed, which allowed to implant the ^{163}Ho via selective ion beam implantation into the gold absorbers of the used low temperature detectors.

The first presented experiment was the measurement of the heat capacity of ^{163}Ho in gold. It was obtained by the comparison of the signal height of two identical MMC set ups, one with ^{163}Ho implanted, the other one not. The in this way obtained specific heat per Ho-ion in Au was compared with two other heat capacity measurements [Vel19b]. By considering the actual ^{163}Ho ion concentration in the measured samples, the here obtained results are in good agreement with the results presented in [Vel19b].

For the specific heat per ^{163}Ho -ion in gold a Schottky anomaly was found around $250\,\mathrm{mK}$ caused dominantly by the hyperfine splitting of the magnetic moments of the electrons in ^{163}Ho and the crystal field splitting caused by the surrounding host material. This result has several implications for the ECHo projekt.

In general is the total heat capacity of the used MMCs a crucial parameter for the detector performance and should be kept low. It was found, that in general a lower detector temperature is preferable since the additional heat capacity due to implanted ^{163}Ho is the lowest for lower temperatures as the maximum of the Schottky anomaly is at 250 mK. The planned working temperature of the MMCs within ECHo is therefore with 20 mK adequate.

Furthermore, it could be shown, together with the other experiments with different concentrations of ^{163}Ho in the samples, that the holmium concentration effects the heat capacity of holmium at temperatures below 50 mK significant due to a shift of the Schottky anomaly of the holmium-holmium interactions towards lower temperatures. Due to the comparable results of the two different measurement techniques, where the ones presented in [Vel19b] used arc melted Au:Ho, it could be shown that the implantation process itself does not introduce an additional heat capacity by e.g. defects in the fcc Au crystal structure. For the next steps of ECHo a co implantation of ^{163}Ho together with Au is planned, to overcome a saturation limit of activity per pixel due to back scattering effects during the implantation. At this point the ^{163}Ho concentration can be adapted and should exceed a concentration of 2 % to minimize the additional heat capacity of ^{163}Ho in Au below 50 mK. Furthermore, was a specific heat capacity of $0.05\,k_\mathrm{B}$ at $T = 20\,\mathrm{mK}$ per Ho-ion found, which will increase the heat capacity of the here used ECHo-1k detector chip by 40 % for the planned activity of $a = 10\,\mathrm{Bq}$ per pixel, which will result in a factor 1.2 worsened fundamental energy resolution for the present detector design, if the read out chain is ideal. This is an acceptable value and will allow to reach a limit on the effective electron neutrino mass of below 10 eV as planned for the next phase of ECHo, ECHo-1k. As can be read in [Gas17] this requires an energy resolution of $\Delta E_\mathrm{FWHM} < 10\,\mathrm{eV}$.

The second measurement, this time of of the ^{163}Ho energy spectrum with maXs-20 detector chips was performed in an underground lab in Modane. 4 pixels have been operated for 4 days. In a spectrum with about 3×10^5 counts in total an energy resolution of $\Delta E_\mathrm{FWHM} = 9\,\mathrm{eV}$ at the NI resonance line was achieved. For this measurement and for the next one presented here a semi automated event analysis was developed. This allowed for adding all data sets with different gain and detector characteristics in a convenient way to the here presented energy spectrum. It could be shown that the used implantation techniques and in particular the purification (chemically and by mass separation) of the implanted ^{163}Ho result in no radioactive contamination visible with the achieved statistics. Furthermore, was the background between 2.9 keV and 6.8 keV analyzed. The two measured counts present in this region were attributed to the natural radioactivity background. The extracted BG-level for a flat background for this measurement was $BG < 2 \times 10^{-5}$ events/pixel/eV/day. The resulting unresolved pile-up fraction considering the 1 count between 2.9 keV and 5.8 keV gives $f_\mathrm{pu} = 1 \times 10^{-6}$. By the comparison with a measurement above ground [Has16] no significant change in background could be observed although the detectors in the underground lab where shielded by 4800 m of water equivalent, which reduces the cosmic muon flux by roughly 10^6. This measurement showed that the background rate is already very small, only one order of magnitude away from the desired background level of $BG < 1 \times 10^{-6}$ events/pixel/eV/day for a sub-eV sensitivity on the electron neutrino mass. Note that at this point of the measurements no material screening was performed and the poor statistics do only allow an upper limit for the BG. The material for the ECHo-1k detector and the dedicated ECHo cryostat has been screened. The results can be found in [Gas17]. Furthermore, an active muon veto is tested for the next phases of ECHo although it isstill not necessary at current level of acquired statistics. This energy spectrum provided new input data for theory with some spectral features that lead to the new Mahan like resonance shape presented in [Vel19a]. The very important results of this theoretical analysis of the measured data is that the in the end point region expected number of counts is enhanced by a factor of 2 for the new Mahan line shape compared to the old / resonances theory [Fae14].

Furthermore, a first new limit on the electron neutrino mass with $m_\nu < 140\,\mathrm{eV}$ 90 % C.L. could be deduced. In particular we have demonstrated that the biggest uncertainty on the neutrino mass limit is introduced by the uncertainty on the Q-value. For the Q-value the uncertainty will be reduced by a Penning trap mass spectrometry measurement (PENTATRAP) to about 1 eV. Higher statistic ^{163}Ho spectra will reduce the error on the Q-value, as well as uncertainties in the theoretical description of the ^{163}Ho spectrum. The error on the unresolved pile-up fraction will get significant smaller once the unresolved pile-up spectrum can be noticed and fitted.

The last measurement was performed with 23 pixels on an ECHo-1k detector chip operated over 22 days. The resulting energy spectrum had 3×10^7 counts and an energy resolution of $E_{\mathrm{FWHM}} = 6.2\,\mathrm{eV}$ at the NI resonance line. Her 267 data files have been added coherently to make up this spectrum. This huge number of data sub sets for 3×10^7 counts in the ^{163}Ho spectrum already shows, that an automatized signal analysis is necessary for this experiment. For this data sets an offline analysis was performed. Due to the large amount of data, used for a single signal trace An online data reduction is needed, which saves only the relevant signal parameters. The χ^2 of the fit might be one of these..

The in this thesis extracted Q-value is $Q = 2.837 \pm 0.005^{stat} \pm 0.005^{syst}\,\mathrm{keV}$. It is in good agreement with all other presented measurements of the Q-value [Ran17, Vel19a, Eli15]. While the statistical error on this presented Q-value might decrease with higher statistics, the systematic error will only decrease with a theory describing the additional broad structure in the end point region of the spectrum. Due to the rather good energy resolution and the high statistics in the achieved ^{163}Ho energy spectrum a detailed comparison between theory and experimental data is possible. Certain spectral features observed in the data have already been predicted by the new *ab initio* calculation presented in [Bra18]. A limit for the electron neutrino mass was extracted for this data set as well, providing the currently best limit of the electron neutrino mass with $m_\nu < 50\,\mathrm{eV}$ 95% C.L., which is a significant improvement of the former best limit of $m_\nu < 225\,\mathrm{eV}$ [Spr87]. Note that the here presented new limit is a preliminary analysis which still does not include a fully developed background model and has as input basis still ^{163}Ho theory models, which are still under development. A analysis with the described method for the neutrino mass limit extraction, the same nuisance parameters as used for this measurement and a simulated input theory following the Mahan fit, showed that with no improvement on the Q-value, the unresolved pile-up fraction, the energy resolution and the background level about 10^{10} events are needed to reach a limit for the electron neutrino mass of below 10 eV.

In conclusion this thesis contributed to fulfill many of the milestones for the ECHo-1k phase of the experiment:

For the detector optimization,

1. a reliable pre and post processing of detector chips for implantation was developed
2. a measurement of the specific heat per ^{163}Ho ion in Au, which determines the activity per pixel, was performed.

For the ^{163}Ho theory,

1. a high statistics and high energy resoltuion ^{163}Ho energy spectrum was measured for comparison with theory
2. a new Q-value with smaller uncertainty was extracted
3. a new preliminary limit on the effective electron neutrino mass was provided

Bibliography

[Abd09] J. N. Abdurashitov, V. N. Gavrin, V. V. Gorbachev, P. P. Gurkina, T. V. Ibragimova, A. V. Kalikhov, N. G. Khairnasov, T. V. Knodel, I. N. Mirmov, A. A. Shikhin, E. P. Veretenkin, V. E. Yants, G. T. Zatsepin, T. J. Bowles, S. R. Elliott, W. A. Teasdale, J. S. Nico, B. T. Cleveland, and J. F. Wilkerson, Measurement of the solar neutrino capture rate with gallium metal. iii. results for the 2002–2007 data-taking period, *Phys. Rev. C*, **80**, 015807, 2009.

[Abe11] K. Abe, Y. Hayato, T. Iida, M. Ikeda, C. Ishihara, K. Iyogi, J. Kameda, K. Kobayashi, Y. Koshio, Y. Kozuma, M. Miura, S. Moriyama, M. Nakahata, S. Nakayama, Y. Obayashi, H. Ogawa, H. Sekiya, M. Shiozawa, Y. Suzuki, A. Takeda, et al., Solar neutrino results in super-kamiokande-iii, *Phys. Rev. D*, **83**, 052010, 2011.

[Abe18] K. Abe et al., Hyper-kamiokande design report, *arXiv: 1805.04163*, 2018.

[Abr70a] A. Abragam and B. Bleaney, Electron paramagnetic resonance of transition-ions, *Oxford Press*, 1970.

[Abr70b] A. Abragam and B. Bleaney, Electron Paramagnetic Resonance of Transition Metals, Claredon Press Oxford, 1970.

[Acq09] R. Acquafredda, T. Adam, N. Agafonova, P. A. Sanchez, M. Ambrosio, A. Anokhina, S. Aoki, A. Ariga, T. Ariga, L. Arrabito, C. Aufranc, D. Autiero, A. Badertscher, A. Bagulya, E. Baussan, A. Bergnoli, F. B. Greggio, A. Bertolin, M. Besnier, D. Biaré, et al., The opera experiment in the cern to gran sasso neutrino beam, *Journal of Instrumentation*, **4**(04), P04018, 2009.

[Ahm01] Q. R. Ahmad, R. C. Allen, T. C. Andersen, J. D. Anglin, G. Bühler, J. C. Barton, E. W. Beier, M. Bercovitch, J. Bigu, S. Biller, R. A. Black, I. Blevis, R. J. Boardman, J. Boger, E. Bonvin, M. G. Boulay, M. G. Bowler, T. J. Bowles, S. J. Brice, M. C. Browne, et al., Measurement of the rate of $\nu_e + d \rightarrow p + p + e^-$ interactions produced by ^8b solar neutrinos at the sudbury neutrino observatory, *Phys. Rev. Lett.*, **87**, 071301, 2001.

[Ahm02] Q. R. Ahmad, R. C. Allen, T. C. Andersen, J. D.Anglin, J. C. Barton, E. W. Beier, M. Bercovitch, J. Bigu, S. D. Biller, R. A. Black, I. Blevis,

R. J. Boardman, J. Boger, E. Bonvin, M. G. Boulay, M. G. Bowler, T. J. Bowles, S. J. Brice, M. C. Browne, T. V. Bullard, et al., Direct evidence for neutrino flavor transformation from neutral-current interactions in the sudbury neutrino observatory, *Phys. Rev. Lett.*, **89**, 011301, 2002.

[Alp15] B. Alpert, M. Balata, D. Bennett, M. Biasotti, C. Boragno, C. Brofferio, V. Ceriale, D. Corsini, P. K. Day, M. De Gerone, R. Dressler, M. Faverzani, E. Ferri, J. Fowler, F. Gatti, A. Giachero, J. Hays-Wehle, S. Heinitz, G. Hilton, U. Köster, et al., Holmes, *The European Physical Journal C*, **75**(3), 112, 2015.

[Alt05] M. Altmann, M. Balata, P. Belli, E. Bellotti, R. Bernabei, E. Burkert, C. Cattadori, R. Cerulli, M. Chiarini, M. Cribier, S. d'Angelo, G. D. Re, K. Ebert, F. von Feilitzsch, N. Ferrari, W. Hampel, F. Hartmann, E. Henrich, G. Heusser, F. Kaether, et al., Complete results for five years of GNO solar neutrino observations, *Physics Letters B*, **616**(3-4), 174–190, 2005.

[And82] J. Andersen, G. Beyer, G. Charpak, A. D. Rújula, B. Elbek, H. Gustafsson, P. Hansen, B. Jonson, P. Knudsen, E. Laegsgaard, J. Pedersen, and H. Ravn, A limit on the mass of the electron neutrino: The case of 163ho, *Physics Letters B*, **113**(1), 72 – 76, 1982.

[Ang05] J. Angrik et al., KATRIN design report 2004, 2005.

[Ant04] P. Antonioli, R. T. Fienberg, F. Fleurot, Y. Fukuda, W. Fulgione, A. Habig, J. Heise, A. B. McDonald, C. Mills, T. Namba, L. J. Robinson, K. Scholberg, M. Schwendener, R. W. Sinnott, B. Stacey, Y. Suzuki, R. Tafirout, C. Vigorito, B. Viren, C. Virtue, et al., SNEWS: the SuperNova early warning system, *New Journal of Physics*, **6**, 114–114, 2004.

[Ase11] V. N. Aseev, A. I. Belesev, A. I. Berlev, E. V. Geraskin, A. A. Golubev, N. A. Likhovid, V. M. Lobashev, A. A. Nozik, V. S. Pantuev, V. I. Parfenov, A. K. Skasyrskaya, F. V. Tkachov, and S. V. Zadorozhny, Upper limit on the electron antineutrino mass from the Troitsk experiment, *Phys. Rev. D*, **84**, 112003, 2011.

[Bah04] J. N. Bahcall and M. H. Pinsonneault, What do we (not) know theoretically about solar neutrino fluxes?, *Phys. Rev. Lett.*, **92**, 121301, 2004.

[Bai83] P. A. Baisden, D. H. Sisson, S. Niemeyer, B. Hudson, C. L. Bennett, and R. A. Naumann, Measurement of the half-life of ^{163}Ho, *Phys. Rev. C*, **28**, 337–341, 1983.

[Bat16] C. R. Bates, C. Pies, S. Kempf, D. Hengstler, A. Fleischmann, L. Gastaldo, C. Enss, and S. Friedrich, Reproducibility and calibration of mmc-based high-resolution gamma detectors, *Applied Physics Letters*, **109**(2), 023513, 2016.

[Ben81] C. Bennett, A. Hallin, R. Naumann, P. Springer, M. Witherell, R. Chrien, P. Baisden, and D. Sisson, The x-ray spectrum following 163ho m electron capture, *Physics Letters B*, **107**(1), 19 – 22, 1981.

[Ber12] J. Beringer, J. F. Arguin, R. M. Barnett, K. Copic, O. Dahl, D. E. Groom, C. J. Lin, J. Lys, H. Murayama, C. G. Wohl, W. M. Yao, P. A. Zyla, C. Amsler, M. Antonelli, D. M. Asner, H. Baer, H. R. Band, T. Basaglia, C. W. Bauer, J. J. Beatty, et al., Review of particle physics, *Phys. Rev. D*, **86**, 010001, 2012, including the 2013 partial update for the 2014 edition.

[Ble89] B. Bleany, Lanthanide ions in metallic gold - ii. terbium and holmium, *Proc. R. Soc. Lond. A*, **424**(1876), 1989.

[Bra18] M. Brass and et al., *Ab initio* calculation of the calorimetric electron capture spectrum of ^{163}holmium: Intra-atomic decay into bound-states, *Phys. Rev. C*, **97**, 054620, 2018.

[Bre19] J. Brehmer, *private communication*, 2019.

[Cap17] F. Capozzi, E. Di Valentino, E. Lisi, A. Marrone, A. Melchiorri, and A. Palazzo, Global constraints on absolute neutrino masses and their ordering, *Phys. Rev. D*, **95**, 096014, 2017.

[Cha14] J. Chadwick, Intensitätsverteilung im magnetischen spektrum der β-strahlen von radium b+c., *Verhandlungen der Deutschen Physikalischen Gesellschaft*, **16**, 383–391, 1914.

[Cla04] J. Clarke and A. I. Braginski (Ed.), The SQUID Handbook, WILEY-VCH, 2004.

[Cle98] B. T. Cleveland, T. Daily, J. Raymond Davis, J. R. Distel, K. Lande, C. K. Lee, P. S. Wildenhain, and J. Ullman, Measurement of the solar electron neutrino flux with the homestake chlorine detector, *The Astrophysical Journal*, **496**(1), 505, 1998.

[Cos93] E. Cosulich, F. Gatti, and S. Vitale, Further results on μ-calorimeters with superconducting absorber, *Journal of Low Temperature Physics*, **93**(3), 263–268, 1993.

[Cow56] C. L. Cowan, F. Reines, F. B. Harrison, H. W. Kruse, and A. D. McGuire, Detection of the free neutrino: a confirmation, *Science*, **124**(3212), 103–104, 1956.

[Cow11] G. Cowan, K. Cranmer, E. Gross, and O. Vitells, Asymptotic formulae for likelihood-based tests of new physics, *Eur. Phys. J.*, **C71**, 1554, 2011.

[Cro14] M. P. Croce, E. M. Bond, A. S. Hoover, G. J. Kunde, W. A. Moody, M. W. Rabin, D. A. Bennett, J. Hayes-Wehle, V. Kotsubo, D. R. Schmidt, and J. N. Ullom, Integration of radioactive material with microcalorimeter detectors, *Journal of Low Temperature Physics*, **176**(5), 1009–1014, 2014.

[Dan05] T. Daniyarov, Metallische magnetische Kalorimeter zum hochauflösenden Nachweis von Röntgenquanten und hochenergetischen Molekülen, PhD Thesis, Heidelberg University, 2005.

[Dor18] K. Dorrer, H.and Chrysalidis, T. Goodacre, and et al., Production, isolation and characterization of radiochemically pure 163ho samples for the echo-project, *Radiochim. Acta*, **106**, 535 – 547, 2018.

[DR81] A. De Rújula, A new way to measure neutrino masses, *Nuclear Physics B*, **188**(3), 414 – 458, 1981.

[DR15] A. De Rújula and M. Lusignoli, The calorimetric spectrum of the electron-capture decay of ^{163}ho. a preliminary analysis of the preliminary data, *arXiv: 1510.05462*, 2015.

[Dru07] D. Drung, C. Assmann, J. Beyer, A. Kirste, M. Peters, F. Ruede, and T. Schurig, Highly Sensitive and Easy-to-Use SQUID Sensors, *Applied Superconductivity, IEEE Transactions on*, **17**(2), 699–704, 2007.

[Dvo11] R. Dvornický, K. Muto, F. Šimkovic, and A. Faessler, Absolute mass of neutrinos and the first unique forbidden β decay of ^{187}re, *Phys. Rev. C*, **83**, 045502, 2011.

[Eli15] S. Eliseev, K. Blaum, M. Block, S. Chenmarev, H. Dorrer, C. E. Düllmann, C. Enss, P. E. Filianin, L. Gastaldo, M. Goncharov, U. Köster, F. Lautenschläger, Y. N. Novikov, A. Rischka, R. X. Schüssler, L. Schweikhard, and A. Türler, Direct measurement of the mass difference of ^{163}Ho and ^{163}Dy solves the q-value puzzle for the neutrino mass determination, *Phys. Rev. Lett.*, **115**, 062501, 2015.

[Ens00] C. Enss, A. Fleischmann, K. Horst, J. Schönefeld, J. Sollner, J. Adams, Y. Huang, Y. Kim, and G. Seidel, Metallic magnetic calorimeters for particle detection, *Journal of Low Temperature Physics*, **121**(3-4), 137–176, 2000.

[Esf17] A. A. Esfahani, D. M. Asner, S. Böser, R. Cervantes, C. Claessens, L. de Viveiros, P. J. Doe, S. Doeleman, J. L. Fernandes, M. Fertl, E. C. Finn, J. A. Formaggio, D. Furse, M. Guigue, K. M. Heeger, A. M. Jones, K. Kazkaz, J. A. Kofron, C. Lamb, B. H. LaRoque, et al., Determining the neutrino mass with cyclotron radiation emission spectroscopy—project 8, *Journal of Physics G: Nuclear and Particle Physics*, **44**(5), 054004, 2017.

[Est19] I. Esteban, M. C. Gonzalez-Garcia, A. Hernandez-Cabezudo, M. Maltoni, and T. Schwetz, Global analysis of three-flavour neutrino oscillations: synergies and tensions in the determination of θ23, δcp, and the mass ordering, *Journal of High Energy Physics*, **2019**(1), 106, 2019.

[Fae14] A. Faessler, L. Gastaldo, and F. Šimkovic, Electron capture in163ho, overlap plus exchange corrections and neutrino mass, *Journal of Physics G: Nuclear and Particle Physics*, **42**(1), 015108, 2014.

[Fae15] A. Faessler, C. Enss, L. Gastaldo, and F. Šimkovic, Determination of the neutrino mass by electron capture in ^{163}Ho and the role of the three-hole states in ^{163}Dy, *Phys. Rev. C*, **91**, 064302, 2015.

[Fer34] E. Fermi, Versuch einer theorie der β-strahlen., *Zeitschrift für Physik*, **88**(3-4), 161–177, 1934.

[Fer12] E. Ferri, C. Arnaboldi, G. Ceruti, M. Faverzani, F. Gatti, A. Giachero, C. Gotti, C. Kilbourne, S. Kraft-Bermuth, A. Nucciotti, G. Pessina, D. Schaeffer, and M. Sisti, Mare-1 in milan: Status and perspectives, *Journal of Low Temperature Physics*, **167**(5-6), 1035–1040, 2012.

[Fer14] E. Ferri, D. Bagliani, M. Biassotti, G. Ceruti, D. Corsini, M. Faverzani, F. Gatti, A. Giachero, C. Gotti, C. Kilbourne, A. Kling, S. Kraft-Bermuth, M. Maino, P. Manfrinetti, A. Nucciotti, G. Pessina, G. Pizzigoni, M. Ribeiro Gomes, D. Schaeffer, and M. Sisti, Preliminary results of the mare experiment, *Journal of Low Temperature Physics*, 1–6, 2014.

[Fle98] A. Fleischmann, Hochauflösendes magnetisches Kalorimeter zur Detektion von einzelnen Röntgenquanten, Diploma thesis, Kirchhoff-Institut für Physik, Universität Heidelberg, 1998.

[Fle00] A. Fleischmann, J. Schönefeld, J. Sollner, C. Enss, J. S. Adams, S. R. Bandler, Y. H. Kim, and G. M. Seidel, Low temperature properties of erbium in gold, *J. Low Temp. Phys.*, **118**(1), 7–21, 2000.

[Fle03] A. Fleischmann, Magnetische Mikrokalorimeter: Hochauflösende Röntgenspektroskopie mit energiedispersiven Detektoren, PhD Thesis, Kirchhoff-Institut für Physik, Universität Heidelberg, 2003.

[Fle05] A. Fleischmann, C. Enss, and G. M. Seidel, Metallic magnetic calorimeters, in C. Enss (Ed.), *Cryogenic particle detection*, number 99 in Topics in Applied Physics, Chapter 4, 151–216, Springer-Verlag Berlin, Heidelberg, 2005.

[Fle09] A. Fleischmann, L. Gastaldo, S. Kempf, A. Kirsch, A. Pabinger, C. Pies, J. Porst, P. Ranitzsch, S. Schäfer, F. v. Seggern, T. Wolf, C. Enss, and G. M. Seidel, Metallic magnetic calorimeters, *AIP Conference Proceedings*, **1185**(1), 571–578, 2009.

[Fuk98] Y. Fukuda, T. Hayakawa, E. Ichihara, K. Inoue, K. Ishihara, H. Ishino, Y. Itow, T. Kajita, J. Kameda, S. Kasuga, K. Kobayashi, Y. Kobayashi, Y. Koshio, M. Miura, M. Nakahata, S. Nakayama, A. Okada, K. Okumura, N. Sakurai, M. Shiozawa, et al., Evidence for oscillation of atmospheric neutrinos, *Phys. Rev. Lett.*, **81**, 1562–1567, 1998.

[Fur39] W. H. Furry, On transition probabilities in double beta-disintegration, *Phys. Rev.*, **56**, 1184–1193, 1939.

[Gal12] M. Galeazzi, F. Gatti, M. Lusignoli, A. Nucciotti, S. Ragazzi, and M. R. Gomes, The Electron Capture Decay of 163-Ho to Measure the Electron Neutrino Mass with sub-eV Accuracy (and Beyond), *arXiv:1202.4763 [physics.ins-det]*, 2012.

[Gam17] L. Gamer, C. E. Düllmann, C. Enss, A. Fleischmann, L. Gastaldo, C. Hassel, S. Kempf, T. Kieck, and K. Wendt, Simulation and optimization of the implantation of holmium atoms into metallic magnetic microcalorimeters for neutrino mass determination experiments, *Nuclear Instruments and Methods in Physics Research Section A: Accelerators, Spectrometers, Detectors and Associated Equipment*, **854**, 139 – 148, 2017.

[Gas17] L. Gastaldo, K. Blaum, K. Chrysalidis, T. Day Goodacre, A. Domula, M. Door, H. Dorrer, C. E. Düllmann, K. Eberhardt, S. Eliseev, C. Enss, A. Faessler, P. Filianin, A. Fleischmann, D. Fonnesu, L. Gamer, R. Haas, C. Hassel, D. Hengstler, J. Jochum, et al., The electron capture in 163ho experiment – echo, *The European Physical Journal Special Topics*, **226**(8), 1623–1694, 2017.

[Gat97] F. Gatti, P. Meunier, C. Salvo, and S. Vitale, Calorimetric measurement of the 163Ho spectrum by means of a cryogenic detector, *Physics Letters B*, **398**(3-4), 415 – 419, 1997.

[Gat01] F. Gatti, Microcalorimeter measurements, *Nuclear Physics B - Proceedings Supplements*, **91**(1–3), 293 – 296, 2001, Neutrino 2000.

[Gra17] N. Grant, DUNE Oscillation Physics, *PoS*, **NuFact2017**, 052, 2017.

[Hah92] W. Hahn, M. Loewenhaupt, and B. Frick, Crystal field excitations in dilute rare earth noble metal alloys, *Phys. B.*, **180**, 176–178, 1992.

[Ham99] W. Hampel, J. Handt, G. Heusser, J. Kiko, T. Kirsten, M. Laubenstein, E. Pernicka, W. Rau, M. Wojcik, Y. Zakharov, R. Ammon, K. Ebert, T. Fritsch, D. Heidt, E. Henrich, L. Stielglitz, F. Weirich, M. Balata, M. Sann, F. Hartmann, et al., GALLEX solar neutrino observations: results for GALLEX IV, *Physics Letters B*, **447**(1-2), 127–133, 1999.

[Har68] J. Harding and J. Zimmerman, Quantum interference magnetometry and thermal noise from a conducting environment, *Physics Letters A*, **27**(10), 670 – 671, 1968.

[Har92] F. Hartmann and R. Naumann, High temperature gas proportional detector techniques and application to the neutrino mass limit using ^{163}ho, *Nuclear Instruments and Methods in Physics Research Section A: Accelerators, Spectrometers, Detectors and Associated Equipment*, **313**(1–2), 237 – 260, 1992.

[Has16] C. Hassel, K. Blaum, T. D. Goodacre, H. Dorrer, C. E. Düllmann, K. Eberhardt, S. Eliseev, C. Enss, P. Filianin, A. Fäßler, A. Fleischmann, L. Gastaldo, M. Goncharov, D. Hengstler, J. Jochum, K. Johnston, M. Keller, S. Kempf, T. Kieck, U. Köster, et al., Recent results for the echo experiment, *Journal of Low Temperature Physics*, **184**(3), 910–921, 2016.

[Hei19] L. Heinriich, M. Feickert, and G. Stark, diana-hep/pyhf v0.1.0, 2019.

[Hen12] D. Hengstler, Untersuchung der Eigenschaften von supraleitenden Re-, Zn- und Zn:Mn-Absorbern für magnetische Mikrokalorimeter, Diploma thesis, Kirchhoff-Institut für Physik, Universität Heidelberg, 2012.

[Hen17] D. Hengstler, Development and characterization of the two-dimensional metallic magnetic calorimeter array maXs30 for the high-resolution X-ray spectroscopy, PhD Thesis, Kirchhoff-Institut für Physik, Universität Heidelberg, 2017.

[Her00] T. Herrmannsdörfer, R. König, and C. Enss, Properties of er-doped au at ultralow temperatures, *Phys. B*, **284–288, Part 2**, 1698 – 1699, 2000.

[Heu11] S. Heuser, Entwicklung mikrostrukturierter magnetischer Kalorimeter mit verbesserter magnetischer Flusskopplung für die hochauflösende Röntgenspektroskopie, Masters Thesis, Kirchhoff-Institut für Physik, Universität Heidelberg, 2011.

[Hof12] V. Hoffmann, Messung der AC-Suszeptibilität von paramagnetischem Au:Er bei Temperaturen oberhalb des Spinglasübergangs, B.sc. thesis, Kirchhoff-Institut für Physik, Universität Heidelberg, 2012.

[Hoo06] A. S. Hoover, M. W. Rabin, C. R. Rudy, D. M. Tournear, D. T. Vo, J. A. Beall, W. B. Doriese, R. D. Horansky, K. D. Irwin, J. N. Ullom, B. L. Zink, and K. E. Chesson, Monte carlo studies of high resolution microcalorimeter detectors, in *2006 IEEE Nuclear Science Symposium Conference Record*, Volume 2, 1268–1272, 2006.

[Hub11] P. Huber, Determination of antineutrino spectra from nuclear reactors, *Phys. Rev. C*, **84**, 024617, 2011.

[Jos62] B. Josephson, Possible new effects in superconductive tunnelling, *Physics Letters*, **1**(7), 251 – 253, 1962.

[Kas56] T. Kasuya, A theory of metallic ferro- and antiferromagnetism on zener's model, *Prog. Theor. Phys.*, **16**(1), 45, 1956.

[Kem13] S. Kempf, M. Wegner, L. Gastaldo, A. Fleischmann, and C. Enss, Multiplexed readout of mmc detector arrays using non-hysteretic rf-squids, *Journal of Low Temperature Physics*, 1–7, 2013.

[Kem18] S. Kempf, A. Fleischmann, L. Gastaldo, and C. Enss, Physics and applications of metallic magnetic calorimeters, *Journal of Low Temperature Physics*, **193**(3), 365–379, 2018.

[Kie19] T. Kieck, H. Dorrer, V. Gadelshin, F. Schneider, and K. Wendt, Highly efficient isotope separation and ion implantation of ^{163}ho for the echo project, *arXive 1904.05559*, 2019.

[Kra05] C. Kraus, B. Bornschein, L. Bornschein, J. Bonn, B. Flatt, A. Kovalik, B. Ostrick, E. Otten, J. Schall, T. Thümmler, and C. Weinheimer, Final results from phase II of the Mainz neutrino mass search in tritium β decay, *The European Physical Journal C - Particles and Fields*, **40**(4), 447–468, 2005.

[Kra13] S. Kraft-Bermuth, V. Andrianov, A. Bleile, A. Echler, P. Egelhof, P. Grabitz, S. Ilieva, C. Kilbourne, O. Kiselev, D. McCammon, and J. Meier, High-precision x-ray spectroscopy of highly charged ions with microcalorimeters, *Physica Scripta*, **2013**(T156), 014022, 2013.

[Kru83] P. Kruit and F. H. Read, Magnetic field paralleliser for 2π electron-spectrometer and electron-image magnifier, *Journal of Physics E: Scientific Instruments*, **16**(4), 313, 1983.

[Lae84] E. Laegsgaard, J. U. Andersen, G. J. Beyer, A. De Rújula, P. G. Hansen, B. Jonson, and H. L. Ravn, The capture ratio n/m in the ec beta decay of ^{163}ho, in O. Klepper (Ed.), *Proceedings of the 7th International Conference on Atomic Masses and Fundamental Constants AMCO-7*, number 26 in THD Schriftenreihe Wissenschaft und Technik, 652–658, Darmstadt-Seeheim, 1984.

[Lea62] K. Lea, M. Leask, and W. Wolf, The raising of angular momentum degeneracy of f-electron terms by cubic crystal fields, *Journal of Physics and Chemistry of Solids*, **23**(10), 1381 – 1405, 1962.

[Lor02] T. J. Loredo and D. Q. Lamb, Bayesian analysis of neutrinos observed from supernova sn 1987a, *Phys. Rev. D*, **65**, 063002, 2002.

[Maj37] E. Majorana, Teoria simmetrica dell'elettrone e del positrone, *Il Nuovo Cimento*, **14**(4), 171–184, 1937.

[Mat11] J. A. B. Mates, The Microwave SQUID Multiplexer, PhD Thesis, University of Colorado at Boulder, 2011.

[McC84] D. McCammon, M. Juda, D. D. Reeder, R. L. Kelley, S. H. Moseley, and A. E. Szymkowiak, A new technique for neutrino mass measurement, in V. Barger and D. Cline (Ed.), *Neutrino Mass and Low Energy Weak Interactions*, 329–343, World Scientific, 1984.

[McC93] D. McCammon, W. Cui, M. Juda, J. Morgenthaler, J. Zhang, R. Kelley, S. Holt, G. Madejski, S. Moseley, and A. Szymkowiak, Thermal calorimeters for high resolution x-ray spectroscopy, *Nucl. Instr. Meth. Phys. Res. A*, **326**(1), 157 – 165, 1993.

[Mou09] B. J. Mount, M. Redshaw, and E. G. Myers, q value of ^{115}in $\rightarrow^{115}$ sn($3/2^+$): The lowest known energy β decay, *Phys. Rev. Lett.*, **103**, 122502, 2009.

[Mue11] T. A. Mueller, D. Lhuillier, M. Fallot, A. Letourneau, S. Cormon, M. Fechner, L. Giot, T. Lasserre, J. Martino, G. Mention, A. Porta, and F. Yermia, Improved predictions of reactor antineutrino spectra, *Phys. Rev. C*, **83**, 054615, 2011.

[Mur70] A. P. Murani, Magnetic susceptibility and electrical resistivity of some gold-rare-earth alloys, *Journal of Physics C: Solid State Physics*, **3**(2S), S153–S158, 1970.

[Nil03] T. Nilsson, The isolde facility at cern, in J. Äystö, P. Dendooven, A. Jokinen, and M. Leino (Ed.), *Exotic Nuclei and Atomic Masses*, 469–472, Berlin, Heidelberg, 2003, Springer Berlin Heidelberg.

[Nuc08] A. Nucciotti, The mare project, *Journal of Low Temperature Physics*, **151**(3-4), 597–602, 2008.

[Pau77] W. Pauli, Fünf Arbeiten zum Ausschließungsprinzip und zum Neutrino, Number 27 in Texte zur Forschung, Wissenschaftliche Buchgesellschaft Darmstadt, 1977, URL:`http://neutrino.uni-hamburg.de/...pauli.pdf`.

[Pic92] A. Picard, H. Backe, H. Barth, J. Bonn, B. Degen, T. Edling, R. Haid, A. Hermanni, P. Leiderer, T. Loeken, A. Molz, R. Moore, A. Osipowicz, E. Otten, M. Przyrembel, M. Schrader, M. Steininger, and C. Weinheimer, A solenoid retarding spectrometer with high resolution and transmission for kev electrons, *Nuclear Instruments and Methods in Physics Research Section B: Beam Interactions with Materials and Atoms*, **63**(3), 345 – 358, 1992.

[Pie08] C. Pies, Entwicklung eines Detektor-Arrays basierend auf magnetischen Kalorimetern für die hochaufgelöste Röntgenspektroskopie an hochgeladenen Ionen, Masters Thesis, Kirchhoff-Institut für Physik, Universität Heidelberg, 2008.

[Pie12] C. Pies, S. Schäfer, S. Heuser, S. Kempf, A. Pabinger, J.-P. Porst, P. Ranitsch, N. Foerster, D. Hengstler, A. Kampkötter, T. Wolf, L. Gastaldo, A. Fleischmann, and C. Enss, maXs: Microcalorimeter Arrays for High-Resolution X-Ray Spectroscopy at GSI/FAIR, *Journal of Low Temperature Physics*, **167**(3-4), 269–279, 2012.

[Pon57] B. Pontecorvo, Mesonium and antimesonium, *Sov. Phys. JETP*, **6**, 429–431, 1957.

[Pon58] B. Pontecorvo, Inverse beta processes and nonconservation of lepton charge, *Sov. Phys. JETP*, **7**, 172–173, 1958.

[Por11] J.-P. Porst, High-Resolution Metallic Magnetic Calorimeters for β-Spectroscopy on ^{187}Rhenium and Position Resolved X-Ray Spectroscopy, PhD Thesis, Heidelberg University, 2011.

[Pow74] R. Powers, P. Martin, G. Miller, R. Welsh, and D. Jenkins, Muonic 197au: A test of the weak-coupling model, *Nucl. Phys. A*, **230**(3), 413 – 444, 1974.

[Ran12] P.-O. Ranitzsch, J.-P. Porst, S. Kempf, C. Pies, S. Schäfer, D. Hengstler, A. Fleischmann, C. Enss, and L. Gastaldo, Development of Metallic Magnetic Calorimeters for High Precision Measurements of Calorimetric ^{187}Re and ^{163}Ho Spectra, *Journal of Low Temperature Physics*, **167**(5-6), 1004–1014, 2012.

[Ran17] P. C.-O. Ranitzsch, C. Hassel, M. Wegner, D. Hengstler, S. Kempf, A. Fleischmann, C. Enss, L. Gastaldo, A. Herlert, and K. Johnston, Characterization of the ^{163}Ho electron capture spectrum: A step towards the electron neutrino mass determination, *Phys. Rev. Lett.*, **119**, 122501, 2017.

[RC19] S. Roy Choudhury and S. Hannestad, Updated results on neutrino mass and mass hierarchy from cosmology with planck 2018 likelihoods, *arXiv: 1907.12598*, 2019.

[Rob15] R. H. Robertson, Direct probes of neutrino mass, *Nuclear and Particle Physics Proceedings*, **265-266**, 7 – 12, 2015, Proceedings of the Neutrino Oscillation Workshop.

[Rud54] M. A. Ruderman and C. Kittel, Indirect exchange coupling of nuclear magnetic moments by conduction electrons, *Phys. Rev.*, **96**, 99–102, 1954.

[Sch00] J. Schönefeld, Entwicklung eines mikrostrukturierten magnetischen Tieftemperaturkalorimeters zum hochauflösenden Nachweis von einzelnen Röntgenquanten, PhD Thesis, Kirchhoff-Institut für Physik, Universität Heidelberg, 2000.

[Sis04] M. Sisti, C. Arnaboldi, C. Brofferio, G. Ceruti, O. Cremonesi, E. Fiorini, A. Giuliani, B. Margesin, L. Martensson, A. Nucciotti, M. Pavan, G. Pessina, S. Pirro, E. Previtali, L. Soma, and M. Zen, New limits from the milano neutrino mass experiment with thermal microcalorimeters, *Nuclear Instruments and Methods in Physics Research Section A: Accelerators, Spectrometers, Detectors and Associated Equipment*, **520**(1–3), 125 – 131, 2004, Proceedings of the 10th International Workshop on Low Temperature Detectors.

[Spr87] P. T. Springer, C. L. Bennett, and P. A. Baisden, Measurement of the neutrino mass using the inner bremsstrahlung emitted in the electron-capture decay of ^{163}ho, *Phys. Rev. A*, **35**, 679–689, 1987.

[Ste52] K. W. H. Stevens, Matrix elements and operator equivalents connected with the magnetic properties of rare earth ions, *Proceedings of the Physical Society. Section A*, **65**(3), 209–215, 1952.

[Tao71] L. J. Tao, D. Davidov, R. Orbach, and E. P. Chock, Hyperfine splitting of er and yb resonances in au: A separation between the atomic and covalent contributions to the exchange integral, *Physical Review B*, **4**, 5–9, 1971.

[TC11] S. Turck-Chièze and S. Couvidat, Solar neutrinos, helioseismology and the solar internal dynamics, *Reports on Progress in Physics*, **74**(8), 086901, 2011.

[Vel19a] C. Velte and et al., High-resolution and low-background ^{163}ho spectrum: interpretation of the resonance tails, *to be submitted*, 2019.

[Vel19b] C. Velte, M. Herbst, A. Reifenberger, and et al., Specific heat of holmium in gold and silver at low temperatures, *to be submitted*, 2019.

[Weg18] M. Wegner, Entwicklung, Herstellung und Charakterisierung eines auf metallischen magnetischen Kalorimetern basierenden Detektorarrays mit 64 Pixeln und integriertem Mikrowellen-SQUID-Multiplexer, PhD Thesis, Kirchhoff-Institut für Physik, Universität Heidelberg, 2018.

[Wie09] J. S. E. Wieslander, J. Suhonen, T. Eronen, M. Hult, V.-V. Elomaa, A. Jokinen, G. Marissens, M. Misiaszek, M. T. Mustonen, S. Rahaman, C. Weber, and J. Äystö, Smallest known q value of any nuclear decay: The rare β^- decay of ^{115}in$(9/2^+) \rightarrow^{115}$ sn$(3/2^+)$, *Phys. Rev. Lett.*, **103**, 122501, 2009.

[Wil69] G. Williams and L. L. Hirst, Crystal-field effects in solid solutions of rare earths in noble metals, *Phys. Rev.*, **185**, 407–415, 1969.

[Wiß13] V. Wißdorf, Magnetisches 1/f-Rauschen und Imaginärteil der magnetischen Suszeptibilität von Erbium dotiertem Gold bei Millikelvin Temperaturen, Bachelor Thesis, Heidelberg University, 2013.

[Yas83] S. Yasumi, G. Rajasekaran, M. Ando, F. Ochiai, H. Ikeda, T. Ohta, P. Stefan, M. Maruyama, N. Hashimoto, M. Fujioka, K. Ishii, T. Shinozuka, K. Sera, T. Omori, G. Izawa, M. Yagi, K. Masumoto, and K. Shima, The mass of the electron neutrino and electron capture in 163ho, *Physics Letters B*, **122**(5–6), 461 – 464, 1983.

[Yas94] S. Yasumi, H. Maezawa, K. Shima, Y. Inagaki, T. Mukoyama, T. Mizogawa, K. Sera, S. Kishimoto, M. Fujioka, K. Ishii, T. Omori, G. Izawa, and O. Kawakami, The mass of the electron neutrino from electron capture in 163ho, *Physics Letters B*, **334**(1–2), 229 – 233, 1994.

[Yos57] K. Yosida, Magnetic properties of cu-mn alloys, *Phys. Rev.*, **106**, 893–898, 1957.

Ich erkläre hiermit, dass ich die vorgelegte Dissertation selbständig verfasst und dabei keine anderen als die angegebenen Quellen und Hilfsmittel verwendet habe.

Heidelberg, 19. August 2019 ....
(Clemens Velte)